Diplomarbeit

Development of a Soft Sensor for Monitoring Product Gas Composition in a Dual Fluidized Bed Gasifier

ausgeführt zum Zwecke der Erlangung des akademischen Grades eines
Diplom-Ingenieur (Dipl.-Ing.)

eingereicht and der Technischen Universität Wien
Fakultät für Maschinenwesen und Betriebswissenschaften
von

Jonas Vogler
Mat.Nr.: 12040673

unter Leitung von
Dipl.-Ing. Dr. techn. Alexander Schirrer
Institut für Mechanik und Mechatronik, E325

Ort, Datum

Unterschrift

Ich nehme zur Kenntnis, dass ich zur Drucklegung dieser Arbeit nur mit Bewilligung der Prüfungskommission berechtigt bin.

Eidesstattliche Erklärung

Ich erkläre an Eides statt, dass die vorliegende Arbeit nach den anerkannten Grundsätzen für wissenschaftliche Abhandlungen von mir selbstständig erstellt wurde. Alle verwendeten Hilfsmittel, insbesondere die zugrunde gelegte Literatur, sind in dieser Arbeit genannt und aufgelistet. Die aus den Quellen wörtlich entnommenen Stellen, sind als solche kenntlich gemacht. Das Thema dieser Arbeit wurde von mir bisher weder im In- noch Ausland einem Beurteiler zur Begutachtung in irgendeiner Form als Prüfungsarbeit vorgelegt. Diese Arbeit stimmt mit der von den Begutachtern beurteilten Arbeit überein. Ich nehme zur Kenntnis, dass die vorgelegte Arbeit mit geeigneten und dem derzeitigen Stand der Technik entsprechenden Mitteln (Plagiat-Erkennungssoftware) elektronisch-technisch überprüft wird. Dies stellt einerseits sicher, dass bei der Erstellung der vorgelegten Arbeit die hohen Qualitätsvorgaben im Rahmen der geltenden Regeln zur Sicherung guter wissenschaftlicher Praxis „Code of Conduct“ an der TU Wien eingehalten wurden. Zum anderen werden durch einen Abgleich mit anderen studentischen Abschlussarbeiten Verletzungen meines persönlichen Urheberrechts vermieden.

Ort, Datum

Unterschrift

Meiner Familie.

Abstract

Biomass gasification is a matter of significant interest in light of the increasing demand for renewable energy and the production of *green* chemicals. In this context, the dual fluidized bed gasification process comes with key advantages compared to other approaches, such as the absence of nitrogen in the product gas, which would lower its heating value.

Steam gasification processes are commonly evaluated based on several key performance indicators such as cold gas efficiency or water conversion. To optimize operation based on these indicators, however, a complete picture of the product gas composition is required, including water content and tars. This presents a challenge, as standard composition analysis equipment is unable to monitor the water content; instead, specialized instrumentation is required. Another approach is to conduct offline sampling, which comes with the downside of providing data only on a point-by-point basis. Process simulation software can also contribute to the understanding and development of the process; however, its computationally demanding nature limits its applicability, rendering it less suited for providing real-time data for plant control.

Soft sensors, on the other hand, can provide model or data-driven estimates of process parameters that are otherwise difficult or costly to obtain. While, in general, soft sensors have long been used successfully in a range of industries, no implementation has been described to date concerning estimating full product gas composition including water content and tar production rate in biomass gasification or indeed a dual fluidized bed gasification plant.

This work presents the development of a soft sensor to augment available measurements with a particular focus on the product gas water and tar contents. The soft sensor is based on an extended Kalman filter (EKF) which estimates the molar flow rates of the products of the gasification process. State prediction is provided by a *Hammerstein* model, which emphasizes the non-linear static relationships while using simple first-order dynamics to describe the time development of the system state. An online analyzer and a gas chromatography (GC) device for product gas analysis, as well as another analyzer for analysis of the flue gas generated in the combustion reactor, are available for state correction. The GC measurements are handled by *extrapolation*, as there is a significant time delay between sampling and the availability of data. An additional EKF is used for disturbance state estimation, with the objective of enhancing the model predictions, leveraging the accuracy of the GC measurements.

Furthermore, a simple heuristic fault detection mechanism based on the EKF's innovation sequence is implemented in order to address a frequently occurring type of fault at the plant.

Finally, the performance of the soft sensor is evaluated based on a gasification test conducted at TU Wien. During the test, the soft sensor demonstrated excellent estimates of the product gas water content, which were verified by offline sampling and compared to process simulation results. The fault detection and isolation also proved to work well, as demonstrated by the fact that erroneous measurements were discarded by the soft sensor, as required. During these *fault periods*, the soft sensor continued to provide reliable estimates of the product gas composition, indicating that the model correction using disturbance states is an appropriate approach to handling constraints resulting from limited knowledge of underlying physical processes. Additionally, the soft sensor demonstrated its ability to meet the required computational performance standards, particularly in terms of the available computation time.

This work will therefore aid in further research and development of the dual fluidized bed process. In particular, the optimization of the plant operation via plant control software will benefit from additional information provided by the soft sensor. Beyond the specific implementation, the general approach of combining limited knowledge of the underlying physical process with data-driven techniques in the modeling phase and established methods of sensor fusion and fault detection may be applied to other types of processes as well, to augment available information for process development.

Kurzfassung

Biomassevergasung gewinnt vor dem Hintergrund steigender Nachfrage nach regenerativer Energie und *grünen* Chemikalien zunehmend an Bedeutung. In diesem Zusammenhang bietet die Zweibett-Wirbelschichtvergasung deutliche Vorteile gegenüber anderen Verfahren, wie beispielsweise die Abwesenheit von Stickstoff im Produktgas, welcher eine Verdünnung darstellt und damit den Heizwert des Produktgases senkt.

Dampf-Vergasungsprozesse werden üblicherweise anhand von *key performance indicators*, wie dem Kaltgaswirkungsgrad oder der Wasserkonversion beschrieben. Um den Betrieb hinsichtlich dieser Indikatoren optimieren zu können bedarf es allerdings der genauen Kenntnis des Wassergehalts im Produktgas. Dies stellt eine gewisse Herausforderung dar, da gängige Analysemethoden für die Produktgaszusammensetzung den Wassergehalt nicht erfassen können, sodass spezielle Messgeräte eingesetzt werden müssen. Andere Methoden, den Wassergehalt zu bestimmen umfassen die manuelle Probenahme und anschließende Analyse im Labor, wobei die Ergebnisse erst mit erheblichem Zeitverzug und nur punktuell zur Verfügung stehen. Prozesssimulationssoftware kann zwar zum Verständnis des Prozesses beitragen, erfordert allerdings erhebliche Rechenleistung und ist daher weniger geeignet um Echtzeitdaten für die Anlagenregelung zu liefern.

Softsensoren sind demgegenüber in der Lage, auf Basis von Modellen oder rein datengestützt, Schätzwerte für Prozessparameter zu liefern, die messtechnisch nur schwer zugänglich sind. Dieser Ansatz ist in der Prozessindustrie bereits seit langem etabliert, allerdings wurden bisher keine Beispiele für die konkrete Aufgabe, den Wassergehalt des Produktgases in Biomassevergasungsprozessen zu bestimmen, beschrieben. Dies gilt insbesondere für die Anwendung in einem Zweibett-Wirbelschichtverfahren.

Im Rahmen dieser Arbeit wird die Entwicklung eins Softsensors vorgestellt, der insbesondere die Messungen der trockenen Produktgaszusammensetzung um Schätzungen des Wassergehalts ergänzt. Die Identifikation des Vergasungsreaktors stützt sich auf Prozessdaten einer Reihe von Testläufen der Zweibett-Wirbelschichtanlage der TU Wien. Das Reaktorsystem wird dabei durch ein Hammersteinmodell abgebildet. Dieser Modellansatz betont die nichtlinearen statischen Zusammenhänge, welche von der Systemdynamik getrennt behandelt werden. Das Hammersteinmodell stellt die Prädiktion für ein Extended Kalman-Filter bereit, welches die Daten dreier Messgeräte für den Korrekturschritt nutzt: ein Analyzer und ein GC (Gaschromatographie)-Gerät für die Bestimmung der Produktgaszusammensetzung und ein weiterer Analyzer, welcher die Abgaszusammensetzung aus dem Verbrennungsreaktor misst. Hierbei werden die GC-Daten besonders behandelt, da diese nur mit erheblicher Zeitverzögerung zwischen Probenahme und Bereitstellung der Daten verfügbar sind. Der Softsensor nutzt die hohe Güte der GC-Daten in erster Linie um Modellkorrekturen vorzunehmen, die in Form von Störgößen auf zukünftige Prä-

diktionen wirken. Um regelmäßig auftretende Fehler erkennen und isolieren zu können, verfügt der Softsensor über einen einfachen heuristischen Erkennungsmechanismus.

Abschließend wird das Verhalten des Softsensors auf Grundlage eines Testlaufs an der Anlage analysiert und bewertet. Über die Dauer des Testlaufs lieferte der Softsensor exzellente Schätzungen für den Wassergehalt im Produktgas, wie anhand von Ergebnissen mehrerer Probenahmen gezeigt werden konnte. Fehlererkennung und -isolation konnten ebenfalls erfolgreich demonstriert werden, und fehlerhafte Messungen wurden entsprechend verworfen. In diesen Szenarien konnten aufgrund der Modellkorrekturen weiterhin solide Schätzungen der Produktgaszusammensetzung geliefert werden. Darüber hinaus konnten die Anforderungen hinsichtlich verfügbarer Rechenleistung durchwegs eingehalten werden, insbesondere in Hinblick auf die Rechenzeit.

Die Ergebnisse der vorliegenden Arbeit können in Zukunft genutzt werden, um Forschung und Entwicklung des Zweibett-Wirbelschichtverfahrens zur Biomassevergasung weiter voranzutreiben. Insbesondere im laufenden Betrieb kann der Prozess mithilfe des Softsensors auch hinsichtlich eingangs genannter Kenngrößen, wie dem Kaltgaswirkungsgrad, optimiert werden.

Content

List of Figures

List of Tables

Symbols

a_i Generic Coefficient
α Confidence level

β_{ij} Element of the element-species matrix

C Generic Constant
χ Split ratio

$\boldsymbol{d}$ Disturbance

ε Error
$\varepsilon_\mathbf{s}$ Solids fraction

$\mathbf{F}$ Static reactor model
$\mathbf{f}$ Static reactor model solution

$\boldsymbol{\Gamma}$ Control input matrix
γ Eigenvalue

H Height
$\boldsymbol{H}$ Measurement sensitivity matrix
$\mathbf{h}$ Output

$\mathbf{I}$ Identity matrix

K Equilibrium constant
$\boldsymbol{K}$ Kalman gain

λ Fault measure

M Molar Mass
$\boldsymbol{M}$ Extrapolation matrix
$\dot{m}$ Mass flow

$\dot{n}$ Mole flow
ν Stoichiometric coefficient

n Number of elements

$\boldsymbol{O}$ Observability matrix

$\boldsymbol{P}$ Estimation error covariance matrix
p Pressure
$\boldsymbol{\Phi}$ State transition matrix

$\boldsymbol{Q}$ Process noise covariance matrix

$\boldsymbol{R}$ Observation noise covatiance matrix
r Regression model
ρ Density

$\boldsymbol{S}$ Stability matrix
$\boldsymbol{\Sigma}$ Innovation sequence covariance matrix

T Temperature
t Time
τ Time constant
θ Threshold
T_s Sampling time

$\boldsymbol{u}$ Model input

$\boldsymbol{v}$ Measurement noise

$\boldsymbol{w}$ Process noise

$\boldsymbol{x}$ System state
ξ Mass fraction
$\underset{\sim}{\xi}$ Mole fraction

$\boldsymbol{y}$ Innovation

$\boldsymbol{z}$ Observation

Indices

ana Analyzer

d Reference to the disturbance state

in Entering flow

st Steam

waf Water-and-ash-free basis
wet Wet basis
wf Water-free basis

x Reference to the system state
xd Reference to the augmented state

Acronyms

BOU Boudouard equilibrium reaction

CR Combustion reactor

DFB Dual fluidized bed

EKF Extended Kalman filter

FG Flue gas

GC Gas chromatography
GR Gasification reactor

ILS Inner loop seal

LLS Lower loop seal

LS Loop seal, referring to both the upper and lower loop seals at the same time

MET Methanation reaction
MS Mass spectrometry

PG Product gas

SMR Steam methane reforming reaction

ULS Upper loop seal

WG Water gas reaction
WGS Water gas shift reaction

1 Introduction

While industrialization led to a steady and ongoing improvement of the social and economic situation in many parts of the world, it was enabled to a great extent by the exploitation of fossil fuel reservoirs to meet rising energy demand and to provide base chemicals for a wide range of industries. Thus, the progress in quality of life has been accompanied by a steady increase in emissions, and a rise in CO_2 levels in the atmosphere. These facts have long been identified to cause average global temperatures to rise, leading to an increase in the number of severe weather phenomena such as floods, hurricanes, and droughts, which can already be observed today [37]. For illustrative purposes, some indicators of human progress are displayed in Figure 1.1.

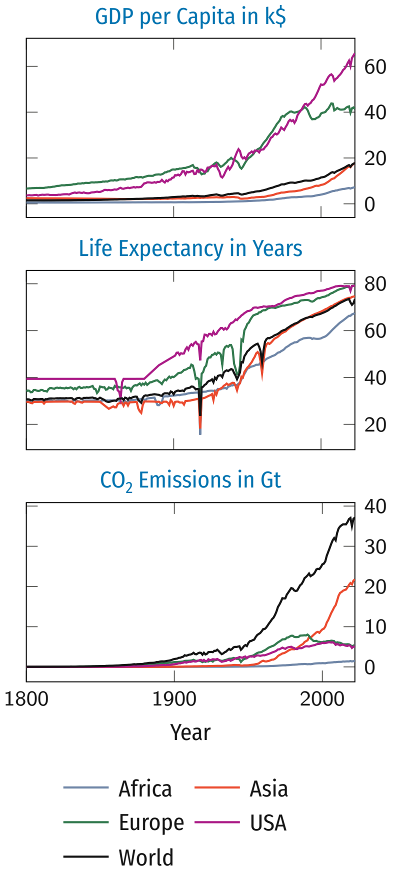

Figure 1.1: GDP per capita based on purchasing power parity [35] life expectancy at birth [30] and cumulative global CO_2 emissions [1] for select world regions since 1800.

In addition to their use as energy carriers, fossil fuels serve as the basis for a wide range of chemical products. For this purpose, fossil fuels are converted to *syngas*, a mixture of H_2 and CO, by steam reforming or partial oxidation, which forms the starting point for the synthesis of a range of chemical products including methanol, aldehydes, and ammonia. In contrast, the Fischer-Tropsch process makes it possible to produce liquid hydrocarbons from syngas, which can be used as fuel in conventional engines. Since modern society's dependence on this particular resource cannot be easily resolved, great efforts are being made to substitute fossil fuels by renewable sources.

One such approach is the gasification of municipal or agricultural waste, or other biomass like wood. Steam gasification involves the reaction of carbonaceous material with steam at elevated temperatures of 700 °C to 1000 °C, depending also on the type of reactor [29, 44]. This reaction produces valuable product gas, which contains high amounts of H_2 and CO. This product gas may replace synthesis gas produced by steam reforming of fossil fuels or used directly for energy production. Since this reaction is overall endothermic, heat needs to be supplied, which is generally achieved by oxidizing a portion of the fuel using air or pure oxygen. Traditionally, both the gasification and oxidization take place in the same reactor. The use of air in lieu of oxygen is accompanied by the disadvantage of nitrogen diluting

[37] Seneviratne et al., "Weather and Climate Extreme Events in a Changing Climate." (2021).

[29] Mishra et al., "Review on biomass gasification: Gasifiers, gasifying mediums, and operational parameters." (2021).

[44] Wang, *Sustainable Bioenergy Production*. (2014).

[35] Gapminder (2023).

[30] Gapminder (2023).

[1] Global Carbon Budget (2023) – with major processing by Our World in Data.

the product gas, which consequently results in a reduction of the heating value.

To address this issue, a novel dual fluidized bed (DFB) gasification plant is subject to research at TU Wien. In order to optimize the process, it is crucial to obtain as much information about the operating parameters as possible. In particular, a number of key performance indicators are used in the analysis of gasification process performance, such as water conversion and cold gas efficiency, which is usually evaluated on a dry, i.e., wf (water-free) product gas basis [44, p. 349]. Both measures require detailed information about the composition of inbound and outgoing flows. In this context the water content of the product gas is a crucial quantity, however, monitoring is not possible with standard gas analysis equipment but requires special instrumentation [5, 17]. A different method, which is pursued at TU Wien, involves offline water sampling. This method necessitates the manual collection and analysis of samples, resulting in a significant delay before results become available. Process simulation software, like IPSEpro, can aid in addressing this issue by validating measurements or employing parameter studies, which are otherwise time-consuming and expensive to conduct with a real plant. Yet, this approach entails significant demand with respect to computational cost. Consequently, neither offline sampling nor process simulation allows for optimizing plant control during operation by control software.

[5] Cherednichenko et al., *Online water vapor detection in the product gas from indirect gasification*. (2013).

[17] Karellas et al., "Analysis of the product gas from biomass gasification by means of laser spectroscopy." (2007).

An alternative to the aforementioned solutions is to represent the process in question by a mathematical model. As elaborated in [9, p. 3], this may be accomplished using "mechanistic modeling (physical modeling), multivariate statistics, and artificial intelligence modeling such as neural networks, fuzzy logic and hybrid methods." They also emphasize the value of empirical or data-driven models in industrial applications, "due to the complexity of the plant dynamics, which can prevent the first principles approach from being used." These models may be implemented in software to generate estimates of process variables, thus circumventing the need for specialized equipment while still providing online data for plant control. Such an implementation is commonly referred to as a *soft sensor*.

[9] Fortuna et al., *Soft Sensors for Monitoring and Control of Industrial Processes*. (2007).

In addition to augmenting existing information on processes, soft sensors can be used for detecting faults in hardware sensors. In [13], the authors distinguish two different approaches in this context. Model-free methods include limit checking and spectrum analysis of sensor readings. Model-based methods, on the other hand, typically leverage the concept of analytical redundancy, where "sensory measurements are compared to analytically computed val-

[13] Gertler, *Fault detection and diagnosis in engineering systems*. (1998).

ues of the respective variable. [...] the resulting differences, called *residuals*, are indicative of the presence of a fault in the system."

Soft sensors have long been established in the process industry [15, 34]. With regard to gasification, a number of studies have been published. In [42] the authors describe a Kalman filter-based approach to estimate temperature profiles and slag formation in an entrained-flow gasification system with acceptable results. Another publication discusses a vision-based soft sensor for estimating major species concentrations in entrained flow gasification reactors using machine learning techniques [32]. Various methods have been presented addressing the issue of fluctuating biomass composition and moisture content based on energy balance evaluation [22] or by employing automated machine learning [19].

However, an application for monitoring product gas composition in biomass steam gasification, and in particular its water content has not yet been presented. The present work describes the development, implementation and performance evaluation of a soft sensor for providing accurate estimates of the product gas composition, including water content, as well as for the char and tar production rates.

To this end, the DFB gasification process is described in Chapter 2, covering incoming and outgoing material flows as well as the measurements processed by the soft sensor. The model identification process is discussed in Chapter 3. The extraction of suitable data from historic gasification tests and necessary preprocessing are covered in this chapter, followed by the identification of a number of static linear models to describe the gasification process and their incorporation into a Hammerstein model. Chapter 5 describes the design of the extended Kalman filter (EKF)-based observer forming the core of the soft sensor. This chapter concludes with a description of the software implementation of the observer. The performance of the soft sensor is evaluated based on a gasification test in Chapter 6, discussing its prediction accuracy, stability, observability and controllability of the observer, as well as computational performance. A brief analysis of the dynamic behavior of the soft sensor output is included as well. The chapter concludes with a summary of suggestions for improvement of the soft sensor. The work closes by highlighting the obstacles overcome by the soft sensor and argues for the prospective benefits of the implementation in Chapter 7.

[15] Kadlec et al., "Data-driven Soft Sensors in the process industry." (2009).

[34] Rogina et al., "Soft sensor for continuous product quality estimation (in crude distillation unit)." (2011).

[42] Valipour et al., "State estimation and sensor location for Entrained-Flow Gasification Systems using Kalman Filter." (2021).

[32] Ögren et al., "Development of a vision-based soft sensor for estimating equivalence ratio and major species concentration in entrained flow biomass gasification reactors." (2018).

[22] Kortela et al., "Fuel moisture soft-sensor and its validation for the industrial BioPower 5 CHP plant." (2013).

[19] Kim et al., "Predicting biomass composition and operating conditions in fluidized bed biomass gasifiers: An automated machine learning approach combined with cooperative game theory." (2023).

2 Plant Description

The key distinction between the DFB plant under consideration in this work and established allothermal gasification systems is the separation of the steam gasification of the fuel and the combustion by which heat is provided for the overall endothermic gasification reaction. It is a major advantage of this approach that no air is introduced into the gasification zone. This means that the product gas (PG) is free of N_2 that would reduce its heating value through dilution. The following chapter provides a concise overview of the process to the extent necessary within the scope of this work.

2.1 Process Description

The two main components of the DFB plant are the gasification reactor (GR) and the combustion reactor which are depicted in the diagram in Figure 2.1. Softwood pellets (subsequently referred to as *fuel*) are fed by a screw conveyor onto the bubbling fluidized bed at the bottom of the gasification reactor. Fluidization of the bed material, which consists of a mixture of 80 % olivine and 20 % limestone, is facilitated by superheated steam, that enters at the bottom of the gasification reactor and also acts as the gasification agent.

Within the bubbling bed, an illustration of which can be observed in Figure 2.2, several steps are involved in the conversion of the fuel, a detailed description of which is given in [21]. Initially, the fuel is heated up and dried, releasing its water content of $\xi_{H_2O} \approx 7.2\,\%$. With increasing temperature, the fuel undergoes *pyrolytic decomposition*, also referred to as *devolatilization*, leading to the formation of permanent gases, such as CO, CO_2, H_2 and light hydrocarbons C_xH_y. Additionally, the formation of condensable hydrocarbons, i.e., tars, and solid char occur as part of this second step. The third phase involves both homogeneous and heterogeneous reactions of the intermediates with the gasification agent, in this case steam. Additionally, biomass also contains inorganic compounds that lead to the formation of ash.

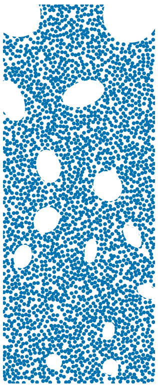

Figure 2.2: Illustration of the bubbling regime adapted from [26].

[21] Koppatz, "Outlining active bed materials for dual fluidised bed biomass gasification: in-bed catalysts and oxygen/carbonate looping behaviour." (2012).

[26] Lim et al., "Hydrodynamics of gas-solid fluidization." (1995).

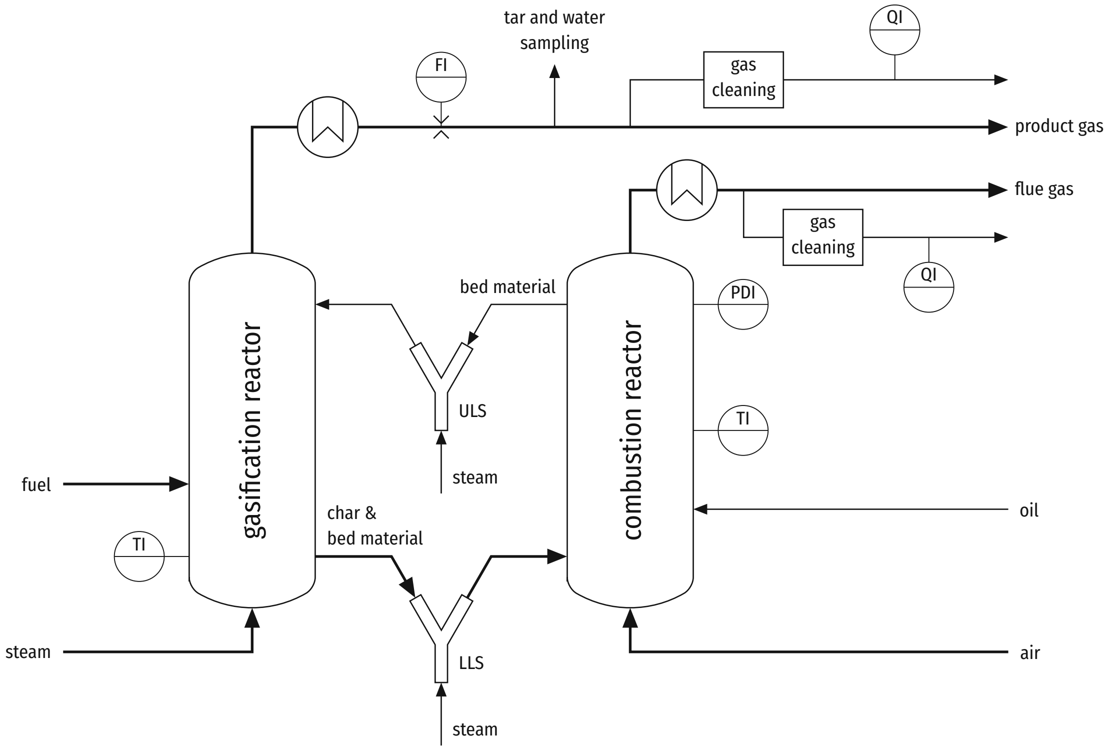

Figure 2.1: Simplified flow diagram of the DFB gasification plant comprising the gasification reactor and the combustion reactor, which are connected via the lower loop seal (LLS) and upper loop seal (ULS) (adapted from [43]).

[43] Vogler et al., “Soft Sensor Design for Product Gas Composition Monitoring Including Fault Isolation in a Dual Fluidized Bed Biomass Gasifier.” (2023).

In the advanced DFB gasification process, the reaction products comprising the product gas rise through a countercurrent column and exit at the top where entrained bed material, fly char and ash are separated in a gravity separation chamber and fed back into the gasification reactor through an internal steam fluidized loop seal (ILS). Subsequently, fine ash is removed from the product gas by means of a cyclone (not depicted in Figure 2.1) and discharged from the gasification reactor. A detailed diagram of the reactor system showing the arrangement of both reactors can be observed in [28].

[28] Mauerhofer et al., “Dual fluidized bed steam gasification: Change of product gas quality along the reactor height.” (2019).

After removal of particulates, the product gas, comprising primarily H_2, CO, CO_2, CH_4, C_2H_6, C_2H_4, N_2, H_2O and trace amounts of O_2, passes through a radiation cooler after which a sampling line is installed. Since the product gas contains condensable tars and water, as well as some remaining particulate matter, it undergoes cleaning prior to composition analysis. The gas cleaning involves filtering particulates and subsequent condensation of water and tar in a series of impinger bottles containing rapeseed oil methyl ester. A detailed description of the procedure is given in [18].

[18] Kern et al., “Gasification of wood in a dual fluidized bed gasi-

Unconverted char and bed material are continuously extracted from the fluidized bed and pass through a lower fier: Influence of fuel feeding on process performance." (2013).

steam fluidized loop seal (LLS) into the combustion reactor, where air is added to facilitate the combustion. The heat generated by the combustion reaction is absorbed by the bed material, which is entrained in a fast fluidization regime and separated from the flue gas (FG) in a gravity separator at the top of the combustion reactor to be fed back, via an upper steam fluidized loop seal (ULS), into the countercurrent column of the gasification reactor to maintain the endothermic gasification reaction.

Combustion air enters the combustion reactor at three different points along the lower part of the combustion reactor, with primary air entering at the lowest point and tertiary air at the highest point. Fuel oil can also be fed into the combustion reactor to compensate "for the relatively high specific heat losses in this small pilot plant and enables control of the gasification temperature for the gasification experiments [3]."

[3] Benedikt et al., "Fuel flexible gasification with an advanced 100 kW dual fluidized bed steam gasification pilot plant." (2018).

Downstream of the combustion reactor, the flue gas, comprising mainly N_2, H_2O, CO_2 and O_2, passes another cyclone and a subsequent radiation cooler before being sampled.

Several measurements are available for monitoring and controlling plant operation, some of which are shown in the block diagram in Figure 2.1.

2.1.1 Gas composition

The product gas composition is sampled every 5 s from a Rosemount NGA 2000 device. In addition, a gas chromatography (GC) takes samples approximately every 12 min. As can be seen in Table 2.1, the set of species available from each of the different devices is different. Notably the H_2O concentration cannot be observed in real time but is instead measured offline at varying intervals. Also, the GC does not capture the H_2 concentration in the product gas whereas the analyzer does not provide a value for the N_2 concentration. Flue gas composition is likewise monitored by an analyzer of the same type but not by a GC.

Table 2.1: Available product gas composition measurements.

Species	Analyzer	GC
H_2	✓	✗
CO	✓	✓
CO_2	✓	✓
CH_4	✓	✓
C_2H_6	✓*	✓
C_2H_4	✓*	✓
H_2O	✗	✗
O_2	✓	✓
N_2	✗	✓

* not available in all data sets.

Tar In the context of this work, *tar* is understood to cover "hydrocarbons with a molecular weight higher than benzene" [27, p. 2]. According to quantitative analysis the most prominent species in this fraction is naphtalene.

[27] Maniatis et al., "Tar Protocols. IEA Bioenergy Gasification Task." (2000).

One of the tar sampling points is located downstream of the product gas cooler as depicted in Figure 2.1. The second sampling point (not shown in the diagram) allows to sample the reaction mixture just above the bubbling bed. The sampling is performed by absorption of tar components in a suitable solvent (toluene in this case, which excludes BTX-compounds from analysis). Since the solvent is cooled, BTX refers to benzene, toluene and xylene.

water condenses as well, allowing for the simultaneous determination of the water content. Quantification of the tar fraction is performed by both thermogravimetric analysis and GC/mass spectrometry (MS). The procedure is detailed in [20].

[20] Kolbitsch, "First fuel tests at a novel 100 kWth dual fluidized bed steam gasification pilot plant." (2016).

Product Gas Mass Flow The product gas mass flow is measured using a quarter circle nozzle specified in [7]. The device geometry shown in Figure 2.3, is specifically designed to measure low Re number flow rates as the discharge coefficient is only dependent on nozzle geometry. However, the expansibility factor depends on material parameters and, consequently, on the product gas composition.

[7] VDI/VDE 2041:1991 – *Durchflussmessung mit Drosselgeräten*.

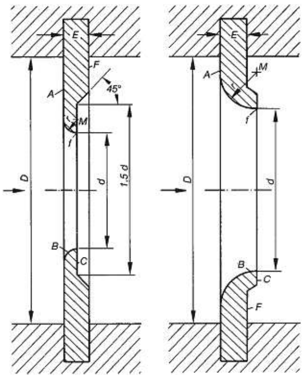

Figure 2.3: Quarter circle nozzle taken from [7]. The term refers to the rounded edge of the orifice opening which prescribes a quarter circle in the cross-section.

Char Since there is no practical way to measure the flow rate of char from the gasification reactor to the combustion reactor, it is a quantity to be determined as part of the modeling process.

Fuel Oil The fuel oil is fed to the combustion reactor by a peristaltic pump hence the flow rate is determined by the rotational speed of the pump.

Circulation Rate The circulation rate refers to the flow rate of bed material exchanged between the two reactors. One aspect is that the circulation rate influences how much char is transported to the combustion reactor and consequently how much heat is generated and transferred back to the gasification reactor. The circulation rate has been shown to strongly correlate with the pressure drop in the top section of the combustion reactor [12]. The nature of this correlation is depicted in Figure 2.4. Since the pressure drop is easily measurable, it is used in the modeling of the plant.

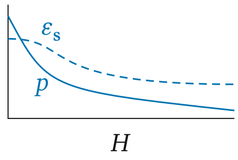

Figure 2.4: Pressure p and solids fraction ε_s as function of riser height H. Adapted from Kunii et al. [24, p. 87].

[12] Fuchs et al., "A general method for the determination of the entrainment in fluidized beds." (2018).

The circulation can be controlled by varying the air flow rate to the combustion reactor. In particular—unlike the simplified illustration in Figure 2.1 suggests—primary, secondary and tertiary air feed lines are installed and can be controlled independently. By increasing the primary air flow rate, thus feeding a larger fraction of the total air flow to the very bottom of the combustion reactor, particle entrainment and thus circulation rate will also increase.

Fuel Feed Rate Fuel is conveyed from one of the fuel feed hoppers onto the bubbling bed by means of a screw conveyor. Based on the rotational speed of the screw conveyor, the fuel feed rate can be calculated.

Temperature Measurements A number of temperature probes are arranged in the bubbling bed as well as along the height of the reactor columns. The two temperatures most indicative of the gasification process are the ones in the bubbling bed in the gasification reactor and at the top of the combustion reactor column [38].

[38] Stanger et al., "Dynamic modeling of dual fluidized bed steam gasification for control design." (2023).

Steam Flow Rate Steam enters the gasification reactor mainly below the bubbling bed, acting as gasification and fluidization agent. An additional amount is fed into the loop seals. While the amount of steam entering via the inner loop seal (ILS) is directly measurable, it is not known how much of the steam fed into the LLS and ULS enters the gasification reactor as opposed to the combustion reactor.

3 Data Compilation and Processing

The aim is to identify a mathematical model of the gasification reactor that can predict the product gas composition depending on the current state and the reactor input parameters. A critical requirement is the robustness of the model, i.e., the model should handle *extreme* input values in such a way that the model output is within physical constraints.

3.1 Data Selection for Identification

Since the DFB plant should deliver insight into a number of different areas of research, numerous trial runs have been conducted using a range of different bed materials and fuels. Consequently, to have a common basis identifying the gasification reactor model, only those data sets where the same bed material and fuel were used are selected.

From the data sets available after the aforementioned exclusions, only those data points are selected where the plant was in *steady-state* operation to be able to identify the stationary model parameters. Steady-state operation was determined by visually evaluating a set of predetermined key operating parameters, namely:

- Fuel, steam, and air flow rates
- Gasification and combustion temperatures
- Circulation rate as indicated by the pressure drop in the top section of the combustion reactor (see Section 2.1).
- Main components compositions

Sample points were specified as average values over 5 min to 20 min intervals of steady-state operation. The sample points obtained in this manner are used to identify the stationary model parameters as explained in Section 4.2.1.

To illustrate this procedure, one particular data set is displayed in Figure 3.1. The diagram shows data from a trial run on March 17, 2021 and covers a period of approximately 9 h. Both air and oil flow rates were increased within the first

Equivalent diagrams for the remaining data sets considered in this work can be observed in Appendix D.

1.5 h while the fuel flow rate was held constant throughout. The steam flow rate was varied slightly in several instances. During this period the input streams of fuel, steam, air, and oil were held more or less constant.

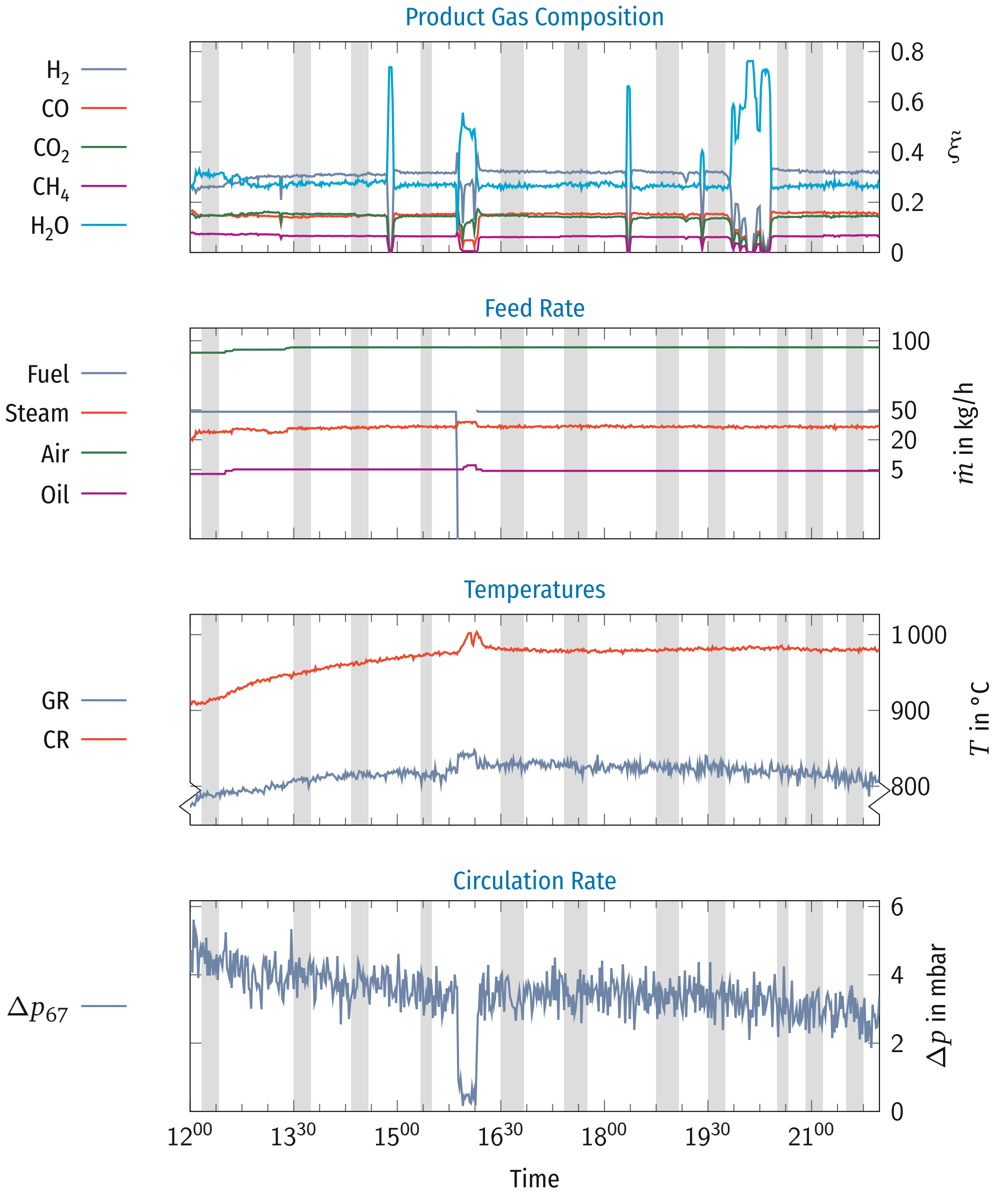

Figure 3.1: Test run on March 17, 2021. *Steady-state* sample intervals are highlighted by ▨.

As evidenced by the highlighted areas in the diagrams, the aforementioned criteria are not strictly met, especially concerning the combustion reactor temperature, which rises from 910 °C to 1000 °C during the first 4 h of operation. Since the temperature changes happened gradually their changing effect on the chemical reactions' parameters was considered minor, allowing for the inclusion of the highlighted periods in the identification data.

3.2 Preprocessing

Mainly due to limitations in the data collection, as discussed in Section 2.1, some preprocessing is required to ensure physical consistency. In the context of this work, this pertains to the mass balance in particular. The following section details the assumptions made as well as the strategies employed to reconstruct missing data.

3.2.1 Mass Balances

The first and most crucial step preceding the model identification is the evaluation of the gasification reactor mass balance. Here, the primary challenge originates from the lack of full knowledge about all input and output streams in addition to incomplete measurements of product gas and flue gas compositions as has been described in Section 2.1. In particular, the water content of both gas streams is unknown except for point-by-point data on the product gas water and tar contents from offline measurements. While the char flow rate transferred between the reactors cannot be measured, it can be recovered from the carbon balance around the combustion reactor. The overall mass balance for the two reactors can be formulated as follows:

$$\Delta \dot{m}^{\mathrm{GR}} = \dot{m}_{\mathrm{fuel}} + \dot{m}_{\mathrm{st}}^{\mathrm{GR,LS}} - \dot{m}_{\mathrm{PG}} - \dot{m}_{\mathrm{char}} - \dot{m}_{\mathrm{tar}} \,, \tag{3.1a}$$

$$\Delta \dot{m}^{\mathrm{CR}} = \dot{m}_{\mathrm{char}} + \dot{m}_{\mathrm{oil}} + \dot{m}_{\mathrm{air}} + \dot{m}_{\mathrm{st}}^{\mathrm{CR,LS}} - \dot{m}_{\mathrm{FG}} \,, \tag{3.1b}$$

where $\dot{m}$ denotes mass flow rates. The amounts of steam entering the gasification reactor and combustion reactor, respectively depend on the split ratio $\chi_{\mathrm{LS}} = \chi_{\mathrm{LLS}} = \chi_{\mathrm{ULS}}$, which is assumed to be equal for the LLS and the ULS.

In eqn. (3.1)

$$\dot{m}_{\mathrm{st}}^{\mathrm{GR,LS}} = \dot{m}_{\mathrm{st}} + \chi_{\mathrm{LS}} \left(\dot{m}_{\mathrm{st}}^{\mathrm{LLS+ULS}} \right)$$

$$\dot{m}_{\mathrm{st}}^{\mathrm{CR,LS}} = (1 - \chi_{\mathrm{LS}}) \left(\dot{m}_{\mathrm{st}}^{\mathrm{LLS+ULS}} \right)$$

holds, where the index LS refers to both the LLS and ULS.

While the differences between incoming and outgoing mass for both reactors, $\Delta \dot{m}^{\mathrm{GR}}$ and $\Delta \dot{m}^{\mathrm{CR}}$ should eq equal to 0 due to conservation of mass, the same principle applies to the flows of the individual elements C, H, O, and N. The element balances can be written using index notation:

$$\Delta \dot{n}_i = \beta_{ij} \, \Delta \dot{n}_j \,. \tag{3.2}$$

β_{ij} designates one element of the *element-species matrix* where its value equals the number of atoms of the element i in the species j. Here, i takes the values C, H, O and N while j takes the values H_2, CO, CO_2, etc.

It is important to note that in this work the bed material is assumed to be inert. This stands in contradiction to findings in literature [11, 33] where it has been demonstrated that exposure of olivine to oxidizing gases such as O_2, H_2O or CO_2 will lead to the formation of various iron oxides on the surface of the mineral particles. Consequently, exposure to reducing gases like CO and H_2 will reduce the iron oxides up to free iron, whereas an oxidizing atmosphere will produce iron oxides on the particle surface. Therefore, there should be net transport of oxygen from the combustion reactor

[11] Fredriksson et al., "Olivine as tar removal catalyst in biomass gasification: Catalyst dynamics under model conditions." (2013).

[33] Pecho et al., "Elucidation of the function of olivine in biomass gasification." (2004).

to the gasification reactor. An important argument for the application of olivine as bed material in DFB plants is its capability of reducing tar in the product gas and increasing the yield of desired CO and H_2. This has been attributed mainly to the formation of Ca deposits on the bed material due to contact with biomass ash [4, 23]. However, for the TU Wien DFB plant, the catalytic effect of the bed material on the formation of CH_4 has been found to be insignificant in previous works [4].

[4] Benedikt et al., "Assessment of correlations between tar and product gas composition in dual fluidized bed steam gasification for online tar prediction, biomass." (2019).

[23] Kuba et al., "Influence of coated olivine on the conversion of intermediate products from decomposition of biomass tars during gasification." (2016).

Char Production Rate

It is crucial to have information about the production rate of char in relation to the operating parameters when modeling the product gas composition. As discussed earlier, it is not possible to determine the char production rate solely from the gasification reactor mass balance without affecting the combustion reactor mass balance. To close the mass balance, several assumptions are made:

1. Feed, steam, oil, and air flow measurements are assumed to be accurate.
2. Product gas and flue gas flow measurements are assumed to not be accurate.
3. Water content in both product gas and flue gas are assumed to not be accurate.
4. The split ratio is initially assumed to be $\chi^0_{\mathrm{LS}} = 0.5$. However, this assumption is later revised on the basis of comparison with offline data (see Section 4.2.1).

Neither water nor N_2 concentrations are consistently available. However, the product gas concentration influences the calculation of the mass flow through the orifice from the measured pressure drop as defined in [7]. Therefore, the product gas and flue gas flow rates in the historical data are assumed to be inaccurate.

Consequently, the water concentrations in both product gas and flue gas were treated as free variables to be determined in such a way that conservation of mass is satisfied.

Finally, the N_2 mass flow resulting from the flushing of the temperature and pressure probes is unknown and thus was treated as a variable quantity. For this purpose, the N_2 concentration was approximated by

$$\begin{gathered} \xi_{\mathrm{N_2}} \approx 1 - \sum_i \xi_i, \quad \text{where} \\ i \in \mathscr{I} = \{\mathrm{H_2, CO, CO_2, CH_4, C_2H_6, C_2H_4, H_2O, O_2}\}, \end{gathered} \tag{3.3}$$

using the available measurements.

The aforementioned assumptions can be summarized in the following optimization problem, where the error in the molar flow rates of each element (C, H, O, and N) $\Delta\dot{n}_i$ is weighted by the corresponding molar flow entering the reactor $\dot{n}_i^{\mathrm{in}}$.

$$\begin{aligned}
\min f\left(\boldsymbol{x}_k\right) &= \left\| \begin{bmatrix} \Delta\dot{\boldsymbol{n}}^{\mathrm{GR}} \oslash \dot{\boldsymbol{n}}^{\mathrm{GR}}_{\mathrm{in}} \\ \Delta\dot{\boldsymbol{n}}^{\mathrm{CR}} \oslash \dot{\boldsymbol{n}}^{\mathrm{CR}}_{\mathrm{in}} \end{bmatrix}_k \right\|_2^2 , \\
\text{where} \quad \boldsymbol{x}_k &= \left[\dot{n}_{\mathrm{PG}}\ \dot{n}_{\mathrm{FG}}\ \dot{n}_{\mathrm{char}}\ \dot{n}_{\mathrm{N_2}}\ \tilde{\xi}^{\mathrm{PG}}_{\mathrm{H_2O}}\ \tilde{\xi}^{\mathrm{FG}}_{\mathrm{H_2O}} \right]^{\top}_k , \\
\text{subject to} \quad \boldsymbol{g}\left(\boldsymbol{x}_k\right) &= \begin{bmatrix} (0 \le \dot{n}_{\mathrm{PG}} \le 4.5)\,\mathrm{kmol/h} \\ (0 \le \dot{n}_{\mathrm{FG}} \le 4.5)\,\mathrm{kmol/h} \\ (0 \le \dot{n}_{\mathrm{char}} \le 1)\,\mathrm{kmol/h} \\ (0 \le \dot{n}_{\mathrm{N_2}} \le 0.2)\,\mathrm{kmol/h} \\ 0 \le \tilde{\xi}^{\mathrm{PG}}_{\mathrm{H_2O}} \le 1 \\ 0 \le \tilde{\xi}^{\mathrm{FG}}_{\mathrm{H_2O}} \le 1 \end{bmatrix} .
\end{aligned} \tag{3.4}$$

The vector of molar flow rates is constructed as follows:

$$\dot{\boldsymbol{n}} = \left[\dot{n}_{\mathrm{C}}\ \dot{n}_{\mathrm{H}}\ \dot{n}_{\mathrm{O}}\ \dot{n}_{\mathrm{O}} \right]^{\top} .$$

$\oslash$ denotes *Hadamard divison*, i.e., element-wise devision which is implemented in MATLAB as `./`.

The solution to problem eqn. (3.4) is obtained through the use of MATLAB's `fmincon` with its default algorithm `interior-point`. The constraints $\boldsymbol{g}\left(\boldsymbol{x}\right)$ were put in place to ensure sensible solutions. The lower bounds for the molar flow rates are physically meaningful since the signs indicate the flow direction (see eqn. (3.1)). The upper bounds, on the other hand, were chosen arbitrarily but generously to limit the solution set in order to aid the solver. In case of the product gas and flue gas water contents, both lower and upper bounds represent physical bounds. The algorithm uses a variety of different concepts in nonlinear programming to efficiently solve the problem [40].

[40] The MathWorks, *Constrained Nonlinear Optimization Algorithms*.

Figure 3.2 shows the molar element balance for both reactors before and after solving (3.4). The data shown is compounded from all steady-state periods which are selected according to the procedure described in Section 3.1.

Prior to the correction, the char flow rate is unknown, resulting in a positive C balance for the gasification reactor. This indicates that more carbon is entering the reactor than exiting. The opposite is true for the C balance for the combustion reactor.

In the pre-correction evaluation of the material balance of the gasification reactor, the water content $\tilde{\xi}^{\mathrm{PG}}_{\mathrm{H_2O}}$ was assumed to remain constant in between offline measurements. In absence of offline measurements, a value of $\tilde{\xi}^{\mathrm{PG}}_{\mathrm{H_2O}} = 0.4$ was assumed. These simplifications likely caused the errors in the H and O balances to be significant for the gasification reactor.

In the case of the pre-correction combustion reactor balance, a value of $\tilde{\xi}^{\mathrm{FG}}_{\mathrm{H_2O}} = 0.1$ is assumed, while it is also consid-

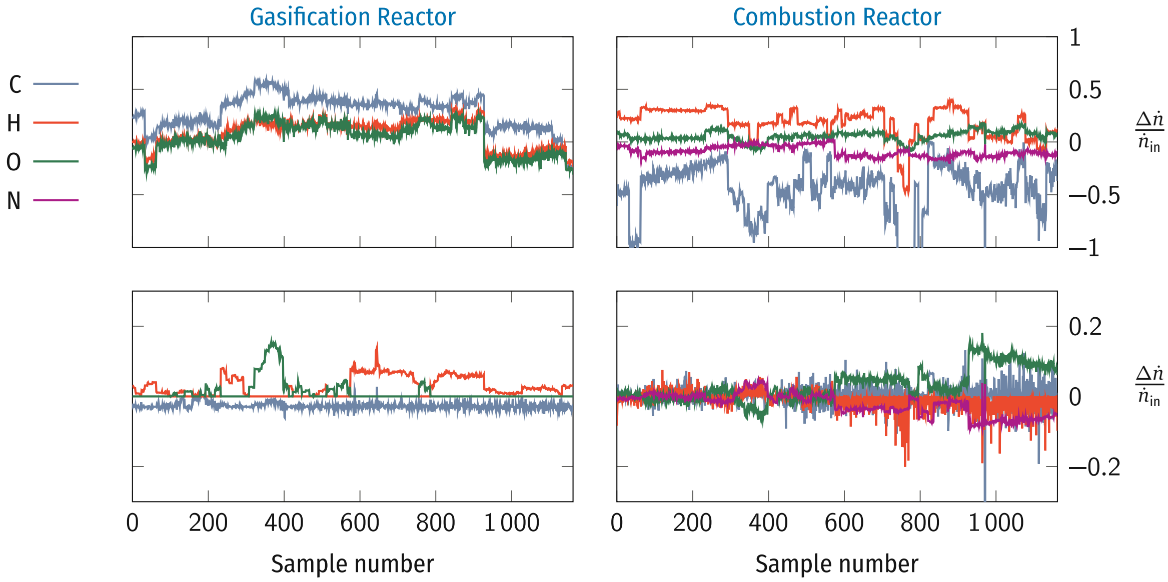

Figure 3.2: Molar element balance before (top) and after (bottom) correction for gasification reactor and combustion reactor, respectively. The data is assembled from all steady-state points and is not contiguous. Note that in case of the pre-correction gasification reactor balance N_2 is not displayed for the sake of reasonable axis scaling.

ered a variable quantity to be determined through solving the material balance.

Both post-correction balances show significantly lower residual errors, however, it is evident that under the assumptions made, the errors could not be eliminated completely.

4 Hammerstein Model Identification

During operation, the plant will generally operate in a steady state once a set point is reached. Consequently, dynamic changes in the product gas composition are expected to only occur during set point changes, such as adjustments in fuel feed rate. It is thus reasonable to emphasize the static relationship between model inputs and outputs over the system dynamics and treat both components separately.

One such approach is the *Hammerstein* model in which the input-output relationship is decomposed into a static nonlinear block and a dynamic linear block, which are connected in series. The general structure can be observed in Figure 4.1. This approach has been successfully applied to the identification of chemical systems [8].

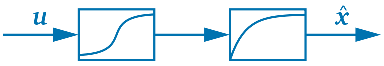

Figure 4.1: Block diagram of a Hammerstein model.

[8] Eskinat et al., "Use of Hammerstein models in identification of nonlinear systems." (1991).

In the following section, Section 4.1, the model input and the system state are defined. In Section 4.2, the identification of several linear regression models will be described. Each of these models describes a particular static relation between the system inputs and the corresponding outputs e.g., the chemical reactions involved in the conversion of the biomass fuel to the desired product gas and the char production rate. Subsequently, the way these linear models are combined into a single static nonlinear model will be detailed. An alternative model will also be described, which is used by the soft sensor in the event of an interruption in the fuel feed rate. Several disturbances, which are introduced to enhance the prediction accuracy of the model will be described in Section 4.2.4, as well as the way they act on the static part of the Hammerstein model. Finally, the modeling of the system dynamics as part of the Hammerstein model will be described.

4.1 Model Inputs and System States

The major input variables for the reactor system were chosen as follows

$$\begin{aligned} \boldsymbol{u} = \big[\dot{m}_{\text{fuel}} \quad \dot{m}_{\text{st}} \quad T_{\text{GR}} \quad T_{\text{CR}} \quad \dot{m}_{\text{air}} \quad \dots \\ \dots \quad \dot{m}_{\text{oil}} \quad \Delta p_{67} \quad \dot{m}_{\text{st}}^{\text{LS}} \quad \Delta p_{\text{GR-CR}}\big]^{\top}. \end{aligned} \tag{4.1}$$

Here $\dot{m}_{\mathrm{fuel}}$ and $\dot{m}_{\mathrm{st}}$ denote the fuel and steam mass flow rates fed directly into the gasification reactor as shown in Figure 2.1. The gasification temperature T_{GR} is measured just below the top of the bubbling bed. This has proven to be a reliable indicator for the performance of the gasification process [20]. This makes sense since the chemical conversion of the fuel mainly takes place in this zone due to good mixing, promoting both mass and heat transfer.

The combustion temperature T_{CR}, on the other hand, is sampled at the top of the combustion reactor column.

As discussed in Section 2.1, the circulation rate is substituted by the pressure drop Δp_{67} in the upper part of the combustion reactor.

On top of that, the air and oil flow rates, $\dot{m}_{\mathrm{air}}$ and $\dot{m}_{\mathrm{oil}}$, also enter the model.

The total amount of steam to the LLS and ULS, $\dot{m}_{\mathrm{st}}^{\mathrm{LS}}$, and the pressure difference between the two reactors, $\Delta p_{\mathrm{GR-CR}}$, will be used to predict the amount of steam entering the gasification reactor through the loop seals.

While the main goal is to estimate the product gas composition, the material balance should close at all times to ensure a physically reliable prediction. Therefore, the outgoing gas flow rates were chosen over the concentrations to comprise the system state. To be able to observe the amount of char transferred from the gasification reactor to the combustion reactor, it is necessary to include the flow rates of the main flue gas components as well. The system state $\boldsymbol{x}$ is therefore defined to comprise the molar flows of the product gas components, H_2, CO, CO_2, CH_4, C_2H_6, C_2H_4, O_2, N_2, and H_2O; the molar flow rate of char $\dot{n}_{\mathrm{char}}$ transported to the combustion reactor; the molar flow rate of tar $\dot{n}_{\mathrm{tar}}$ in the product gas; and the molar flow rates of the main flue gas components, O_2, CO_2, N_2 and H_2O. The mass flow of steam entering the gasification reactor through the LLS and the ULS, $\dot{m}_{\mathrm{st}}^{\mathrm{GR,LS}}$ is included in the system state for evaluation purposes and is not influenced by the other states. This results in a total of 16 individual states.

$$\boldsymbol{x} = \begin{bmatrix} \dot{n}_{\mathrm{H_2}}^{\mathrm{PG}} \\ \dot{n}_{\mathrm{CO}}^{\mathrm{PG}} \\ \dot{n}_{\mathrm{CO_2}}^{\mathrm{PG}} \\ \dot{n}_{\mathrm{CH_4}}^{\mathrm{PG}} \\ \dot{n}_{\mathrm{C_2H_6}}^{\mathrm{PG}} \\ \dot{n}_{\mathrm{C_2H_4}}^{\mathrm{PG}} \\ \dot{n}_{\mathrm{O_2}}^{\mathrm{PG}} \\ \dot{n}_{\mathrm{N_2}}^{\mathrm{PG}} \\ \dot{n}_{\mathrm{H_2O}}^{\mathrm{PG}} \\ \dot{n}_{\mathrm{char}} \\ \dot{n}_{\mathrm{tar}} \\ \dot{n}_{\mathrm{O_2}}^{\mathrm{FG}} \\ \dot{n}_{\mathrm{CO_2}}^{\mathrm{FG}} \\ \dot{n}_{\mathrm{N_2}}^{\mathrm{FG}} \\ \dot{n}_{\mathrm{H_2O}}^{\mathrm{FG}} \\ \dot{m}_{\mathrm{st}}^{\mathrm{GR,LS}} \end{bmatrix}$$

4.2 Static Reactor Model

Utilizing the results from Section 3.2.1, several linear relationships between the plant inputs and the system state, i.e., the products' molar flow rates, were identified. In this context, knowledge about the chemical reactions involved in the gasification of the fuel is leveraged; while some of the models are formulated following a purely data-driven approach. The aim is to combine the linear models into a single nonlinear static model to form the first block of the Hammerstein model structure.

4.2.1 Linear Model Identification

From the data compiled as described in Section 3.2, two distinct subsets are formed. The total number of 86 steady-state points is initially randomly ordered and subsequently divided into an identification data set and a validation data set, allocating one in every four samples to the validation data set.

General Approach

The identification data is then used to identify parameters for the characteristic relationships described subsequently. Considering only linear mixed terms, a regression model with two independent variables $r(x_1, x_2)$ may take the form

$$r(x_1, x_2) = a_{00} + a_{10}x_1 + a_{12}x_1x_2 + a_{20}x_2\,,$$

where a_i are the model parameters to be determined by employing stepwise linear regression.

This method ensures that terms are added to the model only if their parameters are different from zero with a predetermined level of significance. In particular, based on an initial model, an F-test is performed on each parameter not currently included in the model and the parameter with the lowest p-value is added to the model. This step is repeated until there is no parameter left that satisfies $p < 0.05$. Subsequently, an F-test is performed on each parameter included in the model, with the parameter with the largest $p > 0.1$ being eliminated. If there is no parameter satisfying the elimination criterion, the process terminates. Otherwise, the previous step is executed again. In both the *forward selection* and the *backward elimination*, the null hypotheses reads

$$\begin{aligned} H_0: &\quad a_i = 0\,,\\ H_\mathrm{a}: &\quad a_i \neq 0\,. \end{aligned}$$

The procedure is available in MATLAB via `stepwiselm()` [41].

[41] The MathWorks, *stepwiselm.*

Chemical Reaction Progress

In order to describe the reaction system, a total of five equations, which have been identified in the literature [10] to govern the biomass gasification process, are selected. These are the water gas (WG) reaction, the water gas shift (WGS) reaction, the methanation (MET) reaction, the steam methane

[10] Franco et al., “The study of reactions influencing the biomass steam gasification process.” (2003).

reforming (SMR) reaction and the Boudouard equilibrium (BOU) reaction.

Even though the SMR reaction has been found to be severely kinetically inhibited under prevalent operating conditions [23] it appears reasonable to model the CH_4 concentration in relation to the other main product gas components.

$$C_{(s)} + H_2O \rightleftharpoons CO + H_2 \qquad \text{water-gas} \tag{4.2a}$$

$$CO + H_2O \rightleftharpoons CO_2 + H_2 \qquad \text{water-gas shift} \tag{4.2b}$$

$$C_{(s)} + 2\,H_2 \rightleftharpoons CH_4 \qquad \text{methanation} \tag{4.2c}$$

$$CH_4 + H_2O \rightleftharpoons CO + 3\,H_2 \qquad \text{steam-reforming} \tag{4.2d}$$

$$CO_2 + C_{(s)} \rightleftharpoons 2\,CO \qquad \text{Boudouard} \tag{4.2e}$$

Note that solid carbon does not enter the equation for K_{BOU}. Assuming the char phase as solid carbon, its mole fraction $\xi_{C_{(s)}} = 1$.

In equilibrium, each of the reactions will have progressed only to a certain extent, with some amount of reactants remaining in the system. Assuming isobaric conditions, the reaction progress is determined by the system temperature T alone. The *equilibrium constant* $K(T)$ for each reaction follows from thermodynamics and may be written as follows:

$$\begin{gathered} K_{WG}(T) = \frac{\xi_{CO}\,\xi_{H_2}}{\xi_{H_2O}}, \quad K_{WGS}(T) = \frac{\xi_{CO_2}\,\xi_{H_2}}{\xi_{CO}\,\xi_{H_2O}}, \quad K_{MET}(T) = \frac{\xi_{CH_4}}{\xi_{H_2}^2}, \\ K_{SMR}(T) = \frac{\xi_{CO}\,\xi_{H_2}^3}{\xi_{CH_4}\,\xi_{H_2O}}, \quad K_{BOU}(T) = \frac{\xi_{CO}^2}{\xi_{CO_2}}. \end{gathered} \tag{4.3}$$

While the equilibrium constants assume fixed values for any given temperature, they do not take the kinetics of the underlying reactions into account. It has been observed that the reaction system does in fact not reach chemical equilibrium. This is at least true for the SMR reaction—while an amount of $\xi_{CH_4} \approx 10\,\%$ is commonly observed in the product gas, equilibrium calculations predict virtually no CH_4 for $T > 750\,°C$ [36].

[36] Schuster et al., “Biomass steam gasification – an extensive parametric modeling study.” (2001).

However, the expressions on the right-hand side, i.e., the *law of mass action*, may be computed for any non-equilibrium state as well—naturally yielding deviating values. In general, the main factors influencing the reaction kinetics are reactor temperature, residence time, and mixing behavior, i.e. mass transfer, and catalytic activity. These can be assumed to directly depend on plant layout and operating parameters for the given DFB plant. Since the former is not subject to frequent changes, it appears reasonable to model these expressions in dependence of the plant input parameters.

Motivated by this reasoning, for each of the reactions eqn. (4.2) the law of mass action, i.e., the expression

$$\prod_j \xi_j^{\nu_{ij}},$$

where ν_{ij} denotes the stoichiometric coefficient of species j in reaction i, is evaluated. Corresponding linear models $r_i(\boldsymbol{u})$ are then identified to predict the reaction progress in terms of the system inputs.

By convention, the stoichiometric coefficient is positive for products and negative for reactants.

C_2 Components

As previously discussed, C_2H_6 and C_2H_4 are also present in the product gas. The concentrations of these species are modeled using a different approach for two reasons. Firstly, fewer data are available for these components. Consequently, identifying a model with fewer parameters increases the confidence in these parameters benefitting the reliability of its predictions. Secondly, the C_2 components undergo reactions analogous to the SMR reaction.

$$C_xH_y + x\,H_2O \rightleftharpoons x\,CO + \left(y/2 + x\right)H_2\,. \tag{4.4}$$

Thus, it seems reasonable to model the C_2-components in relation to the CH_4-concentration in the product gas:

$$r_i\left(\xi_{CH_4}\right) = a_0 + a_1\xi_{CH_4}\,, \quad \text{where} \quad i = \{C_2H_6, C_2H_4\}\,. \tag{4.5}$$

Char Production Rate

As mentioned before, a key unknown is the char flow rate $\dot{m}_{\text{char}}$. Given the reasonable assumption that the absolute value of the char flow rate is proportional to the fuel flow rate, a linear model $r_{\text{char}}(\boldsymbol{u})$ for the ratio

$$\frac{\dot{m}_{\text{char}}}{\dot{m}_{\text{fuel}}} \tag{4.6}$$

is fitted to the identification data.

Product Gas Analyzer N_2 Correction

The N_2 concentration in the product gas is only available through the GC analysis. However, it can be inferred from the analyzer data through eqn. (3.3). The resulting concentration $\xi_{N_2}^{\text{wf}}$ does, however, exceed the values reported by the GC, since trace gases are not considered in the calculation. Therefore, another linear model is identified to correct the calculated value:

$$r_{N_2}\left(\xi_{N_2}^{\text{wf,analyzer}}\right) = a_0 + a_1\xi_{N_2}^{\text{wf,analyzer}}\,. \tag{4.7}$$

This model is intended to serve as a fallback, in the event of the GC measurement being unavailable.

Loop Seal Split Ratio

Finally, the steam flow rate from the upper and lower loop seals (see Figure 2.1) into the gasification reactor and the combustion reactor, respectively, is unknown, as only the total steam flow rate to each of the loop seals is accessible by measurement. While an even split might be assumed, this assumption did not yield satisfactory results with regard to the material balances for each reactor. However, the split ratio cannot be directly recovered from the material balances of the two reactors because the measured total loop seal steam flow rate, $\dot{m}_{\mathrm{st}}^{\mathrm{LS}}$, may be insufficient to resolve both material balances.

Therefore, an attempt is made to correct the split ratio χ_{LS} starting from an initially assumed value of

$$\chi_{\mathrm{LS}} = \dot{m}_{\mathrm{st}}^{\mathrm{GR,LS}} / \dot{m}_{\mathrm{st}}^{\mathrm{LS}} = 0.5\,,$$

The product gas water content $\tilde{\xi}_{\mathrm{H_2O}}^{\mathrm{PG}}$ is determined by solving eqn. (3.4). Considering all steady-state points for which offline water content measurements have been conducted, the relative error $\varepsilon_{\mathrm{H_2O}}$ in the product gas water content was computed as follows:

$$\varepsilon_{\mathrm{H_2O}} = \frac{\tilde{\xi}_{\mathrm{H_2O}}^{\mathrm{PG}}}{\tilde{\xi}_{\mathrm{H_2O}}^{\mathrm{PG,offline}}} - 1\,. \tag{4.8}$$

The expression

$$\frac{\varepsilon_{\mathrm{H_2O}}}{\varepsilon_{\mathrm{H_2O}}^{-}}\,,$$

where $\varepsilon_{\mathrm{H_2O}}^{-}$ is the minimum observed error as per eqn. (4.8) out of all sample points, is evaluated. Its value is subsequently fitted by a linear model

$$r_{\mathrm{H_2O}}(\Delta p_{\mathrm{GR-CR}}) \in [0, 1]\,. \tag{4.9}$$

The steam flow rate entering the gasification reactor via the upper and lower loop seals is then predicted as follows:

$$\dot{m}_{\mathrm{st}}^{\mathrm{GR,LS}} = \underbrace{\left(\chi_{\mathrm{LS}}^{0} + r_{\mathrm{H_2O}}\left(1 - \chi_{\mathrm{LS}}^{0}\right)\right)}_{\chi_{\mathrm{LS}}(\Delta p_{\mathrm{GR-CR}})} \dot{m}_{\mathrm{st}}^{\mathrm{LS}}\,. \tag{4.10}$$

This approach yields better results concerning the closure of the material balance of the gasification reactor, in comparison to the assumption of a constant split ratio for all data sets. Still, it can only be regarded as a *best-guess* estimate as discussed in the following section.

4.2.2 Combined Static Reactor Model

Utilizing the linear regression models identified earlier, a combined static nonlinear model is created in form of an implicit function $\mathbf{F}(\boldsymbol{u}, \bar{\boldsymbol{x}}) = \mathbf{0}$ with the current input vector $\boldsymbol{u}$ and the static model prediction $\bar{\boldsymbol{x}}$ of the system state. The individual entries of $\mathbf{F}$ are computed as follows:

$$F_1(\boldsymbol{u}, \bar{\boldsymbol{x}}) = \frac{\dot{n}_{\mathrm{char}}}{\dot{m}_{\mathrm{fuel}}/M^{\mathrm{waf}}_{\mathrm{char}} r_{\mathrm{char}}(\boldsymbol{u})} - 1 = 0\,, \tag{4.11a}$$

$$F_2(\boldsymbol{u}, \bar{\boldsymbol{x}}) = \frac{\dot{n}_{\mathrm{tar}}}{\dot{n}^{\mathrm{wf}}_{\mathrm{PG}}/M^{\mathrm{waf}}_{\mathrm{tar}} r_{\mathrm{tar}}(\tilde{\xi}^{\mathrm{wf}}_{\mathrm{CH_4}})} - 1 = 0\,, \tag{4.11b}$$

$$F_3(\boldsymbol{u}, \bar{\boldsymbol{x}}) = \frac{\tilde{\xi}_{\mathrm{H_2}} \tilde{\xi}_{\mathrm{CO}} / \tilde{\xi}_{\mathrm{H_2O}}}{r_{\mathrm{WG}}(\boldsymbol{u})} - 1 = 0\,, \tag{4.11c}$$

$$F_4(\boldsymbol{u}, \bar{\boldsymbol{x}}) = \frac{\tilde{\xi}_{\mathrm{H_2}} \tilde{\xi}_{\mathrm{CO_2}} / \tilde{\xi}_{\mathrm{CO}} \tilde{\xi}_{\mathrm{H_2O}}}{r_{\mathrm{WGS}}(\boldsymbol{u})} - 1 = 0\,, \tag{4.11d}$$

$$F_5(\boldsymbol{u}, \bar{\boldsymbol{x}}) = \frac{\tilde{\xi}_{\mathrm{CH_4}} / \tilde{\xi}^2_{\mathrm{H_2}}}{r_{\mathrm{MET}}(\boldsymbol{u})} - 1 = 0\,, \tag{4.11e}$$

$$F_6(\boldsymbol{u}, \bar{\boldsymbol{x}}) = \frac{\tilde{\xi}^3_{\mathrm{H_2}} \tilde{\xi}_{\mathrm{CO}} / \tilde{\xi}_{\mathrm{CH_4}} \tilde{\xi}_{\mathrm{H_2O}}}{r_{\mathrm{SMR}}(\boldsymbol{u})} - 1 = 0\,, \tag{4.11f}$$

$$F_7(\boldsymbol{u}, \bar{\boldsymbol{x}}) = \frac{\tilde{\xi}^2_{\mathrm{CO}} / \tilde{\xi}_{\mathrm{CO_2}}}{r_{\mathrm{BOU}}(\boldsymbol{u})} - 1 = 0\,, \tag{4.11g}$$

$$\begin{aligned} F_8(\boldsymbol{u}, \bar{\boldsymbol{x}}) &= \tilde{\xi}_{\mathrm{O_2}} / C_{\mathrm{O_2}} - 1 = 0\,, \\ &\text{where} \quad C_{\mathrm{O_2}} = 10^{-4}\,, \end{aligned} \tag{4.11h}$$

$$F_9(\boldsymbol{u}, \bar{\boldsymbol{x}}) = \frac{\tilde{\xi}_{\mathrm{C_2H_6}}}{r_{\mathrm{C_2H_6}}(\tilde{\xi}^{\mathrm{wf}}_{\mathrm{CH_4}})(1 - \tilde{\xi}_{\mathrm{H_2O}})} - 1 = 0\,, \tag{4.11i}$$

$$F_{10}(\boldsymbol{u}, \bar{\boldsymbol{x}}) = \frac{\tilde{\xi}_{\mathrm{C_2H_4}}}{r_{\mathrm{C_2H_4}}(\tilde{\xi}^{\mathrm{wf}}_{\mathrm{CH_4}})(1 - \tilde{\xi}_{\mathrm{H_2O}})} - 1 = 0\,, \tag{4.11j}$$

$$\mathbf{F}_{11\ldots14}(\boldsymbol{u}, \bar{\boldsymbol{x}}) = \Delta \dot{\boldsymbol{n}}^{\mathrm{GR}} \oslash \dot{\boldsymbol{n}}^{\mathrm{GR}}_{\mathrm{in}} = 0\,, \tag{4.11k}$$

$$\mathbf{F}_{15\ldots18}(\boldsymbol{u}, \bar{\boldsymbol{x}}) = \Delta \dot{\boldsymbol{n}}^{\mathrm{CR}} \oslash \dot{\boldsymbol{n}}^{\mathrm{CR}}_{\mathrm{in}} = 0\,, \tag{4.11l}$$

$$\mathbf{F}_{19}(\boldsymbol{u}, \bar{\boldsymbol{x}}) = \frac{\dot{m}^{\mathrm{GR,LS}}_{\mathrm{st}}}{\left(\chi^0_{\mathrm{LS}} + r_{\mathrm{H_2O}} \left(1 - \chi^0_{\mathrm{LS}}\right)\right) \dot{m}^{\mathrm{LS}}_{\mathrm{st}}} - 1 = 0\,. \tag{4.11m}$$

$\dot{\boldsymbol{n}}$ denotes the element molar flow rates as opposed to the species molar flow rates:

$$\dot{\boldsymbol{n}} = \left[\dot{n}_{\mathrm{C}} \quad \dot{n}_{\mathrm{H}} \quad \dot{n}_{\mathrm{O}} \quad \dot{n}_{\mathrm{N}}\right]^{\top}.$$

All entries in eqn. (4.11) are expressed as fractions. This form was chosen for scaling purposes. Note that the mole fractions $\tilde{\xi}_i$ are computed according to

$$\tilde{\xi}_i = \frac{\dot{n}_i}{\sum_j \dot{n}_j} \tag{4.12}$$

from the system state vector, prior to evaluating $\mathbf{F}(\boldsymbol{u}, \boldsymbol{x})$.

Eqn. (4.11a) sets the state prediction of the char flow rate $\dot{n}_{\mathrm{char}}$ in relation to the value predicted by the linear regression model $r_{\mathrm{char}}(\boldsymbol{u})$. Since the model predicts the char-to-fuel mass ratio, the factor $\dot{m}_{\mathrm{fuel}}/M^{\mathrm{waf}}_{\mathrm{char}}$, with the molar mass of water-and-ash-free char $M^{\mathrm{waf}}_{\mathrm{char}}$, is needed as well. The expression evaluates to zero if the system state prediction equals the linear model prediction.

The identification of the tar model was not conducted as part of this work. Instead, it was adopted from an IPSEpro model of the DFB plant, which is based on [4]. The IPSEpro model is described in some detail in [21].

Similarly, eqn. (4.11b) sets the system state prediction in relation to the linear model prediction $r_{\mathrm{tar}}(\boldsymbol{u})$. Again, a conversion factor $\dot{n}^{\mathrm{wf}}_{\mathrm{PG}}/M^{\mathrm{waf}}_{\mathrm{tar}}$ is needed, where $\dot{n}^{\mathrm{wf}}_{\mathrm{PG}}$ is the total dry product gas mole flow and $M^{\mathrm{waf}}_{\mathrm{tar}}$ is the molar mass of water-and-ash-free tar.

Eqns. (4.11c) to (4.11g) are all defined with the law of mass action for reactions eqn. (4.2) in the numerator and the corresponding linear model in the denominator. Each expression equals zero when the law of mass action takes the value predicted by the corresponding linear model.

The model for the O_2 concentration, eqn. (4.11h), is the simplest, as it assumes a constant value.

Since the linear models for the C_2 components reflect dry compositions, the conversion factor $(1 - \tilde{\xi}_{H_2O})$ is required in eqns. (4.11i) and (4.11j).

Eqns. (4.11k) and (4.11l) represent the relative molar element balance for the gasification reactor and combustion reactor, respectively. This ensures the conservation of mass in the prediction step—at least in a least-squares sense.

Finally, $\mathbf{F}_{19}$ sets the steam mass flow rate entering the gasification reactor via the upper and lower loop seals, $\dot{m}^{\mathrm{GR,LS}}_{\mathrm{st}}$, to the value predicted by the model eqn. (4.10).

Eqn. (4.11) is a system of 19 nonlinear equations for $n_{\mathrm{x}} = 16$ system states. In particular, eqn. (4.11) is reformulated as a constrained optimization problem

$$\begin{aligned} &\min_{\bar{x}} \|\mathbf{F}(\boldsymbol{u}, \bar{\boldsymbol{x}})\|_2^2 \,, \\ \text{subject to} \quad &\bar{x}_i \geq 0, \quad i = 1, 2, \ldots, n_{\mathrm{x}} \,. \end{aligned} \tag{4.13}$$

Clearly, the solution is subject to constraints since a negative sign implies an incoming as opposed to an outgoing flow. Problem eqn. (4.13) is solved iteratively at each time step using the least-squares solver implementation `lsqnonlin()`, which is a least-squares solver available in MATLAB.

4.2.3 Alternative Static Reactor Model

During gasification tests, the fuel feed may be interrupted, i.e., $\dot{m}_{\mathrm{fuel}} = 0\,\mathrm{kg/h}$. In this case, the static model eqn. (4.11) is no longer valid since it is largely based on regression models identified for a limited range of set points, rather than on first principles only. Consequently, an alternative model, $\tilde{\mathbf{F}}$, is used in this case. The alternative model simply sets the molar flow rates of all species except N_2 and H_2O exiting the gasification reactor to $\dot{n}_i = 0\,\mathrm{kmol/h}$. The gasification reactor and combustion reactor material balances remain unaltered, as well as the equation corresponding to $\dot{m}_{\mathrm{st}}^{\mathrm{GR,LS}}$. Mathematically, the model is formulated as follows:

$$\begin{aligned}
\tilde{F}_i(\boldsymbol{u},\bar{\boldsymbol{x}}) &= \frac{\dot{n}_i}{10^{-10}\,\mathrm{kmol/h}} - 1 = 0\,. \\
\forall i &\in \mathscr{I} = \{\mathrm{H_2}, \mathrm{CO}, \mathrm{CO_2}, \mathrm{CH_4}, \mathrm{C_2H_6}, \ldots \\
&\qquad \mathrm{C_2H_4}, \mathrm{O_2}, \mathrm{char}, \mathrm{tar}\}\,, \quad |\mathscr{I}| = 9\,,
\end{aligned} \tag{4.14a}$$

$$\tilde{\mathbf{F}}_{10\ldots13}(\boldsymbol{u},\bar{\boldsymbol{x}}) = \Delta\dot{\boldsymbol{n}}^{\mathrm{GR}} \oslash \dot{\boldsymbol{n}}_{\mathrm{in}}^{\mathrm{GR}} = 0\,, \tag{4.14b}$$

$$\tilde{\mathbf{F}}_{14\ldots17}(\boldsymbol{u},\bar{\boldsymbol{x}}) = \Delta\dot{\boldsymbol{n}}^{\mathrm{CR}} \oslash \dot{\boldsymbol{n}}_{\mathrm{in}}^{\mathrm{CR}} = 0\,, \tag{4.14c}$$

$$\tilde{\mathbf{F}}_{18}(\boldsymbol{u},\bar{\boldsymbol{x}}) = \frac{\dot{m}_{\mathrm{st}}^{\mathrm{GR,LS}}}{\left(\chi_{\mathrm{LS}}^{0} + r_{\mathrm{H_2O}}\left(1-\chi_{\mathrm{LS}}^{0}\right)\right)\dot{m}_{\mathrm{st}}^{\mathrm{LS}}} - 1 = 0\,. \tag{4.14d}$$

This means the number of equations in the model is reduced by one, but it still exceeds the number of variables.

4.2.4 Disturbance States

To improve the prediction accuracy of the Hammerstein model, described in earlier, based on previous measurements $n_{\mathrm{d}} = 8$ disturbance states d_i were defined:

$$\boldsymbol{d} = \begin{bmatrix} d_{\mathrm{CO}} & d_{\mathrm{CO_2}} & d_{\mathrm{CH_4}} & d_{\mathrm{C_2H_6}} d_{\mathrm{C_2H_4}} & d_{\mathrm{O_2}} & d_{\mathrm{char}} & d_{\mathrm{N_2}} \end{bmatrix}^{\top}. \tag{4.15}$$

The first six disturbance states correct the molar flow rates of the associated product gas species according to

$$\begin{aligned}
\dot{n}_i &\rightarrow \frac{\dot{n}_i}{d_i}\,, \quad \text{where} \\
i &\in \mathscr{I} = \{\mathrm{CO}, \mathrm{CO_2}, \mathrm{CH_4}, \mathrm{C_2H_6}, \mathrm{C_2H_4}, \mathrm{O_2}\}\,,
\end{aligned} \tag{4.16}$$

which is done before evaluating eqn. (4.11).

Similarly, the char flow rate predicted by the regression model eqn. (4.6) is corrected through a disturbance state as well:

$$r_{\mathrm{char}} \rightarrow \frac{r_{\mathrm{char}}}{d_{\mathrm{char}}}\,. \tag{4.17}$$

In contrast, $d_{\mathrm{N_2}}$ represents the unknown molar flow rate of N_2 introduced into the system due to flushing temperature and pressure probes (see Section 2.1).

As a consequence, the optimization problem eqn. (4.13) becomes

$$\begin{aligned}
&\min_{\bar{x}} \left\|\mathbf{F}(\boldsymbol{u},\bar{\boldsymbol{x}},\hat{\boldsymbol{d}})\right\|_2^2, \\
&\text{subject to} \quad \bar{x}_i \geq 0, \quad i = 1, 2, \ldots, n_{\mathrm{x}}\,.
\end{aligned} \tag{4.18}$$

where $\hat{\boldsymbol{d}}$ denotes the estimate of the disturbances. It is obtained through the use of a dedicated EKF, which will be described in Section 5.3.

4.3 System Dynamics

Based on historical data, the molar flow rates of the product gas components appear to express exponential decay following a fuel feed rate interruption. Consequently, a simple first-order dynamic ansatz is made:

In the observer design, a discretized version of this ansatz is employed, which will be detailed in Section 5.2.

$$\dot{x}_i = -\frac{1}{\tau_i}\left(x_i - f_i\left(\boldsymbol{u}, \hat{\boldsymbol{d}}\right)\right), \quad i = 1, 2, \ldots, n_\mathrm{x}, \tag{4.19}$$

Refer to Appendix C for an overview of the soft sensor parameters.

where τ_i is the time constant associated with each state. The particular value is considered a tuning parameter to be determined. The function $f_i\left(\boldsymbol{u}, \hat{\boldsymbol{d}}\right)$ denotes the static model prediction of the i^{th} system state, which is mathematically given by

$$\mathbf{f}\left(\boldsymbol{u}, \hat{\boldsymbol{d}}\right) = \underset{\bar{x}}{\operatorname{argmin}} \left\| \mathrm{F}(\boldsymbol{u}, \bar{\boldsymbol{x}}, \hat{\boldsymbol{d}}) \right\|_2^2 \tag{4.20a}$$

$$\text{subject to} \quad \bar{x}_i \geq 0, \quad i = 1, 2, \ldots, n_\mathrm{x}. \tag{4.20b}$$

The obvious advantage of this ansatz is its simplicity, however, the drawback is that time constants are only associated with each state. This makes it impossible to fit different time constants for different inputs, such as the fuel feed rate or the steam flow rate.

In contrast to the system states, the disturbances are assumed to remain constant over time.

$$\dot{d}_i = 0, \quad i = 1, 2, \ldots, n_\mathrm{d}, \tag{4.21}$$

This concludes the layout of the Hammerstein model as depicted in Figure 4.1.

5 Observer Design

The Hammerstein model developed in Chapter 4 provides the system state prediction for an EKF-type observer forming the core of the soft sensor. The following chapter commences by describing the general structure of the soft sensor, followed by a dedicated section for each of its components. These include a Kalman filter for estimating the system state, EKF_x, and another Kalman filter for estimating the disturbance state, EKF_d, described in Section 5.2 and Section 5.3, respectively. The delayed GC measurements necessitate special treatment to fuse them using the optimal gain, which will be detailed in Section 5.4. Additionally, the mechanism used to detect faults in any of the measurements will be described in Section 5.5. For further information, a description of the code structure of the soft sensor is included in Appendix A, as well as a brief description of the online monitoring interface developed within the scope of this work.

5.1 General Structure

The central element of the soft sensor is formed by an EKF to estimate the system state $\boldsymbol{x}$. It will be referred to by EKF_x and will be described in detail in Section 5.2. It uses the measurements $\boldsymbol{z}^\mathrm{ana}$ from the two analyzers and $\boldsymbol{z}^\mathrm{GC}$ from the GC to correct the system state predictions generated by the Hammerstein model. It assumes the following non-linear, time-invariant, discrete model for the system.

The subscript x alludes to the system state $\boldsymbol{x}$.

The individual entries of the measurement vectors $\boldsymbol{z}_k^\mathrm{ana}$ and $\boldsymbol{z}_k^\mathrm{GC}$ are given by

$$\boldsymbol{z}^\mathrm{ana} = \begin{bmatrix} z_{\mathrm{H_2}}^\mathrm{PG,ana} \\ z_{\mathrm{CO}}^\mathrm{PG,ana} \\ z_{\mathrm{CO_2}}^\mathrm{PG,ana} \\ z_{\mathrm{CH_4}}^\mathrm{PG,ana} \\ z_{\mathrm{O_2}}^\mathrm{PG,ana} \\ z_{\mathrm{N_2}}^\mathrm{PG,ana} \\ z_{\mathrm{O_2}}^\mathrm{FG,ana} \\ z_{\mathrm{CO_2}}^\mathrm{FG,ana} \\ z_{\mathrm{N_2}}^\mathrm{FG,ana} \end{bmatrix}, \boldsymbol{z}^\mathrm{GC} = \begin{bmatrix} z_{\mathrm{CO}}^\mathrm{GC} \\ z_{\mathrm{CO_2}}^\mathrm{GC} \\ z_{\mathrm{CH_4}}^\mathrm{GC} \\ z_{\mathrm{C_2H_6}}^\mathrm{GC} \\ z_{\mathrm{C_2H_4}}^\mathrm{GC} \\ z_{\mathrm{O_2}}^\mathrm{GC} \\ z_{\mathrm{N_2}}^\mathrm{GC} \end{bmatrix}.$$

$$\boldsymbol{x}_{k+1} = \boldsymbol{\Phi}_\mathrm{x}\boldsymbol{x}_k + \boldsymbol{\Gamma}_\mathrm{x}\mathbf{f}(\boldsymbol{u}_k) + \boldsymbol{w}_{\mathrm{x},k} \tag{5.1a}$$

$$\boldsymbol{z}_k^\mathrm{ana} = \mathbf{h}_\mathrm{x}^\mathrm{ana}(\boldsymbol{x}_k) + \boldsymbol{v}_k^\mathrm{ana}, \tag{5.1b}$$

$$\boldsymbol{z}_k^\mathrm{GC} = \mathbf{h}_\mathrm{x}^\mathrm{GC}(\boldsymbol{x}_s) + \boldsymbol{v}_s^\mathrm{GC} \tag{5.1c}$$

where $\boldsymbol{\Phi}_\mathrm{x}$ and $\boldsymbol{\Gamma}_\mathrm{x}$ denote the *state transition matrix* and the *control input matrix*. $\boldsymbol{w}_\mathrm{x} \sim \mathcal{N}(\mathbf{0}, \boldsymbol{Q}_\mathrm{x})$ and $\boldsymbol{v} \sim \mathcal{N}(\mathbf{0}, \boldsymbol{R})$ denote the process noise and the measurement noise; both are assumed to be normally distributed with zero mean and covariance matrices $\boldsymbol{Q}_\mathrm{x}$ and $\boldsymbol{R}$, respectively. The output function is referred to by $\mathbf{h}_x(\boldsymbol{x})$ and is non-linear; its individual entries will be described in Section 5.2. $\boldsymbol{z}_k^\mathrm{GC}$ in eqn. (5.2c) is

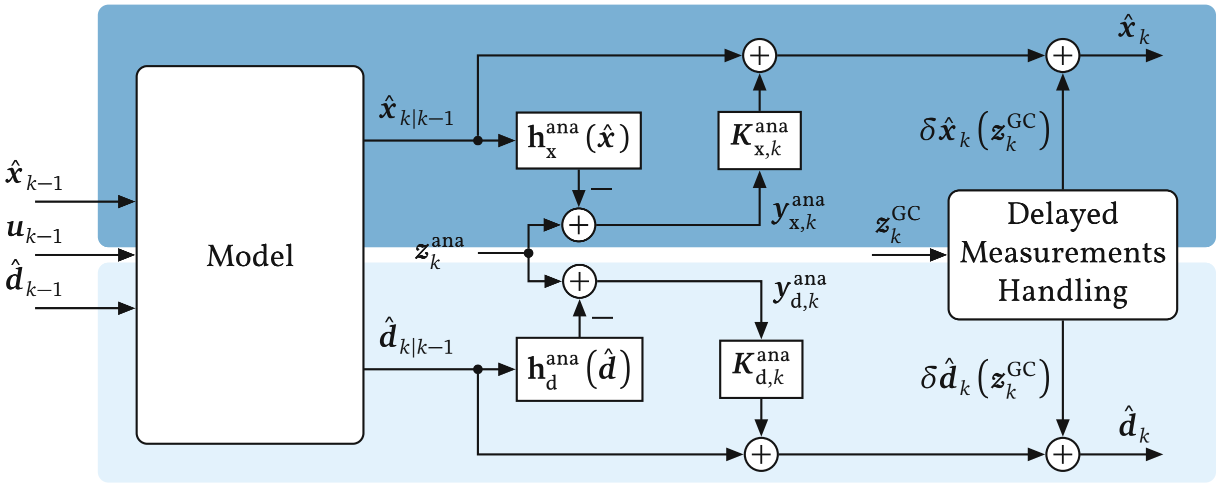

Figure 5.1: Block diagram of the soft sensor comprising the EKF$_{\mathrm{x}}$ for estimating the system state, indicated by 🟦, and the EKF$_{\mathrm{d}}$ for estimating the disturbances, indicated by ⬜. The delayed GC measurements are handled in a special way, as indicated.

the GC measurement taken at time $s = k - T_s^{\mathrm{GC}}/T_s$, where $T_s^{\mathrm{GC}} = 12\,\mathrm{min}$ is the sampling time of the GC. The optimal gain to fuse the delayed measurement at time k will be described in Section 5.4.

Figure 5.1 also displays the second EKF$_{\mathrm{d}}$. It facilitates the correction of the static reactor model employing the disturbance state $\boldsymbol{d}$, thereby improving future predictions based on past measurements. The temporal development of the disturbances is assumed to be driven solely by white noise. Consequently, the disturbance model reads as follows:

$$\begin{aligned} \boldsymbol{d}_{k+1} &= \boldsymbol{\Phi}_{\mathrm{d}}\boldsymbol{d}_k + \boldsymbol{w}_{\mathrm{d},k}, \quad \text{where} \quad \boldsymbol{\Phi}_{\mathrm{d}} = \mathbf{I} & (5.2\mathrm{a}) \\ \boldsymbol{z}_k^{\mathrm{ana}} &= \mathbf{h}_{\mathrm{d}}(\boldsymbol{d}_k) + \boldsymbol{v}_k^{\mathrm{ana}}, & (5.2\mathrm{b}) \\ \boldsymbol{z}_k^{\mathrm{GC}} &= \mathbf{h}_{\mathrm{d}}^{\mathrm{GC}}(\boldsymbol{d}_s) + \boldsymbol{v}_s^{\mathrm{GC}} & (5.2\mathrm{c}) \end{aligned}$$

where, again, the process noise $\boldsymbol{w}_{\mathrm{d}} \sim \mathcal{N}(\mathbf{0}, \boldsymbol{Q}_{\mathrm{d}})$ and the measurement noise $\boldsymbol{v}_{\mathrm{d}} \sim \mathcal{N}(\mathbf{0}, \boldsymbol{R})$ are assumed to be zero-mean Gaussian distributed with covariance matrices $\boldsymbol{Q}_{\mathrm{d}}$ and $\boldsymbol{R}$, respectively. Again, in eqn. (5.2c), $\boldsymbol{z}_k^{\mathrm{GC}}$ is the delayed measurement.

A common event during the operation of the DFB gasification plant is the gas analysis equipment reporting erroneous values. This is solved by a fault detection mechanism described in Section 5.5 based on the EKF$_{\mathrm{x}}$'s innovation sequence.

5.2 Extended Kalman Filter for System State Estimation

In this section, the equations of the $\mathrm{EKF}_{\mathrm{x}}$ will be described. The *a priori* estimate generated using the Hammerstein model is given by

$$\hat{\boldsymbol{x}}_{k|k-1} = \boldsymbol{\Phi}_{\mathrm{x}}\,\hat{\boldsymbol{x}}_{k-1} + \boldsymbol{\Gamma}_{\mathrm{x}}\,\mathbf{f}(\boldsymbol{u}_{k-1})\,, \tag{5.3a}$$

$$\boldsymbol{P}_{\mathrm{x},k|k-1} = \boldsymbol{\Phi}_{\mathrm{x}}\,\boldsymbol{P}_{\mathrm{x},k-1}\,\boldsymbol{\Phi}_{\mathrm{x}}^{\top} + \boldsymbol{Q}_{\mathrm{x}}\,, \tag{5.3b}$$

where $\hat{\boldsymbol{x}}_{k|k-1}$ is the a priori estimate of the current time step, $\hat{\boldsymbol{x}}_{k-1}$ is the *a posteriori* estimate of the previous time step and $\mathbf{f}(\boldsymbol{u}_{k-1})$ is the Hammerstein model prediction of the static system state, as described in Section 4.3. $\boldsymbol{P}_{\mathrm{x}}$ denotes the estimation error covariance matrix. The process noise covariance matrix $\boldsymbol{Q}_{\mathrm{x}}$ is unknown and is considered a tuning parameter.

The matrices $\boldsymbol{\Phi}_{\mathrm{x}}$ and $\boldsymbol{\Gamma}_{\mathrm{x}}$ are determined by applying a semi-implicit Euler scheme to the dynamic ansatz eqn. (4.19):

$$\hat{x}_{i,k|k-1} = \frac{2\tau_i - T_s}{2\tau_i + T_s}\,\hat{x}_{i,k-1} + \frac{2T_s}{2\tau_i + T_s}\,f_i(\boldsymbol{u}_{k-1})\,, \tag{5.4}$$

where $T_s = 5\,\mathrm{s}$ is the sampling time the soft sensor operates at. Consequently, $\boldsymbol{\Phi}_{\mathrm{x}}$ and $\boldsymbol{\Gamma}_{\mathrm{x}}$ evaluate as the following diagonal matrices:

At this point $\tau_i = \tau = 6T_s = 30\,\mathrm{s}$ is assumed. This assumption will be tested in Section 6.5.

$$\begin{aligned} \boldsymbol{\Phi} &= \operatorname{diag}\left(\frac{2\tau_1 - T_s}{2\tau_1 + T_s}, \dots, \frac{2\tau_{n_{\mathrm{x}}} - T_s}{2\tau_{n_{\mathrm{x}}} + T_s}\right) \quad \text{and} \\ \boldsymbol{\Gamma} &= \operatorname{diag}\left(\frac{2T_s}{2\tau_1 + T_s}, \dots, \frac{2T_s}{2\tau_{n_{\mathrm{x}}} + T_s}\right), \end{aligned} \tag{5.5}$$

The a posteriori estimate $\hat{\boldsymbol{x}}_k$ is obtained as follows:

$$\hat{\boldsymbol{x}}_k = \hat{\boldsymbol{x}}_{k|k-1} + \boldsymbol{K}_{\mathrm{x},k}^{\mathrm{ana}}\,\boldsymbol{y}_{\mathrm{x},k}^{\mathrm{ana}} + \delta\hat{\boldsymbol{x}}_k\,, \tag{5.6a}$$

$$\boldsymbol{P}_{\mathrm{x},k} = \left(\mathbf{I} - \boldsymbol{K}_{\mathrm{x},k}^{\mathrm{ana}}\,\boldsymbol{H}_{\mathrm{x},k}^{\mathrm{ana}}\right)\boldsymbol{P}_{\mathrm{x},k|k-1} + \delta\boldsymbol{P}_{\mathrm{x},k}\,, \tag{5.6b}$$

where the system state is corrected by the product of the Kalman gain $\boldsymbol{K}_{\mathrm{x},k}^{\mathrm{ana}}$ and the innovation $\boldsymbol{y}_{\mathrm{x},k}^{\mathrm{ana}}$. The correction terms $\delta\hat{\boldsymbol{x}}_k$ and $\delta\boldsymbol{P}_{\mathrm{x},k}$ are non-zero only at the time a GC measurement becomes available, which will be discussed in Section 5.4. The measurement sensitivity matrix $\boldsymbol{H}_{\mathrm{x},k}^{\mathrm{ana}}$ is defined as the partial derivative of the output equation $\mathbf{h}_{\mathrm{x}}^{\mathrm{ana}}$ with respect to the system state $\boldsymbol{x}$ evaluated at the a priori estimate:

$$\boldsymbol{H}_{\mathrm{x},k}^{\mathrm{ana}} = \left.\frac{\partial \mathbf{h}_{\mathrm{x}}^{\mathrm{ana}}}{\partial \boldsymbol{x}}\right|_{\hat{\boldsymbol{x}}_{k|k-1}}. \tag{5.7}$$

With this definition, the Kalman gain is derived:

$$\boldsymbol{K}^{\mathrm{ana}}_{\mathrm{x},k} = \boldsymbol{P}_{\mathrm{x},k|k-1}\,\boldsymbol{H}^{\mathrm{ana}\top}_{\mathrm{x},k}\left(\boldsymbol{H}^{\mathrm{ana}}_{\mathrm{x},k}\,\boldsymbol{P}_{\mathrm{x},k|k-1}\,\boldsymbol{H}^{\mathrm{ana}\top}_{\mathrm{x},k} + \boldsymbol{R}^{\mathrm{ana}}\right)^{-1}, \tag{5.8}$$

where $\top$ indicates the transpose of the matrix. The covariance matrix $\boldsymbol{R}^{\mathrm{ana}}$ of the measurement noise of the analyzers is unknown and considered a tuning parameter.

The innovation $\boldsymbol{y}^{\mathrm{ana}}_{\mathrm{x},k}$ is defined as

$$\boldsymbol{y}^{\mathrm{ana}}_{\mathrm{x},k} = \boldsymbol{z}^{\mathrm{ana}}_{k} - \mathbf{h}^{\mathrm{ana}}_{\mathrm{x}}\left(\hat{\boldsymbol{x}}_{k|k-1}\right), \tag{5.9}$$

where each of the vectors comprises the entries corresponding to the species measured by the product gas and flue gas analyzers.

Since the system state comprises the molar flow rates but the analyzers measure water-free mole fractions, the output function $\mathbf{h}^{\mathrm{ana}}_{\mathrm{x}}$ takes the following form:

$$h^{\mathrm{ana,PG}}_{\mathrm{x},i}(\boldsymbol{x}) = \xi^{\mathrm{PG,wf}}_{i} = \frac{\dot{n}^{\mathrm{PG}}_{i}}{\sum_j \dot{n}^{\mathrm{PG}}_{j}}, \quad \text{where} \\ i,j \in \mathscr{I}^{\mathrm{PG}} = \{\mathrm{H_2}, \mathrm{CO}, \mathrm{CO_2}, \mathrm{CH_4}, \mathrm{C_2H_6}, \mathrm{C_2H_4}, \mathrm{N_2}, \mathrm{O_2}\}, \tag{5.10a}$$

$$h^{\mathrm{ana,FG}}_{\mathrm{x},i}(\boldsymbol{x}) = \xi^{\mathrm{FG,wf}}_{i} = \frac{\dot{n}^{\mathrm{FG}}_{i}}{\sum_j \dot{n}^{\mathrm{FG}}_{j}}, \quad \text{where} \\ i,j \in \mathscr{I}^{\mathrm{FG}} = \{\mathrm{CO_2}, \mathrm{N_2}, \mathrm{O_2}\}, \tag{5.10b}$$

As in the case of the product gas analyzer, the $\mathrm{N_2}$ concentration in the flue gas is also inferred from the available species concentrations from

$$\xi^{\mathrm{FG,wf}}_{\mathrm{N_2}} \approx 1 - \xi^{\mathrm{FG,wf}}_{\mathrm{CO_2}} - \xi^{\mathrm{FG,wf}}_{O2}.$$

where i refers to any of the species in $\mathscr{I}$, whereas j runs over all species, as indicated.

5.3 Extended Kalman Filter for Disturbance State Estimation

As described in Section 5.1, these disturbance states are estimated by the $\mathrm{EKF_d}$. Based on the underlying model eqn. (5.2), the a priori estimate of the disturbance state, considering the disturbance state transition matrix $\boldsymbol{\Phi}_{\mathrm{d}} = \mathbf{I}$, is obtained through

$$\hat{\boldsymbol{d}}_{k|k-1} = \hat{\boldsymbol{d}}_{k-1}, \tag{5.11a}$$

$$\boldsymbol{P}_{\mathrm{d},k|k-1} = \boldsymbol{P}_{\mathrm{d},k-1} + \boldsymbol{Q}_{\mathrm{d}}, \tag{5.11b}$$

where the covariance matrix $\boldsymbol{Q}_{\mathrm{d}}$ is unknown and considered a tuning parameter.

The a posteriori estimate follows from

$$\hat{\boldsymbol{d}}_{k} = \hat{\boldsymbol{d}}_{k|k-1} + \boldsymbol{K}^{\mathrm{ana}}_{\mathrm{d},k}\,\boldsymbol{y}^{\mathrm{ana}}_{\mathrm{d},k} + \delta\hat{\boldsymbol{d}}_{k}, \tag{5.12a}$$

$$\boldsymbol{P}_{\mathrm{d},k} = \left(\mathbf{I} - \boldsymbol{K}^{\mathrm{ana}}_{\mathrm{d},k}\,\boldsymbol{H}^{\mathrm{ana}}_{\mathrm{d},k}\right)\boldsymbol{P}_{\mathrm{d},k|k-1} + \delta\boldsymbol{P}_{\mathrm{d},k}. \tag{5.12b}$$

where, again, the correction terms $\delta\hat{\boldsymbol{d}}_k$ and $\delta\boldsymbol{P}_{\mathrm{d},k}$ are nonzero only at the time a GC measurement becomes available. The measurement sensitivity matrix is computed analogously to eqn. (5.13):

$$\boldsymbol{H}^{\mathrm{ana}}_{\mathrm{d},k} = \left.\frac{\partial \mathbf{h}^{\mathrm{ana}}_{\mathrm{d}}}{\partial \boldsymbol{d}}\right|_{\hat{\boldsymbol{d}}_{k|k-1}}, \tag{5.13}$$

where the output function's partial derivative with respect to the disturbance states is evaluated at the a priori estimate $\hat{\boldsymbol{d}}_{k|k-1}$. The Kalman gain $\boldsymbol{K}^{\mathrm{ana}}_{\mathrm{d},k}$ to update the disturbances based on the analyzer measurements reads

$$\boldsymbol{K}^{\mathrm{ana}}_{\mathrm{d},k} = \boldsymbol{P}_{\mathrm{d},k|k-1}\,\boldsymbol{H}^{\mathrm{ana}^{\top}}_{\mathrm{d},k}\left(\boldsymbol{H}^{\mathrm{ana}}_{\mathrm{d},k}\,\boldsymbol{P}_{\mathrm{d},k|k-1}\,\boldsymbol{H}^{\mathrm{ana}^{\top}}_{\mathrm{d},k} + \boldsymbol{R}^{\mathrm{ana}}\right)^{-1}, \tag{5.14}$$

where the unknown measurement noise $\boldsymbol{R}^{\mathrm{ana}}$ is considered a tuning parameter.

The innovation $\boldsymbol{y}^{\mathrm{ana}}_{\mathrm{d},k}$ is defined as

$$\boldsymbol{y}^{\mathrm{ana}}_{\mathrm{d},k} = \boldsymbol{z}^{\mathrm{ana}}_{k} - \mathbf{h}^{\mathrm{ana}}_{\mathrm{d}}\left(\hat{\boldsymbol{d}}_{k|k-1}\right). \tag{5.15}$$

Due to the way the disturbances act on the system states according to eqn. (4.16), the corresponding individual output functions $h^{\mathrm{ana,PG}}_{\mathrm{d},i}$ take the same form as eqn. (5.10 a):

$$\begin{aligned} h^{\mathrm{ana,PG}}_{\mathrm{d},i}(\boldsymbol{x}) &= \xi^{\mathrm{PG,wf}}_{i} = \frac{\dot{n}^{\mathrm{PG}}_{i}}{\sum_j \dot{n}^{\mathrm{PG}}_{j}}, \quad \text{where} \\ i,j &\in \mathscr{I}^{\mathrm{PG}} = \{\mathrm{CO}, \mathrm{CO_2}, \mathrm{CH_4}, \mathrm{C_2H_6}, \mathrm{C_2H_4}, \mathrm{N_2}, \mathrm{O_2}\}, \end{aligned} \tag{5.16 a}$$

$$\begin{aligned} h^{\mathrm{ana,FG}}_{\mathrm{d},i}(\boldsymbol{x}) &= \xi^{\mathrm{FG,wf}}_{i} = \frac{\dot{n}^{\mathrm{FG}}_{i}}{\sum_j \dot{n}^{\mathrm{FG}}_{j}}, \quad \text{where} \\ i,j &\in \mathscr{I}^{\mathrm{FG}} = \{\mathrm{CO_2}, \mathrm{O_2}\}. \end{aligned} \tag{5.16 b}$$

Given the air and oil flow rates into the combustion reactor, the char flow rate determines the amounts of $\mathrm{CO_2}$ and $\mathrm{O_2}$ in the flue gas, so the corresponding water-free concentrations from the flue gas analyzer are used to correct the disturbance d_{char}, resulting in eqn. (5.16 b).

5.4 Delayed Measurements

As noted earlier, the GC analysis takes approximately 12 min for one sample to complete. Consequently, a GC measurement, $\boldsymbol{z}^{\mathrm{GC}}_{s}$, taken at time s and becoming available at time k will be delayed by $N = k - s$ time steps. The time at which this occurs will be referred to as a *major instance* whereas all other instances will be referred to as a *minor instances*. The

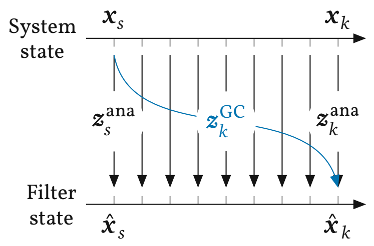

Figure 5.2: System with delayed measurement $\boldsymbol{z}_k^{\text{GC}}$, adapted from [25].

situation is illustrated in Figure 5.2. This means that the GC measurement cannot be fused straightforwardly using eqn. (5.6) since the Kalman gain matrices at both instances are generally different: $\boldsymbol{K}_k^{\text{GC}} \neq \boldsymbol{K}_s^{\text{GC}}$.

Various solutions exist to deal with this problem, the most trivial of which involves recalculating the previous N steps of the filter the moment the delayed measurement becomes available. This approach, however, is deemed unfeasible since the computational burden is concentrated on a single instant, potentially resulting in the computation time exceeding the sampling time T_s.

In this work, the delayed measurement is *extrapolated* from instant s to instant k, a method derived in [25]. The core idea is to store the filter state at time s and to modify the update step eqn. (5.6) at time k to account for the time delay to fuse the delayed measurement. Using this method, the correction terms take the following form:

$$\delta\hat{\boldsymbol{x}}_k = \boldsymbol{K}^{\text{GC}}_{\text{x},k}\left(\boldsymbol{z}^{\text{GC}}_k - \mathbf{h}^{\text{GC}}_{\text{x}}\left(\hat{\boldsymbol{x}}_{s|s-1}\right)\right), \tag{5.17a}$$

$$\delta\boldsymbol{P}_{\text{x},k} = -\boldsymbol{K}^{\text{GC}}_{\text{x},k}\boldsymbol{H}^{\text{GC}}_{\text{x},s}\boldsymbol{P}_{\text{x},s|s-1}\boldsymbol{M}_{\text{x}}^{\top}. \tag{5.17b}$$

The extrapolated measurement, $\tilde{\boldsymbol{z}}_k^{\text{GC}}$, is defined such that

$$\tilde{\boldsymbol{z}}^{\text{GC}}_k - \mathbf{h}^{\text{GC}}_{\text{x}}\left(\hat{\boldsymbol{x}}_k\right) = \boldsymbol{z}^{\text{GC}}_k - \mathbf{h}^{\text{GC}}_{\text{x}}\left(\hat{\boldsymbol{x}}_s\right) \tag{5.18}$$

holds. Based on this definition, the optimal gain is given by the Kalman gain

The authors note that, strictly speaking, optimality is only ensured for a linear system.

[25] Larsen et al., “Incorporation of time delayed measurements in a discrete-time Kalman filter.” (1998).

$$\boldsymbol{K}^{\text{GC}}_{\text{x},k} = \boldsymbol{M}_{\text{x}}\boldsymbol{P}_{\text{x},s}\boldsymbol{H}_s^{\text{GC}\top}\left(\boldsymbol{H}^{\text{GC}}_{\text{x},s}\boldsymbol{P}_{\text{x},s}\boldsymbol{H}^{\top}_{\text{x},s} + \boldsymbol{R}^{\text{GC}}_s\right)^{-1}. \tag{5.19}$$

Since the Kalman gain $\boldsymbol{K}^{\text{GC}}_{\text{x},k}$ needs to reflect the time delay the delay matrix $\boldsymbol{M}_{\text{x}}$ is introduced, which is calculated by

$$\boldsymbol{M}_{\text{x}} = \prod_{i=0}^{N-1}\left(\mathbf{I} - \boldsymbol{K}^{\text{GC}}_{\text{x},k-i}\boldsymbol{H}^{\text{GC}}_{\text{x},k-i}\right)\boldsymbol{\Phi}_{\text{x},k-i-1}, \tag{5.20}$$

and which satisfies the following relationship

$$\boldsymbol{P}_{\text{x},s}\boldsymbol{M}_{\text{x}}^{\top} = \mathbb{E}\left\{(\hat{\boldsymbol{x}} - \boldsymbol{x})_s(\hat{\boldsymbol{x}} - \boldsymbol{x})_k^{\top}\right\}, \tag{5.21}$$

where $(\hat{\boldsymbol{x}} - \boldsymbol{x})$ is the estimation error.

Substituting the index d for x, the correction terms $\delta\hat{\boldsymbol{d}}_k$ and $\delta\boldsymbol{P}_{\text{d},k}$ are obtained.

Using this method, only eqn. (5.20) needs to be evaluated at each time step, in addition to storing the filter state at time s in the form of $\hat{\boldsymbol{x}}_{s|s-1}$ and $\boldsymbol{P}_{\text{x},s|s-1}$ to be able to fuse the delayed measurement $\boldsymbol{z}_k^{\text{GC}}$ at time k.

5.5 Fault Detection

During the operation of the DFB gasification plant, faulty measurements occur, which have to be detected and isolated to ensure that they are not used in the state estimation. This involves discarding the measurements from the affected device and not using them in the a posteriori estimate eqns. (5.6) and (5.12).

One particular type of fault concerning the gas analysis equipment is related to the gas cleaning procedure preceding the analysis, which is detailed in Section 2.1. Since the impinger bottles are loaded with tars over time, it is necessary to replace them with ones containing fresh solvent. During the replacement, the sampling line will be interrupted and the composition data reported by the downstream measurement equipment does not reflect the actual gas composition. This scenario affects both online analyzers as well as the GC.

Furthermore, the GC is regularly used to analyze other product streams in the plant. Consequently, the same issue arises, namely that the reported data does not reflect the product gas composition during those periods.

In particular, a scalar measure is used to detect faults. This measure is strictly motivated by statistical reasoning, albeit the threshold parameters are determined heuristically rather than based on statistics, as will be explained in the following section.

5.5.1 General Kalman Filter-based Approach

For detecting faults, different approaches exist, including data-driven and model-based methods [6]. Common approaches for model-based fault detection in control systems are based on the analysis of a Kalman filter's innovation sequence $\boldsymbol{y}$ [13, 14, 45]. In the context of this work, this type of method is attractive since an EKF is already being used.

One such approach described in [45, p. 157] is outlined in the following, based on the linear system

$$\boldsymbol{x}_{k+1} = \boldsymbol{\Phi}\boldsymbol{x}_k + \boldsymbol{\Gamma}\boldsymbol{u}_k + \boldsymbol{w}_k\,, \tag{5.22a}$$

$$\boldsymbol{z}_k = \boldsymbol{H}\hat{\boldsymbol{x}}_k + \boldsymbol{v}_k\,. \tag{5.22b}$$

The process and measurement noises, denoted by $\boldsymbol{w}_k \sim \mathcal{N}(0, \boldsymbol{Q})$ and $\boldsymbol{v}_k \sim \mathcal{N}(0, \boldsymbol{R})$, respectively, are both assumed to have zero mean and covariances $\boldsymbol{Q}$ and $\boldsymbol{R}$, respectively. Additionally, both noise sequences are assumed to be uncorrelated:

$$\mathbb{E}\left\{\boldsymbol{w}_k \boldsymbol{v}_l^\top\right\} = \boldsymbol{0}\,. \tag{5.23}$$

[6] Chiang et al., *Fault Detection and Diagnosis in Industrial Systems*. (2001).

[14] Hajiyev et al., *Fault Diagnosis and Reconfiguration in Flight Control Systems*. (2003).

[45] Wang et al., *Model-Based Fault Diagnosis*. (2023).

Eqn. (5.22) is not connected to eqn. (5.1) but is solely introduced to illustrate the derivation of the fault measure in this section.

The assumption of zero mean white noise is also made for the initial condition for the estimation error $\tilde{\boldsymbol{x}}_0$:

$$\tilde{\boldsymbol{x}}_0 \sim \mathcal{N}(0, \boldsymbol{P}_0) . \tag{5.24}$$

Again, the initial condition is assumed to be uncorrelated with the noise sequences:

$$\mathbb{E}\left\{\tilde{\boldsymbol{x}}_0 \boldsymbol{w}_k^\top\right\} = \boldsymbol{0} , \quad \mathbb{E}\left\{\tilde{\boldsymbol{x}}_0 \boldsymbol{v}_k^\top\right\} = \boldsymbol{0} . \tag{5.25}$$

Based on these assumptions, it can be shown [45] that the innovation sequence $\boldsymbol{y}_k$ follows the distribution

$$\boldsymbol{y}_k \sim \mathcal{N}(0, \boldsymbol{\Sigma}_k) , \quad \text{where} \quad \boldsymbol{\Sigma}_k = \boldsymbol{H}\boldsymbol{P}_{k|k-1}\boldsymbol{H}^\top + \boldsymbol{R} , \tag{5.26}$$

where $\boldsymbol{\Sigma}_k$ is the covariance of the innovation sequence $\boldsymbol{y}_k$. In a fault scenario, $\boldsymbol{y}_k$ no longer satisfies eqn. (5.26). This can be exploited for detecting a fault by introducing the scalar measure

$$\lambda_k = \boldsymbol{y}_k^\top \boldsymbol{\Sigma}_k^{-1} \boldsymbol{y}_k , \tag{5.27}$$

n_y denotes the dimension of the innovation sequence.

which, under the earlier assumptions, satisfies a $\chi^2_{n_y}$-distribution with n_y degrees of freedom, i.e., the dimension of the innovation vector. A hypothesis test to determine whether eqn. (5.26) holds may therefore be formulated as follows:

$$H_0 : \lambda_k \sim \chi^2_{n_y} , \tag{5.28}$$

$$H_1 : \lambda_k \nsim \chi^2_{n_y} . \tag{5.29}$$

An arbitrary confidence level $1-\alpha$ may be defined to obtain a threshold parameter θ, such that

$$\mathbb{P}(\lambda_k \leq \theta) = 1 - \alpha . \tag{5.30}$$

The decision rule for the hypothesis test eqn. (5.28) may then be formulated by comparing the test statistic λ to the threshold θ:

$$\lambda_k \leq \theta \quad \text{Fault-free,} \tag{5.31a}$$

$$\lambda_k > \theta \quad \text{Faulty.} \tag{5.31b}$$

The test statistic may be computed for each of the available measurement sources separately and compared to a given threshold.

5.5.2 Heuristic Determination of the Fault Thresholds

The assumptions regarding the Gaussianness of the process noise and measurement noise sequences made in Section 5.1 are violated in the case of the soft sensor. As a consequence, the test statistic λ does not follow a χ^2-distribution, as is evident by looking at the histograms in Figure 5.3. Therefore, the threshold parameters θ are defined heuristically by analyzing the values of the fault measure λ during known faults in the historical data such that these events are detected. The aim is to set the thresholds as low as possible, to make the detection more sensitive, but also to set them as high as necessary to not detect a fault when in fact the deviation between prediction and observation originates from model limitations as opposed to faults in the measurements.

It is worth noting that, in contrast to the analyzer data for product gas and FG, the probability density function of the GC measurements exhibits a significant tail. This can be attributed to the fact that the GC device was used at times to analyze different gas streams and consequently did not reflect the actual product gas composition, leading to large values of the test statistic. In contrast, the periods in which the analyzers were reporting *false* data, i.e., when the gas cleaning impinger bottles were being exchanged, were rather short compared to the periods of normal operation.

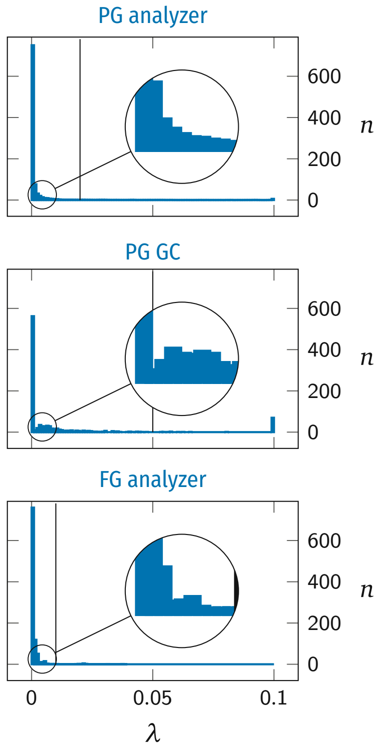

Figure 5.3: Histograms of the test statistics eqn. (5.27) for the three measurement sources. The histograms show the normalized number n of occurrences, such that the total area evaluates to 0. The thresholds for each of the sensors are also indicated and can be observed in Appendix C. The values for the test statistic were generated by running the soft sensor on historic data sets.

5.5.3 Additional Measures in the Case of a Fault

When a fault occurs in one of the measurement channels, the value of the associated test statistic is expected to increase gradually instead of abruptly. For this reason, due to the compromise between high sensitivity and low false alarm rate in defining the thresholds, several faulty measurements may already have been fused, once the threshold is exceeded.

In order to avoid these potentially false measurements to influence the filter state in subsequent iterations, two measures are taken. The covariance matrices $\boldsymbol{P}_\mathrm{x}$ and $\boldsymbol{P}_\mathrm{d}$ are recomputed for the last 12 time steps using only the prediction steps eqns. (5.3b) and (5.11b). In addition, the disturbance state is reset to the state at time $k-12$. At this point, the value 12 is chosen arbitrarily and is to be evaluated in Chapter 6.

6 Results

The soft sensor performance was validated as part of a gasification test conducted with the DFB gasification plant at TU Wien.

First, the individual models introduced in Section 4.2.1 entering the combined static model will be evaluated in Section 6.1 by comparing their predictions against that part of the historical data reserved for validation.

Subsequently, the soft sensor's performance during a gasification test will be discussed. The data shown in Section 6.2 and Appendix A.2 is therefore new and has not been used in the prior identification process. The analysis will include the estimation of the product gas composition in Section 6.2 with special focus on the water content, and the fault detection.

The comparison between predicted and measured flue gas composition and the estimated char flow rate during the test will be discussed more briefly in Section 6.3.

More emphasis will be laid on the time development of the disturbance states in Section 6.4, followed by an evaluation of the dynamic behavior of the system states in response to an interruption of the fuel feed in Section 6.5.

In addition, the stability and the observability will be evaluated in Section 6.6.

The chapter concludes with several suggestions for improvement of the soft sensor based on the evaluation of the gasification test.

6.1 Linear Model Evaluation

The individual models discussed above are evaluated using the validation data set. For this purpose parity plots, which compare the model predictions to the actual data, are shown in Figure 6.1.

It can be observed that for reactions eqns. (4.2a) to (4.2c) the models produce good predictions for the validation data, with the prediction errors predominantly within ±20 %.

In contrast, the predictions of reaction eqn. (4.2d) exhibit larger errors. It has been suggested in the literature [4] that

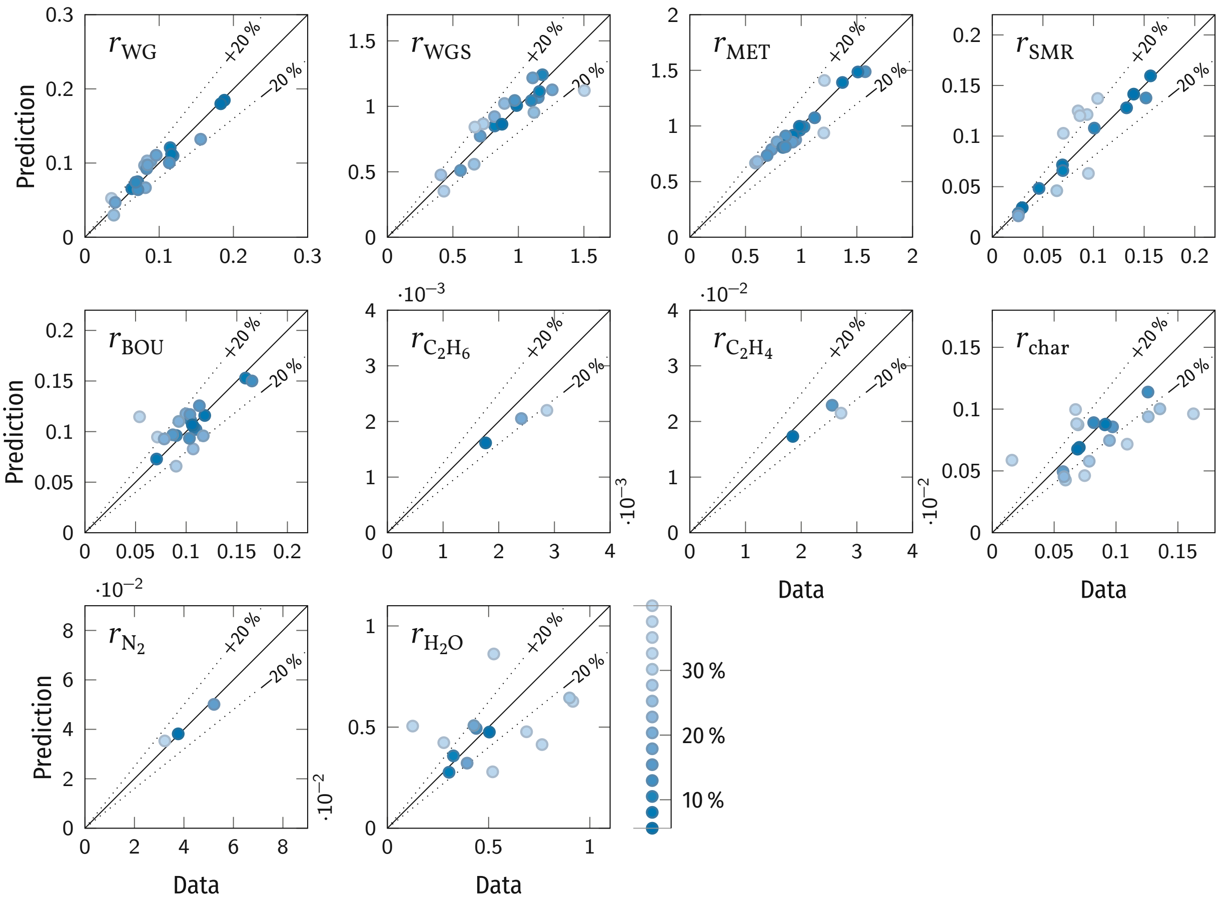

Figure 6.1: The parity plots show the performance of the regression models on the validation data. Aside from indicators for a prediction error of ±20 % the data points are colorized according to their prediction error.

changes in CH_4 concentration may be attributed to dilution effects, rather than conversion through the SMR reaction, which may explain the larger prediction errors.

While the model predictions for reaction eqn. (4.2e) are largely within the ±20 %-range, the data is clustered around a narrow range of values. This indicates a weak correlation with the model parameters.

As mentioned above, only a limited number of data points were available for the identification of the C_2 models. Therefore, the parity plots for both models provide only limited meaningfulness, despite the fact that the predictions express acceptable deviations from the data. The same is true for the N_2 model.

The model for predicting the loop seal split ratio exhibits substantial prediction errors, underlining that it may be regarded as a best-guess estimate only.

The largest errors among the models can be observed in the prediction of the char flow rate. This likely results from the char flow rate having been inferred from the mass balance (see Section 3.2.1) and has not been measured directly. Therefore, inaccuracies in flow rate and composition measurements naturally accumulate in the calculated value of the char flow rate.

6.2 Product Gas Composition

Overall, the soft sensor estimates of the product gas composition are in close agreement with the measurements, as can be seen in Figure 6.2. This is particularly true for the main components CO, CO_2, and CH_4, as well as for the C_2 components. This is a consequence of the corresponding values defined in the covariance matrices $\boldsymbol{Q}$ and $\boldsymbol{R}$, and the model correction. The O_2 concentration reported by the analyzer assumes values of $\tilde{\xi}_{O_2} \approx 2 \cdot 10^{-3}$ from the start until $t \approx 3\,\mathrm{h}$, being in good agreement with the measurements from the GC. After the first fault, it drops in a stepwise manner to $\tilde{\xi}_{O_2} \approx 10^{-4}$, while the GC measurement declines in a more continuous fashion. Some periods are missing from the analyzer graph due to negative reported values in combination with the logarithmic axis. The soft sensor's estimate for the O_2 concentration is almost constant during the whole test, albeit slightly above the value set in eqn. (4.11h), likely due to the mass balance eqn. (4.11k). Since the amount of oxygen in the product gas is considered of minor interest, this deviation between measurements and estimate is deemed acceptable.

In contrast, the soft sensor estimates for H_2 and O_2 deviate from the measurements. In the case of the H_2 estimate, this can be attributed to the absence of a disturbance state correcting the H_2 molar flow rate. Instead, it is only indirectly influenced by eqns. (4.11c) to (4.11f) through d_{CO}, d_{CO_2}, and d_{CH_4}. This may be mitigated by adjusting the value of the associated covariance. While there is a disturbance state associated with the O_2 concentration, it shows only a minimal effect due to the choice of the associated covariance. This is deemed acceptable since the O_2 concentration is considered to be of subordinate importance.

Correcting the model in this manner resulted in the water content estimate consistently and significantly exceeding the offline data. This is likely due to remaining errors in the H containing species' molar flow rate estimates. The deviation in the H_2 concentration estimates is accepted due to the prioritization of the accuracy of the product gas water content.

Figure 6.2 illustrates the effect of the delayed measurements. While the GC measurements are drawn at the time of sampling, the associated correction—in this case of the C_2H_4 mole fraction—is delayed by 12 min. The magnified portion of the diagram also illustrates the necessity to delay storing the filter state, which is detailed in Appendix A.1. . The instant the next sample is taken coincides with the instant before the correction takes effect. Thus, the resulting innovation used in the next correction would not take into account the correction induced by the previous measure-

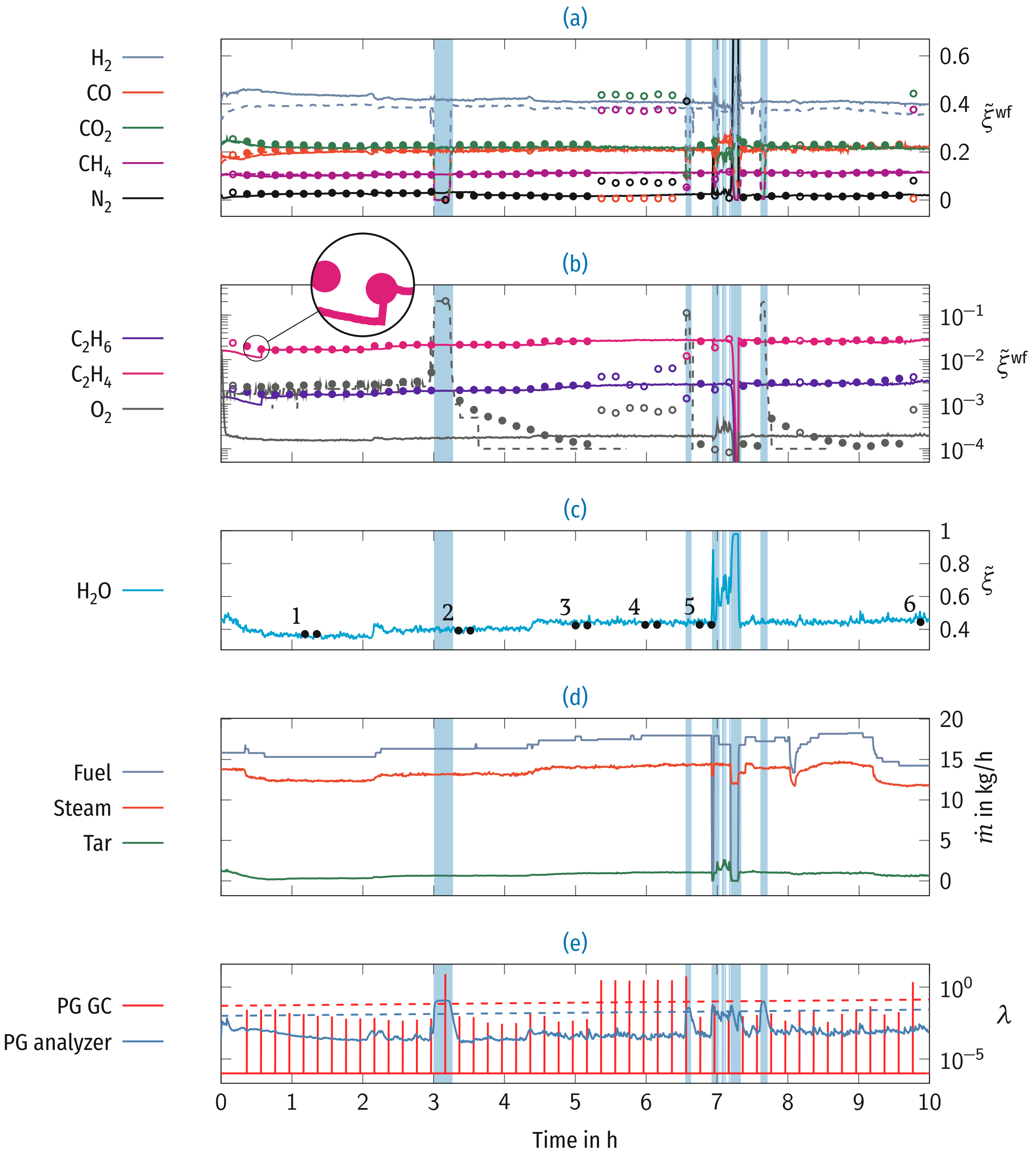

Figure 6.2: (a) Dry product gas concentrations of the major species for the gasification test run. —— indicates the soft sensor output, - - - indicates analyzer data and • indicates GC data which was fused. ∘ indicates GC data which was discarded. (b) Dry product gas concentrations of the minor species. (c) Water content with offline measurements indicated by •. (d) Fuel feed rate, steam feed rate and tar production rate. (e) Fault measures for the product gas analyzer and the GC. The corresponding thresholds are indicated by - - -. Periods during which product gas analyzer measurements were being discarded are highlighted by 🟦.

ment. However, a delay of one sample time instead of six should suffice, judging by the diagram.

6.2.1 Water Content

The estimated water content is in excellent agreement with the offline sampling data. Table 6.1 shows the largest relative error, which is 6.8 %. In addition to the offline sampling, the results obtained by IPSEpro are listed, which display a comparable maximum relative error of 7.4 %.

The soft sensor estimates and the IPSEpro results are also compared in Figure 6.3. This is a significant result, as it allows for continuous monitoring of the water content, thereby enabling the process to be optimized based on key performance indicators such as water conversion and cold gas efficiency. Otherwise, these values would only be available punctually whenever offline samples are collected.

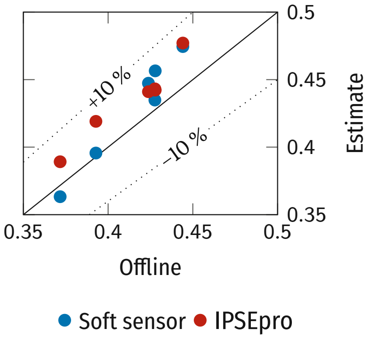

Figure 6.3: Comparison between soft sensor estimates and IPSEpro simulation results of the product gas water content.

Table 6.1: Comparison of product gas water content determined by offline sampling and the soft sensor's estimate. The sample indices refer to Figure 6.2. Adapted from [43].

	Absolute values			Relative error	
№	Offline	Soft sensor	IPSEpro	Soft sensor	IPSEpro
1	0.372	0.363	0.389	0.023	0.047
2	0.393	0.396	0.419	0.007	0.067
3	0.424	0.447	0.441	0.056	0.041
4	0.428	0.435	0.443	0.017	0.036
5	0.428	0.456	0.442	0.067	0.034
6	0.444	0.474	0.477	0.068	0.074

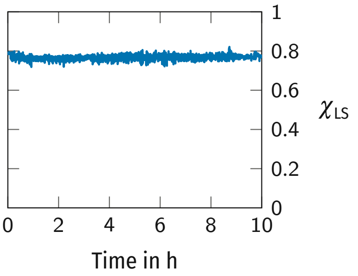

Figure 6.4: Estimated loop seal split ratio during the gasification test.

Additionally, Figure 6.4 shows the loop seal split ratio estimated based on eqn. (4.10). The predicted split ratio remains relatively constant throughout the whole gasification test at a value of $\chi_{\text{LS}} \approx 0.77$. This behavior may not be interpreted directly but can only be considered valid based on the agreement of the water content estimate with the offline analysis.

6.2.2 Tar Mass Flow

The tar production rate can be seen to remain below 2 kg/h throughout the gasification test. At this point, no offline analysis of the amount of tar in the product gas is available for comparison. Consequently, no assessment can be made of the accuracy of the soft sensor estimate for the tar production rate.

6.2.3 Fault Detection

During the test, several faults were successfully detected as indicated in Figure 6.2.

At $t \approx 3\,\mathrm{h}$, the analyzer measurements show a sharp drop, indicating that the sampling line was interrupted. The test statistic $\lambda^{\mathrm{PG,analyzer}}$ shows a sharp increase, exceeding the threshold and consequently leading to the fault being detected. The same is true for the value of $\lambda^{\mathrm{PG,GC}}$. The simulated product gas composition during the fault remained at a steady level as expected. This demonstrates the effectiveness of the model correction via the disturbance states. A similar scenario occurred at $t \approx 6.5\,\mathrm{h}$ and $t \approx 7.5\,\mathrm{h}$.

Between 5.3 hand6.5 h, the values of $\lambda^{\mathrm{PG,GC}}$ can be seen to exceed the threshold. This is a consequence of the GC having been used to monitor a different gas stream during this period. This is confirmed by observing the high amounts of CH_4 and CO_2 reported by the GC. As a consequence, the GC data were discarded during this period.

Around $t \approx 7\,\mathrm{h}$, several adjustments in the fuel flow rate occurred. This led to large fluctuations in the product gas composition, affecting both the measurements and the estimated values. The value of $\lambda^{\mathrm{PG,analyzer}}$ can be seen to fluctuate around the threshold value leading to repeated entering and exiting of the soft sensor's simulation mode. As a consequence of the interruption of the fuel feed rate, the static model change described in Section 5.5 was triggered. One potential solution to circumvent the frequent on-and-off switching of the soft sensor's fault mode within a brief period of time is to delay the switch back to normal operation when the value of the test statistic decreases below its threshold by a few time steps.

6.3 Flue Gas Composition and Char Flow Rate

Figure 6.5 shows the test run results for the flue gas composition. Step changes in the fuel feed rate (see Figure 6.2) can be observed to produce associated changes in the estimated char flow rate, which seems reasonable. With an increase in the char flow rate, the oil flow rate was lowered, while the air flow rate remained fairly constant. The combined effect of these observations appears to be a fairly constant flue gas composition. The soft sensor predictions of the flue gas composition are in close agreement with the analyzer measurements. It is worth pointing out that the molar flow rates of CO_2 and CO are not corrected using the flue gas analyzer measurements. Instead, these measurements are only used to correct the predicted char flow rate. This indicates

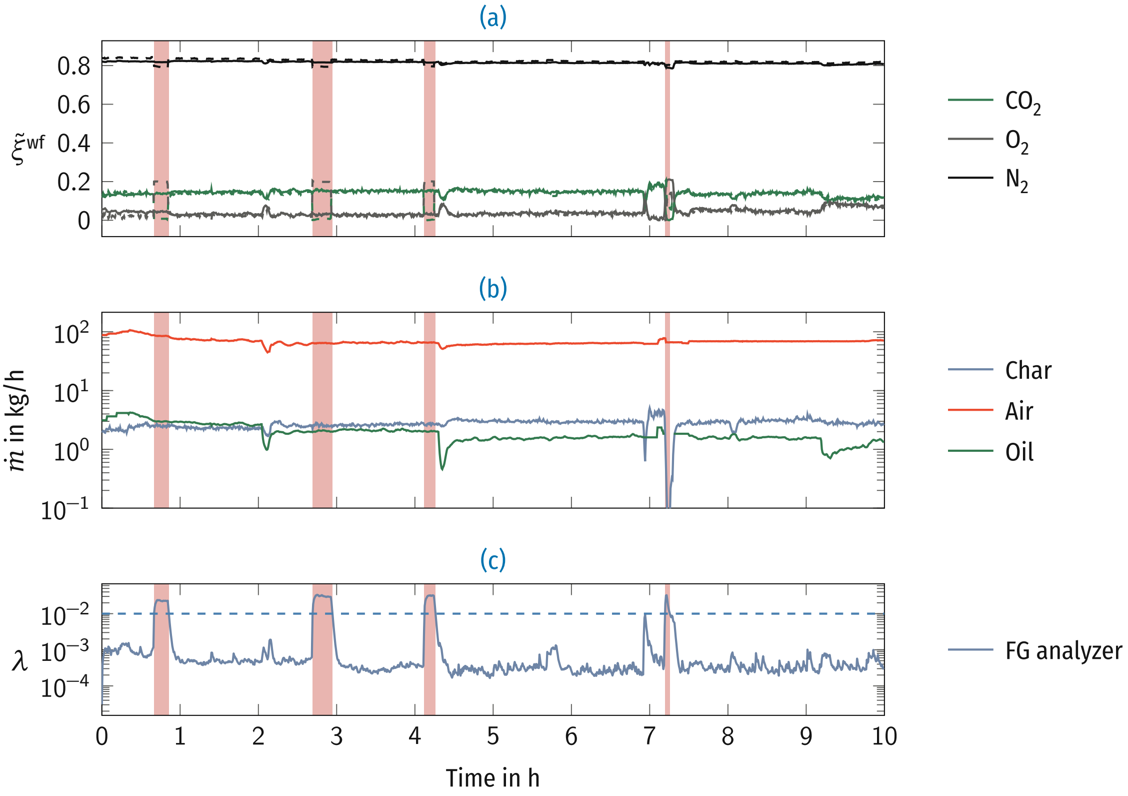

Figure 6.5: (a) Flue gas composition during the gasification test. The dashed line indicating the N$_2$ concentration is obtained using the closure condition $\sum \tilde{\xi}_i^{\mathrm{wf}} = 1$. (b) Estimated flow rate of char, and flow rates of air and oil. (c) Fault measure for the product gas analyzer. Periods during which measurements were being discarded are highlighted by 🟥.

that the char flow rate estimate is accurate since it directly impacts the combustion reactor carbon balance. However, no offline sampling is available to validate the estimates at this point.

6.3.1 Fault Detection

A total of five faults were recognized during the test run, as indicated by the fault measure λ in Figure 6.5, which coincides with sudden changes in the flue gas composition. During these occurrences, the char flow rate and the flue gas composition were simulated while the product gas composition continued to be corrected through the measurements from the product gas analyzer.

6.4 Model Corrections

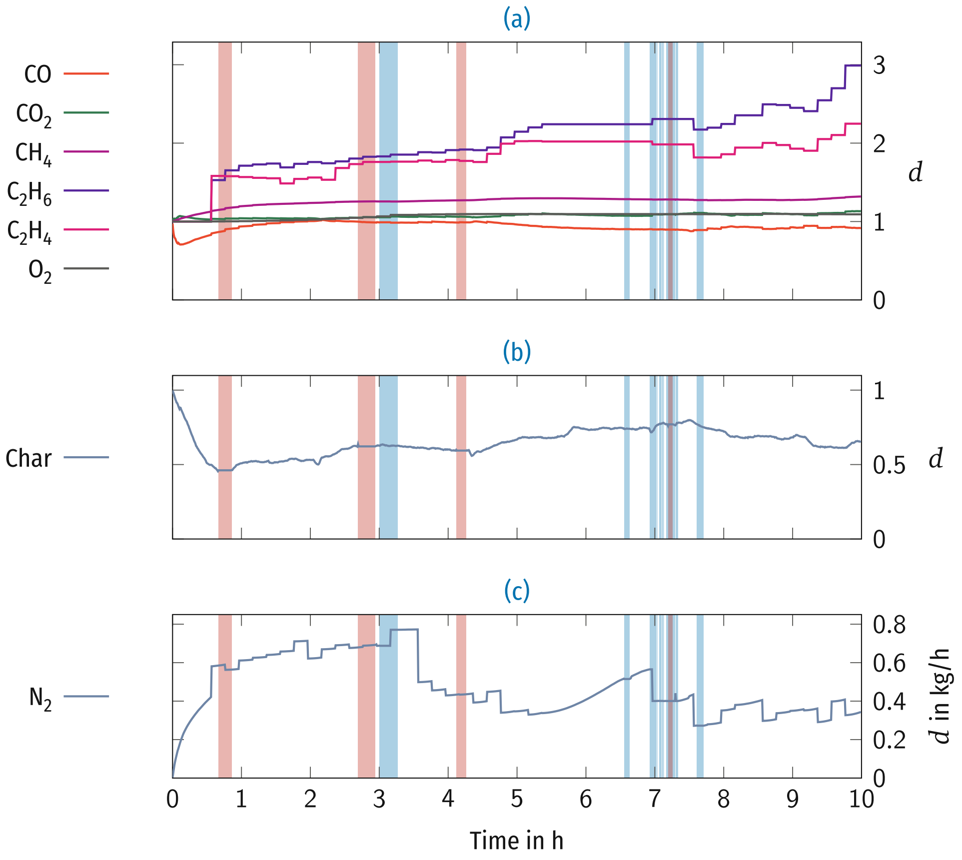

Figure 6.6: Time development of the disturbance states during the gasification test. Periods, during which measurements were being discarded, are highlighted by 🟦 and 🟥.

During the test, the disturbance states developed as expected over time, as can be observed in Figure 6.6. Notable step changes occur due to updates using the GC measurements.

As anticipated, the most significant corrections were observed for the gaseous components, particularly for the C_2 components. This is a consequence of the simplicity of the model, which links these species only to the CH_4 concentration. For this reason, their variances in the $\boldsymbol{Q}$ matrix were chosen relatively large, leading to larger corrections for a given discrepancy between measurement and prediction. It can also be seen that both disturbances were adjusted solely based on the GC measurements but not on the analyzer's, since it does not provide these data. The same argument holds true for the O_2 concentration, even more so, as the model simply predicts a constant value.

In contrast, the disturbances for CO, CO_2, and CH_4 are continuously adjusted based on the analyzer data. The graph does, however, also show steps at instances when GC data was fused. The disturbance state correcting the char production rate does not show any step changes, since the flue gas is only sampled by an online analyzer.

The disturbance for estimating the amount of N_2 entering the gasification reactor is presented as a mass flow. It is updated by both, the analyzer and the GC, however, the tuning parameters have been set such that the analyzer only leads to minor adjustments, while the GC measurement has a much greater influence. This was done because the analyzer does not measure N_2 but is only inferred using eqn. (3.3) in combination with the correction model discussed in Section 4.2.1.

6.5 Dynamic Behavior

In Figure 6.7, the response of the gasification reactor system to a step change in the fuel feed rate $\dot{m}_{\text{fuel}}$ can be observed. As expected, the N_2 concentration in the product gas quickly reaches a value of $\xi_{N_2}^{\text{wf}} = 1$. Similarly, the other component concentrations approach zero. The water concentration rises to $\xi_{H_2O} = 1 - \xi_{N_2}$.

The same is true for the mass flow rates of char and tar. The observed dynamic behavior is a direct consequence of the ansatz eqn. (4.19).

It is apparent that the water-free product gas concentrations ξ_i^{wf} do not obey a typical first-order dynamic response as might be expected considering eqn. (4.19). This is due to the definition of the mole fraction

$$\tilde{\xi}_i^{\mathrm{wf}} = \frac{\dot{n}_i}{\sum_{j \neq \mathrm{H_2O}} \dot{n}_j}\,, \quad \text{where} \qquad (6.1)$$
$$i, j \in \mathscr{I} = \{\mathrm{H_2}, \mathrm{CO}, \mathrm{CO_2}, \mathrm{CH_4}, \mathrm{C_2H_6}, \mathrm{C_2H_4}, \mathrm{N_2}, \mathrm{O_2}\}\,.$$

Taking the derivative of eqn. (6.1) with respect to time t and solving the corresponding differential equation to obtain the time development of the water-free mole fraction leads to

$$\tilde{\xi}_i^{\mathrm{wf}}(t) = \frac{\tilde{\xi}_{i,0}^{\mathrm{wf}}}{1 - \frac{f_{\mathrm{PG}}^{\mathrm{wf}}}{\dot{n}_{\mathrm{PG},0}^{\mathrm{wf}}}\left(1 - e^{t/\tau}\right)}\,, \qquad (6.2)$$

where $\tilde{\xi}_{i,0}^{\mathrm{wf}} = \tilde{\xi}_{i,0}^{\mathrm{wf}}(t_0)$ denotes the water-free composition, and $\dot{n}_{\mathrm{PG},0}^{\mathrm{wf}} = \dot{n}_{\mathrm{PG}}^{\mathrm{wf}}(t_0)$ is the water-free product gas molar flow rate both at the time of the input step.

$$f_{\mathrm{PG}}^{\mathrm{wf}} = \sum_{j \neq \mathrm{H_2O}} \dot{n}_j^{\mathrm{in}} = \hat{d}_{\mathrm{N_2}} = \text{const.} \qquad (6.3)$$

denotes the estimated N_2 molar flow rate entering the gasification reactor since all other product gas species' molar flow rates are set to zero according to eqn. (4.14).

This outcome permits the time constant τ to be recovered from the step response, by observing the following relationship.

A detailed derivation of this result, including underlying assumptions, is given in Appendix B.

$$\tau \approx \frac{t'' - t'}{2}\,. \qquad (6.4)$$

According to the derivation in Appendix B, the inflection point of the step response curve coincides with the point at which the concentration reaches half of its initial value, i.e.,

$$\left(t'', \tilde{\xi}_i^{\mathrm{wf}}(t'')\right) = \left(t_{1/2}, \tilde{\xi}_i^{\mathrm{wf}}(t_{1/2})\right)\,.$$

This is not the case here, as evidenced by Figure 6.7, where the characteristic values are indicated for the H_2 step response. As a consequence, the values of the time constants derived by using different reference points on the response curve differ significantly as Table 6.2 shows. For instance, the time constant associated with H_2 assumes two values differing by a factor of 5.

Notably, the step response appears to express a dead time as well, which is not considered in the model. This may be explained by the fact that the model assumes instant drying, devolatilization, and conversion of the fuel when entering

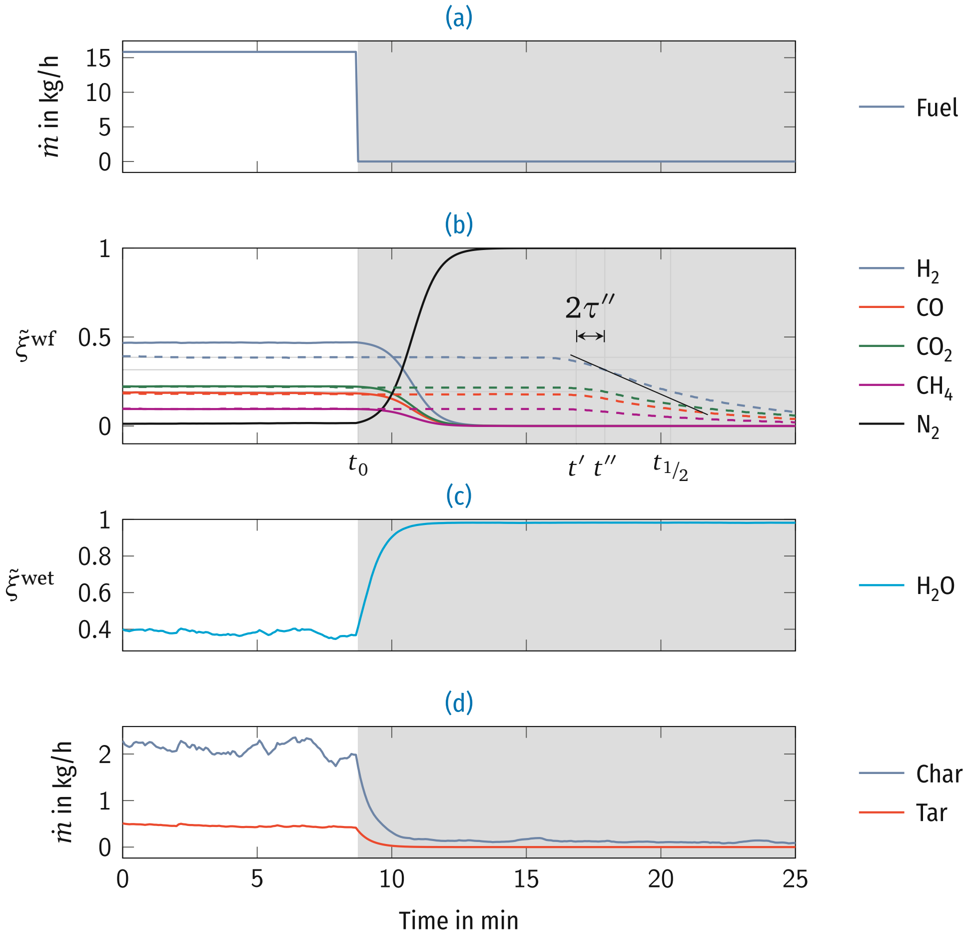

Figure 6.7: Step response to a change in fuel feed rate. Comparison between soft sensor output and analyzer measurements. (a) Fuel feed rate. (b) Product gas composition as calculated by the soft sensor ——, and by the analyzer - - -. Refer to the main text for description of the characteristic time instances of the H_2 step response indicated in the diagram. (c) Product gas water content. (d) Char and tar mass flow rates. Periods, during which measurements were being discarded, are highlighted by ▨.

the gasification reactor. This is, of course, an oversimplification. It is reasonable to assume that when the fuel feed rate is interrupted, i.e., $\dot{m}_{\mathrm{fuel}}(t_0) = 0\,\mathrm{kg/s}$, there is still unconverted fuel inside the bubbling bed, continuing to sustain the chemical reactions eqn. (4.2). This behavior may be accommodated in the model by introducing another system state that reflects the rate of change of the amount of fuel within the reactor and using this value instead of the measured fuel feed rate as input for the Hammerstein model (see Section 4.2).

Another potentially contributing factor to the apparent dead time observed in the step response to a change in fuel feed rate is the fact that the product gas composition is sampled downstream of the gasification reactor rather than from the bubbling bed directly (see Figure 2.1). However,

Table 6.2: Time constants obtained from step input response in Figure 6.7. Different values are given for $\tau'' = (t'' - t')/2$ and $\tau_{1/2} = (t_{1/2} - t')/2$ are given, where the index $1/2$ refers to the time at which $\tilde{\xi}_i^{\mathrm{wf}}(t_{1/2}) = \tilde{\xi}_{i,0}^{\mathrm{wf}}/2$ holds.

	$\tilde{\xi}_{i,0}^{\mathrm{wf}}$	$\tilde{\xi}_i^{\mathrm{wf}}(t'')$	τ'' in s	$\tilde{\xi}_i^{\mathrm{wf}}(t_{1/2})$	$\tau_{1/2}$ in min
H_2	0.386	0.316	32	0.193	2.3
CO	0.179	0.152	25	0.090	2.1
CO_2	0.218	0.182	25	0.109	3.3
CH_4	0.096	0.085	16	0.048	2.2

this effect is probably insignificant compared to the aforementioned argument.

While, in principle, the time constants for the system states can be easily adjusted to better resemble the observed dynamic behavior, the benefit of doing so is questionable, given that system dynamics are considered to be of subordinate importance compared with the steady-state predictions (see Chapter 4).

6.6 Observer Characteristics

In this section several characteristics of the observer will be presented, based on the gasification test data.

The stability and observability are evaluated based on the temporal development of the associated measures, which are detailed in sections 6.6.1 and 6.6.2, respectively. In order to analyze the stability and the observability of the soft sensor, the system state and the disturbances are aggregated in an *augmented* state to account for coupling effects. Consequently, the state transition model becomes

$$\boldsymbol{\Phi}_{\mathrm{xd}} = \begin{bmatrix} \boldsymbol{\Phi}_{\mathrm{x}} & \left.\frac{\partial \mathbf{f}(\boldsymbol{u},\hat{\boldsymbol{d}})}{\partial \hat{\boldsymbol{d}}}\right|_{\boldsymbol{u}_{k-1},\hat{\boldsymbol{d}}_{k-1}} \\ \mathbf{0} & \boldsymbol{\Phi}_{\mathrm{d}} \end{bmatrix}, \tag{6.5}$$

where the expression $\left.\frac{\partial \mathbf{f}(\boldsymbol{u},\hat{\boldsymbol{d}})}{\partial \hat{\boldsymbol{d}}}\right|_{\boldsymbol{u}_{k-1},\hat{\boldsymbol{d}}_{k-1}}$ accounts for the coupling, and the index xd denotes the augmented state. Furthermore, the estimation error covariance and the measurement sensitivity matrices become

$$\boldsymbol{H}_{\mathrm{xd}} = \begin{bmatrix} \boldsymbol{H}_{\mathrm{x}} \\ \boldsymbol{H}_{\mathrm{d}} \end{bmatrix} \quad \text{and} \tag{6.6a}$$

$$\boldsymbol{P}_{\mathrm{xd}} = \begin{bmatrix} \boldsymbol{P}_{\mathrm{x}} & \mathbf{0} \\ \mathbf{0} & \boldsymbol{P}_{\mathrm{d}} \end{bmatrix}, \tag{6.6b}$$

respectively. The Kalman gain for the augmented system is then obtained through [16]

$$\boldsymbol{K}^{\mathrm{ana}}_{\mathrm{xd},k} = \boldsymbol{P}_{\mathrm{xd},k|k-1}\boldsymbol{H}^{\mathrm{ana}\top}_{\mathrm{xd},k}\left(\boldsymbol{H}^{\mathrm{ana}}_{\mathrm{xd},k}\boldsymbol{P}_{\mathrm{xd},k|k-1}\boldsymbol{H}^{\mathrm{ana}\top}_{\mathrm{xd},k} + \boldsymbol{R}^{\mathrm{ana}}\right)^{-1}. \tag{6.7}$$

[16] Kalman, "A New Approach to Linear Filtering and Prediction Problems." (1960).

In contrast, the controllability of the soft sensor's states will not be discussed since control is outside the scope of this work.

In addition, the computational performance of the soft sensor during the test will be discussed in Section 6.6.3.

6.6.1 Stability

While a well-established theory exists regarding the stability of the (linear) Kalman filter, the non-linearity of the EKF equations precludes the formulation of general statements regarding stability in all circumstances. However, it is possible to evaluate a stability criterion at any given point in time, thus enabling the assessment of local stability of the EKF [2, p. 752]. Employing the definitions eqns. (6.5) and (6.6a), the observer has a stable solution if all eigenvalues of the stability matrix

[2] Baillieul et al., *Encyclopedia of Systems and Control.* (2021).

$$\boldsymbol{S}_{\mathrm{xd}} = (\boldsymbol{\Phi}_{\mathrm{xd}} - \boldsymbol{\Phi}_{\mathrm{xd}}\boldsymbol{K}_{\mathrm{xd}}\boldsymbol{H}_{\mathrm{xd}}) \tag{6.8}$$

are located in the open inner unit circle of the complex plane [39], i.e.,

$$\left|\gamma_{\mathrm{xd},i}\right| < 1 \forall i \in 1, \ldots, n_{\mathrm{x}} + n_{\mathrm{d}}\,. \tag{6.9}$$

[39] Su et al., "On existence, optimality and asymptotic stability of the Kalman filter with partially observed inputs." (2015).

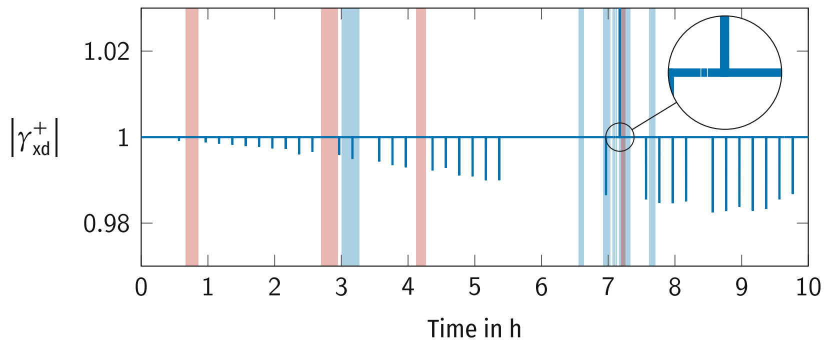

Figure 6.8: Absolute value of the largest eigenvalue γ^{+}_{xd} of the stability matrix of the augmented system. Fault regimes are indicated by 🟦 and 🟥.

Figure 6.8 shows the largest eigenvalue $\left|\gamma^{+}_{\mathrm{xd}}\right|$ of the stability matrix $\boldsymbol{S}_{\mathrm{xd}}$. It is evident from the diagram that the largest eigenvalue $\left|\gamma^{+}_{\mathrm{xd}}\right| = 1$ most of the time. In several instances, the case $\gamma^{+}_{\mathrm{xd}} < 1$ can be observed. These instances correspond to events when GC measurements were fused.

This observation matches the expectation, since the disturbances $d_{\mathrm{C_2H_6}}$ and $d_{\mathrm{C_2H_4}}$ are updated only through the GC. In all minor instances, they remain constant according to eqn. (4.21). Consequently, any potential errors remain constant as well, i.e., neither grow nor decay over time.

The fact that $\left|\gamma^{+}_{\mathrm{xd}}\right|$ assumes values close to 1 even in major instances can be explained by the values chosen for the covariances, in particular $\boldsymbol{Q}_{\mathrm{d}}$, in relation to the measurement noise matrices, $\boldsymbol{R}^{\mathrm{ana}}$ and $\boldsymbol{R}^{\mathrm{GC}}$, respectively, which only allow for small changes in the event of an update.

At $t \approx 7\,\mathrm{h}$, $\left|\gamma^{+}_{\mathrm{xd}}\right| > 1$, i.e., stability is lost temporarily. This loss of stability coincides with the soft sensor entering and exiting simulation mode for the product gas composition in between two successive fuel feed rate interruptions (see Figure 6.2). The soft sensor successfully recovered from this single event and continued to provide accurate estimates after the fuel feed rate had stabilized. Nevertheless, this behavior is undesirable and calls for further analysis in subsequent works.

6.6.2 Observability

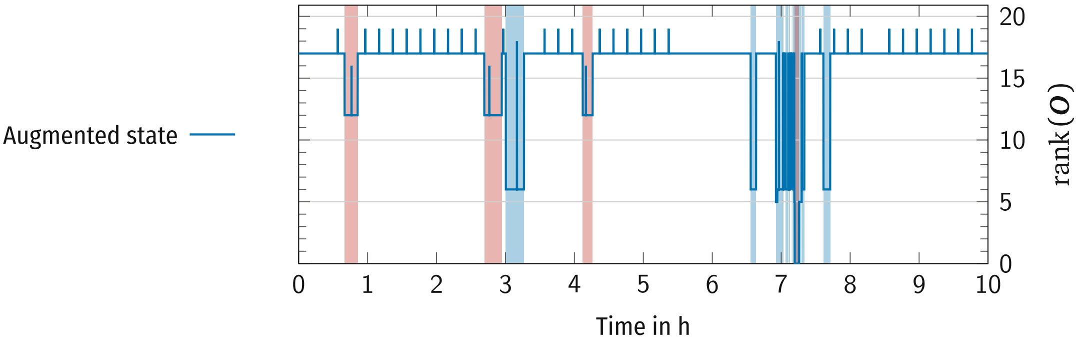

Figure 6.9: Rank of the observability matrix of the augmented system. Fault regimes are indicated by 🟦 and 🟥.

Observability is determined by the rank of the observability matrix

$$\boldsymbol{O}_{\mathrm{xd}} = \left[\boldsymbol{H}_{\mathrm{xd}}^{\top} \quad (\boldsymbol{H}_{\mathrm{xd}}\boldsymbol{\Phi}_{\mathrm{xd}})^{\top} \quad \left(\boldsymbol{H}_{\mathrm{xd}}\boldsymbol{\Phi}_{\mathrm{xd}}^{2}\right)^{\top} \quad \cdots \quad \left(\boldsymbol{H}_{\mathrm{xd}}\boldsymbol{\Phi}_{\mathrm{xd}}^{n-1}\right)^{\top}\right]^{\top}. \tag{6.10}$$

If the rank of the observability matrix equals the number of system states, the system is fully observable [31, p. 83]. Since the output equation eqn. (5.10) is non-linear, and, as a consequence, $\boldsymbol{H}_{\mathrm{xd}} \neq \mathit{const.}$, observability is evaluated locally for each time step.

[31] Ogata, *Modern Control Engineering (5th Edition)*. (2009).

The resulting time development of the rank of the observability matrix is presented in Figure 6.9. During normal

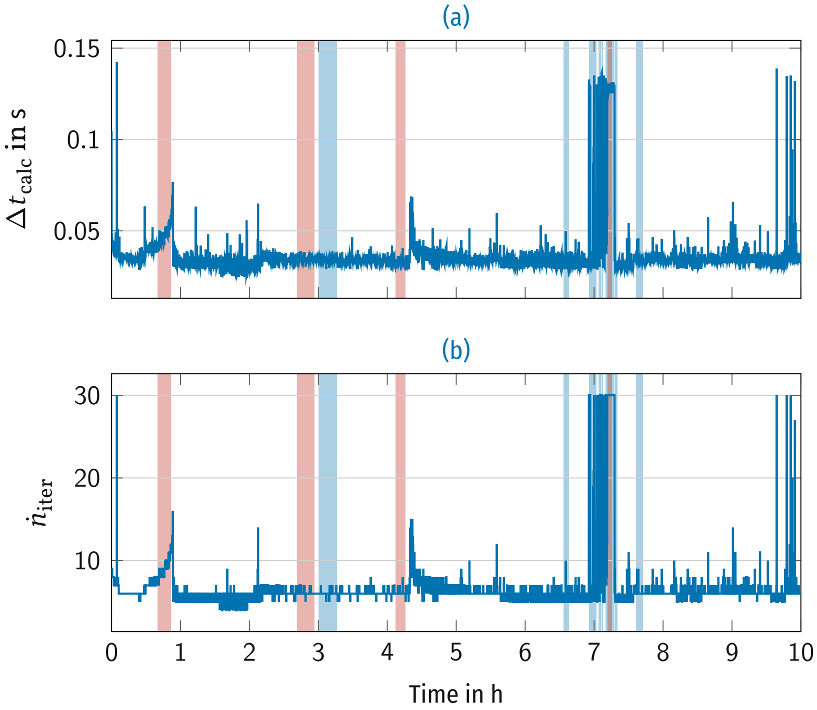

Figure 6.10: Computational performance of the soft sensor during the gasification test. (a) Time Δt_{calc} taken to solve eqn. (4.13). (b) Number of iterations taken to solve eqn. (4.13). Fault regimes are indicated by 🟦 and 🟥.

operation, excluding major instances, $\operatorname{rank}(\boldsymbol{O}_{\mathrm{xd}}) = 17 < n_{\mathrm{x}} + n_{\mathrm{d}} = 24$ shows that the augmented system is only partially observable.

During the course of the test run, the rank of the observability matrix decreased on several occasions. These events coincide with the soft sensor running in simulation mode due to a fault being detected in the product gas and the flue gas analyzer measurements, respectively. In the event of a fault in the product gas measurement being detected, the rank of the observability matrix drops by 11, whereas a fault in the flue gas measurement leads to a drop of 5 in rank. In the case of simultaneous faults in the product gas and flue gas measurements, the rank of the observability matrix drops to 0.

In addition to the aforementioned scenarios, the instances in which the GC measurement became available can be observed. The period during which the GC was sampling a different gas stream is also apparent since no change in the rank of the observability matrix occurs from $t \approx 5.5\,\mathrm{h}$ to $7\,\mathrm{h}$.

6.6.3 Computational Performance

In addition to the quality of the soft sensor's state estimates, its performance in terms of computational requirements is also of interest. Figure 6.10 shows two metrics of interest in this context. Firstly, the calculation time required to solve eqn. (4.13) is at $\Delta t_{\mathrm{calc}} \approx 50\,\mathrm{ms}$ most of the time, while reaching values of up to 150 ms in some instances, which is well below the allowed maximum of $T_s = 5\,\mathrm{s}$. This adds to the soft sensor's suitability for control purposes in comparison to the IPSEpro simulation, from which results are available every 1 min.

Of course, some additional processing is performed for each time step. However, the time requirements are insignificant in comparison.

As expected, the calculation time is directly proportional to the number of iterations required by the least-squares solver to obtain a solution. In the majority of cases, the solver takes $n_{\mathrm{iter}} \approx 7$ iterations to conclude. The maximum number of iterations is observed when fuel feed interruptions occur, where the value reaches $n_{\mathrm{iter}} = 30$. In fact, 30 is the maximum number of iterations allowed in order to restrict the calculation time, should the solver fail to find a feasible solution.

6.7 Potential Improvements

The review of the soft sensor's performance during the gasification test revealed a number of areas for improvement.

Firstly, the time constants for the system states should be adjusted according to the analysis in Section 6.5 to achieve better replication of the actual system dynamics.

Secondly, an additional system state may be introduced resembling the amount of fuel within the gasification reactor. Using this system state instead of the fuel feed rate in the reactor model eqn. (4.11) may also lead to more accurate predictions with respect to the system dynamics.

To avoid repeated switching between normal operation and simulation mode, a delay may be implemented such that the soft sensor would only exit simulation mode a specified number of samples after the indication by the fault measure is observed.

Additionally, the covariance values corresponding to the hydrogen flow rate $\dot{n}_{\mathrm{H_2}}$ should be adjusted to achieve better agreement with the analyzer data.

In addition to the aforementioned points, further investigation is necessary with respect to the tar production rate.

The suggested delay between the availability of a GC measurement and the sampling of the next one should be lowered from $6T_s \rightarrow T_s$.

7 Conclusion

The present work describes the development of an EKF-based soft sensor using a Hammerstein model for system state prediction. Another EKF was introduced to estimate disturbances used to improve the underlying static model of the gasification reactor. Based on a gasification test, the soft sensor was shown to yield reliable results for the product gas composition. In particular, the estimates of the water content in the product gas were shown to be in excellent agreement with the offline analysis. Comparison with process simulation results demonstrated that the soft sensor is on par in terms of accuracy while being far less demanding in terms of computational load. While the soft sensor also produces estimates for the char and tar flow rates, no offline data was available at the time of writing to validate these estimates.

Concerning the tuning parameters of the soft sensor, the covariance matrices and the time constants, the gasification test results revealed the need for minor revisions.

The soft sensor will contribute to the research on the DFB gasification plant at the TU Wien, in particular targeting plant operation and control. Accurate real-time estimates of the product gas water content permit the plant control software to optimize plant operation with respect to key performance indicators such as cold gas efficiency, which is evaluated on a dry product gas basis.

While the soft sensor is tailored to a specific plant, including a specific type of fuel, the overall concept may be applied to similar processes as well.

Bibliography

[1] Global Carbon Budget (2023) – with major processing by Our World in Data, "Annual CO_2 emissions – GCB" [dataset]. Global Carbon Project, "Global Carbon Budget" [original data]. URL: `ourworldindata.org/grapher/annual-co2-emissions-per-country` (visited on 03/05/2024).

[2] John Baillieul et al., eds. *Encyclopedia of Systems and Control*. 2nd ed. Springer Cham, June 30, 2021. XLII, 2469. ISBN: 9783030441845. DOI: `10.1007/978-3-030-44184-5`.

[3] F. Benedikt et al. "Fuel flexible gasification with an advanced 100 kW dual fluidized bed steam gasification pilot plant." In: *Energy* 164 (Dec. 2018), pp. 329–343. ISSN: 0360-5442. DOI: `10.1016/j.energy.2018.08.146`.

[4] Florian Benedikt et al. "Assessment of correlations between tar and product gas composition in dual fluidized bed steam gasification for online tar prediction, biomass." In: *Applied Energy* 238 (2019), pp. 1138–1149. ISSN: 0306-2619. DOI: `10.1016/j.apenergy.2019.01.181`.

[5] Sergey Cherednichenko et al. *Online water vapor detection in the product gas from indirect gasification*. Res. Rep. 2013:244. Malmö, Sweden: Svenskt Gastekniskt Center AB, 2013.

[6] Leo H. Chiang et al. *Fault Detection and Diagnosis in Industrial Systems*. Advanced Textbooks in Control and Signal Processing. Springer, 2001. ISBN: 978-1-852-33327-0.

[7] Verein Deutscher Ingenieure/Verband Deutscher Elektrotechniker (1991). VDI/VDE 2041:1991. *Durchflussmessung mit Drosselgeräten. Blenden und Düsen für besondere Anwendungen*. Beuth Verlag GmbH.

[8] Esref Eskinat et al. "Use of Hammerstein models in identification of nonlinear systems." In: *AIChE J.* 37.2 (Feb. 1991), pp. 255–268. ISSN: 1547-5905. DOI: `10.1002/aic.690370211` .

[9] Luigi Fortuna et al., eds. *Soft Sensors for Monitoring and Control of Industrial Processes*. SpringerLink. London: Springer London, 2007. 270179 pp. ISBN: 9781846284809.

[10] C. Franco et al. "The study of reactions influencing the biomass steam gasification process." In: *Fuel* 82.7 (May 2003), pp. 835–842. ISSN: 0016-2361. DOI: `10.1016/s0016-2361(02)00313-7`.

[11] Hans O. A. Fredriksson et al. “Olivine as tar removal catalyst in biomass gasification: Catalyst dynamics under model conditions.” In: *Applied Catalysis B: Environmental* 130-131 (Feb. 2013), pp. 168–177. DOI: `10.1016/j.apcatb.2012.10.017`.

[12] Josef Fuchs et al. “A general method for the determination of the entrainment in fluidized beds.” In: *The International Journal of Multiphysics* 12 (Dec. 2018), pp. 359–371. DOI: `10.21152/1750-9548.12.4.359`.

[13] Janos J. Gertler. *Fault detection and diagnosis in engineering systems*. Includes bibliographical references and index. New York: Dekker, 1998. 484 pp. ISBN: 0824794273. DOI: `10.1201/9780203756126`.

[14] Chingiz Hajiyev et al. *Fault Diagnosis and Reconfiguration in Flight Control Systems*. Springer US, 2003. DOI: `10.1007/978-1-4419-9166-9`.

[15] Petr Kadlec et al. “Data-driven Soft Sensors in the process industry.” In: *Comput. Chem. Eng.* 33.4 (Apr. 2009), pp. 795–814. ISSN: 0098-1354. DOI: `10.1016/j.compchemeng.2008.12.012`.

[16] R. E. Kalman. “A New Approach to Linear Filtering and Prediction Problems.” In: *Journal of Basic Engineering* 82.Series D (Mar. 1960), pp. 35–45. ISSN: 0021-9223. DOI: `10.1115/1.3662552`.

[17] S. Karellas et al. “Analysis of the product gas from biomass gasification by means of laser spectroscopy.” In: *Opt. Lasers Eng.* 45.9 (Sept. 2007), pp. 935–946. ISSN: 0143-8166. DOI: `10.1016/j.optlaseng.2007.03.006`.

[18] Stefan Kern et al. “Gasification of wood in a dual fluidized bed gasifier: Influence of fuel feeding on process performance.” In: *Chemical Engineering Science* 90 (Mar. 2013), pp. 284–298. ISSN: 0009-2509. DOI: `10.1016/j.ces.2012.12.044`.

[19] Jun Young Kim et al. “Predicting biomass composition and operating conditions in fluidized bed biomass gasifiers: An automated machine learning approach combined with cooperative game theory.” In: *Energy* 280.280 (Oct. 2023), p. 128138. ISSN: 0360-5442. DOI: `10.1016/j.energy.2023.128138`.

[20] Maximilian Kolbitsch. “First fuel tests at a novel 100 kWth dual fluidized bed steam gasification pilot plant.” PhD thesis. TU Wien, 2016.

[21] Stefan Koppatz. “Outlining active bed materials for dual fluidised bed biomass gasification: in-bed catalysts and oxygen/carbonate looping behaviour.” PhD thesis. TU Wien, 2012.

[22] J. Kortela et al. “Fuel moisture soft-sensor and its validation for the industrial BioPower 5 CHP plant.” In: *Applied Energy* 105 (2013), pp. 66–74. ISSN: 0306-2619. DOI: `10.1016/j.apenergy.2012.12.049`.

[23] Matthias Kuba et al. “Influence of coated olivine on the conversion of intermediate products from decomposition of biomass tars during gasification.” In: *Biomass Conversion and Biorefinery* 7.1 (Apr. 2016), pp. 11–21. DOI: `10.1007/s13399-016-0204-z`.

[24] D. Kunii et al. *Fluidization Engineering*. Ed. by Howard Brenner. Chemical Engineering. Butterworth-Heinemann, 1991, p. 491. ISBN: 0409902330.

[25] T. D. Larsen et al. “Incorporation of time delayed measurements in a discrete-time Kalman filter.” In: *Proceedings of the 37th IEEE Conference on Decision and Control (Cat. No.98CH36171)*. Vol. 4. IEEE, 1998, 3972–3977 vol.4. DOI: `10.1109/cdc.1998.761918`.

[26] K. S. Lim et al. “Hydrodynamics of gas-solid fluidization.” In: *International Journal of Multiphase Flow* 21 (supp-S Dec. 1995), pp. 141–193. DOI: `10.1016/0301-9322(95)00038-y`.

[27] K Maniatis et al. “Tar Protocols. IEA Bioenergy Gasification Task.” In: *Biomass and Bioenergy* 18.1 (Jan. 2000), pp. 1–4. DOI: `10.1016/s0961-9534(99)00072-0`.

[28] A. M. Mauerhofer et al. “Dual fluidized bed steam gasification: Change of product gas quality along the reactor height.” In: *Energy* 173 (2019), pp. 1256–1272. ISSN: 0360-5442. DOI: `https://doi.org/10.1016/j.energy.2019.02.025`.

[29] Somya Mishra et al. “Review on biomass gasification: Gasifiers, gasifying mediums, and operational parameters.” In: *Materials Science for Energy Technologies* 4 (2021), pp. 329–340. ISSN: 2589-2991. DOI: `10.1016/j.mset.2021.08.009`.

[30] Gapminder (2023), “GDP per capita Dataset” version 30 [dataset]. URL: `gapminder.org/data/documentation/gd001/` (visited on 03/05/2024).

[31] Katsuhiko Ogata. *Modern Control Engineering (5th Edition)*. 5th ed. Prentice-Hall electrical engineering series. Instrumentation and controls series. Prentice Hall, 2009. ISBN: 9780136156734.

[32] Yngve Ögren et al. “Development of a vision-based soft sensor for estimating equivalence ratio and major species concentration in entrained flow biomass gasification reactors.” In: *Appl. Energy* 226.226 (Sept. 2018), pp. 450–460. ISSN: 0306-2619. DOI: `10.1016/j.apenergy.2018.06.007`.

[33] J. Pecho et al. “Elucidation of the function of olivine in biomass gasification.” In: (Jan. 2004). ISSN: 1423-7342.

[34] A. Rogina et al. “Soft sensor for continuous product quality estimation (in crude distillation unit).” In: *Chem. Eng. Res. Des.* 89.10 (Oct. 2011), pp. 2070–2077. ISSN: 0263-8762. DOI: `10.1016/j.cherd.2011.01.003`.

[35] Gapminder (2023), “Life expectancy Dataset” version 12 [dataset]. URL: `gapminder.org/data/documentation/gd004/` (visited on 03/05/2024).

[36] G. Schuster et al. “Biomass steam gasification – an extensive parametric modeling study.” In: *Bioresour. Technol.* 77.1 (Mar. 2001), pp. 71–79. DOI: `10.1016/S0960-8524(00)00115-2`.

[37] S.I. Seneviratne et al. “Weather and Climate Extreme Events in a Changing Climate.” In: *Climate Change 2021: The Physical Science Basis. Contribution of Working Group I to the Sixth Assessment Report of the Intergovernmental Panel on Climate Change*. Ed. by V. Masson-Delmotte et al. Cambridge, United Kingdom and New York, NY, USA: Cambridge University Press, 2021, pp. 1513–1766. DOI: `10.1017/9781009157896.013`.

[38] Lukas Stanger et al. “Dynamic modeling of dual fluidized bed steam gasification for control design.” In: *Energy* 265 (Feb. 2023), p. 126378. DOI: `10.1016/j.energy.2022.126378`.

[39] Jinya Su et al. “On existence, optimality and asymptotic stability of the Kalman filter with partially observed inputs.” In: *Automatica* 53 (2015), pp. 149–154. ISSN: 0005-1098. DOI: `10.1016/j.automatica.2014.12.044`.

[40] Inc. The MathWorks. *Constrained Nonlinear Optimization Algorithms. fmincon Interior Point Algorithm*. URL: `de.mathworks.com/help/optim/ug/constrained-nonlinear-optimization-algorithms.html#brnpd5f` (visited on 07/11/2023).

[41] Inc. The MathWorks. *stepwiselm. Algorithms*. URL: `de.mathworks.com/help/stats/stepwiselm.html#bt0dbnp-6` (visited on 07/11/2023).

[42] Mahshad Valipour et al. “State estimation and sensor location for Entrained-Flow Gasification Systems using Kalman Filter.” In: *Control Engineering Practice* 108 (2021), p. 104702. ISSN: 0967-0661. DOI: `doi.org/10.1016/j.conengprac.2020.104702`.

[43] Jonas Vogler et al. “Soft Sensor Design for Product Gas Composition Monitoring Including Fault Isolation in a Dual Fluidized Bed Biomass Gasifier.” In: *2024 International Conference on Control, Automation and Diagnosis (ICCAD)* (May 15, 2024). Paris, France: IEEE, Dec. 15, 2023, pp. 1–7. Forthcoming.

[44] Lijun Wang. *Sustainable Bioenergy Production*. Ed. by L. Wang. CRC Press, Apr. 10, 2014, p. 583. ISBN: 9780429096068. DOI: `10.1201/b16764`.

[45] Zhenhua Wang et al. *Model-Based Fault Diagnosis. Methods for State-Space Systems*. Ed. by Janusz Kacprzyk et al. Vol. 221. Studies in Systems, Decision and Control. Springer Nature Singapore, 2023. DOI: `10.1007/978-981-19-6706-1`.

A Soft Sensor Implementation and Monitoring Interface

The following appendix provides additional reference to the implementation of the soft sensor's features in program code. For this purpose the soft sensor algorithm is illustrated using simplified, commented pseudocode. Additionally, a description of the online monitoring interface developed within the scope of this work is given.

A.1 Description of the Observer Algorithm

To concisely summarize the implementation of the of the soft sensor's features introduced in Chapter 5, they are described briefly in the following section by means of pseudo code.

First, eqn. (4.20) is solved iteratively in line 2 to obtain the static model prediction of the system state based on the input vector. This is followed by the evaluation of eqn. (5.3). Using the a priori estimate, the measurement sensitivity matrix $\boldsymbol{H}_k$, the output vector $\mathbf{h}_k$ and the innovation $\boldsymbol{y}_k$ can be computed, as well as the test statistic λ for both the PG analyzer and the FG analyzer.

Algorithm 1 State Prediction

```
1: function SENSOR($\boldsymbol{u}_k$,$\boldsymbol{z}_k$)
2:     $\mathbf{f}\left(\boldsymbol{u},\hat{\boldsymbol{d}}\right) \leftarrow \operatorname{argmin}_{\boldsymbol{x}} \left\|\mathbf{F}(\boldsymbol{u}_{k-1},\bar{\boldsymbol{x}}_{k-1},\hat{\boldsymbol{d}}_{k-1})\right\|_2^2$    ▷ Solve eqn. (4.20)
3:     $\hat{\boldsymbol{x}}_{k|k-1} \leftarrow \boldsymbol{\Phi}\hat{\boldsymbol{x}}_{k-1} + \boldsymbol{\Gamma}\mathbf{f}\left(\boldsymbol{u},\hat{\boldsymbol{d}}\right)$    ▷ Solve eqn. (5.3)
4:     $\boldsymbol{H}_k \leftarrow \boldsymbol{H}\left(\hat{\boldsymbol{x}}_{k|k-1}\right), \mathbf{h}_k \leftarrow \mathbf{h}\left(\hat{\boldsymbol{x}}_{k|k-1}\right), \boldsymbol{y}_k \leftarrow \boldsymbol{z}_k - \mathbf{h}_k$    ▷ Evaluate eqns. (5.9) and (5.13) to (5.15)
```

Having determined the values λ for both analyzers, the actual fault detection is performed in line 5 in algorithm 1. If a fault is detected, the covariance matrix $\boldsymbol{P}$ is recomputed from time step $k-12,\ldots,k-1$ using only the a priori estimates, i.e., it is purely simulated, while the disturbance states are reset to their values at $k-12$. This is done in case the fault detection is not sensitive enough and detects the fault late. This approach ensures that any potentially faulty values will not affect future estimates. Additionally, the entries in the observer matrix $\boldsymbol{H}$ associated with the faulty sensor are reset to $\mathbf{0}$ in line 18.

Algorithm 1 (Continued) Analyzer Fault Handling

```
 5:   Evaluate: $\lambda_k^{\text{PG analyzer}}, \lambda_k^{\text{FG analyzer}}$          ▷ eqn. (5.27)
 6:   for $i$ in $\{\text{PG analyzer}, \text{FG analyzer}\}$ do
 7:       if $\lambda_{i,k} > \theta$ then                                ▷ Fault detected?
 8:           $\boldsymbol{P}_{k-1} \leftarrow \boldsymbol{P}_{k-12}$                      ▷ Recalculate $\boldsymbol{P}$
 9:           for $j \leftarrow 1, 11$ do
10:               $\boldsymbol{P}_{k-1} \leftarrow \boldsymbol{\Phi}\boldsymbol{P}_{k-1}\boldsymbol{\Phi}^\top + \boldsymbol{Q}$
11:           end for
12:           $\hat{\boldsymbol{d}}_{k-1} \leftarrow \hat{\boldsymbol{d}}_{k-12}$                ▷ Reset disturbances
13:       end if
14:   end for

15:   $\boldsymbol{P}_{k|k-1} \leftarrow \boldsymbol{\Phi}\boldsymbol{P}_{k-1}\boldsymbol{\Phi}^\top + \boldsymbol{Q}$                    ▷ Predict $\boldsymbol{P}$

16:   for $i$ in $\{\text{PG analyzer}, \text{FG analyzer}\}$ do
17:       if $\lambda_{i,k} > \theta_i$ or $\dot{m}_{\text{fuel}} = 0$ then
18:           $\boldsymbol{H}_k^i \leftarrow \boldsymbol{0}$                           ▷ Ignore measurements
19:       end if
20:   end for
```

It is necessary to handle the delayed measurements by the GC and the fault detection for the GC together since the test statistic λ_s can only be computed once the GC measurement data becomes available. If a major instance occurs, i.e., a GC measurement is available, it is checked, whether a previous major instance has already occurred. If this is not the case, the measurement is discarded, since at this point the filter state from the time of sampling is unknown. In the alternative scenario, the innovation $\boldsymbol{y}_s$ and, subsequently, the test statistic λ_s^{GC} are evaluated using the previously stored output $\mathbf{h}_s$. In the event of a fault, the measurement is discarded. Otherwise, the Kalman gain for the delayed measurement is computed, followed by the correction values for the a posteriori estimates of $\hat{\boldsymbol{x}}$, $\hat{\boldsymbol{d}}$ and $\boldsymbol{P}$.

For all minor instances, only the delay matrix $\boldsymbol{M}^*$ needs to be updated according to eqn. (5.20) and the fault measure and the corrections are set to 0.

If the last major instance was recorded six time steps prior to the current one, the delay matrix is reinitialized (line 43), and the filter state, comprising the covariance matrix $\boldsymbol{P}$, the observer matrix $\boldsymbol{H}$, and the value of the output function $\mathbf{h}$, is stored (line 44).

Algorithm 1 (Continued) Delayed Measurements Handling

```
    if major_instance = true then
        if previous_major_instance = true then
            $y_s \leftarrow z_k^* - \mathbf{h}_s$                                   ▷ Calculate innovation …
            $\lambda_s^{\mathrm{GC}} \leftarrow y_s^\top \Sigma_s y_s$                    ▷ and fault measure
            if $\lambda_s^{\mathrm{GC}} > \theta_{\mathrm{GC}}$ then                       ▷ Fault detected?
                $\delta\hat{x}_k \leftarrow 0, \delta\hat{d}_k \leftarrow 0, \delta P_k \leftarrow 0$        ▷ No correction
            else
                $K_k^* = M^* P_s H_s^\top \left(H_s P_s H_s^\top + R_s\right)^{-1}$   ▷ Calculate corrections (eqns. (5.17 a) and (5.19))
                $\delta\hat{x}_k \leftarrow K_{\mathrm{x},k}^* y_{\mathrm{x},s}$
                $\delta\hat{d}_k \leftarrow K_{\mathrm{d},k}^* y_{\mathrm{d},s}$
                $\delta P_k \leftarrow -K_k^* H_s P_{s|s-1} M^{*\top}$
            end if
        else                              ▷ Filter state from time of sampling not available
            $\delta\hat{x}_k \leftarrow 0, \delta\hat{d}_k \leftarrow 0, \delta P_k \leftarrow 0$            ▷ No correction
            previous_major_instance←true
        end if
    else
        $\lambda_s^{\mathrm{GC}} \leftarrow 0$
        $M^* \leftarrow M^* (\mathrm{I} - K_k H_k) \Phi$                  ▷ Calculate delay matrix eqn. (5.20)
        $\delta\hat{x}_k \leftarrow 0, \delta\hat{d}_k \leftarrow 0, \delta P_k \leftarrow 0$
    end if
    if time_since_last_major_instance = $6T_s$ then                  ▷ Sampling instant?
        $M^* \leftarrow \mathrm{I}$                                        ▷ Reinitialize delay matrix
        $P_s \leftarrow P_{k|k-1}, H_s \leftarrow H_k\left(\hat{x}_{k|k-1}\right), \mathbf{h}_s \leftarrow \mathbf{h}\left(\hat{x}_{k|k-1}\right)$   ▷ Store filter state
    end if
```

Finally, the a posteriori estimate is computed and the filter state returned as can be seen in algorithm 1.

Algorithm 1 (Continued) A Posteriori Estimate

```
    $K_k \leftarrow P_{k|k-1} H_k^\top \left(H_k P_{k|k-1} H_k^\top + R\right)$

    $\hat{x}_k \leftarrow \hat{x}_{k|k-1} + K_{\mathrm{x},k}\, y_k + \delta\hat{x}_k$
    $\hat{d}_k \leftarrow \hat{d}_{k|k-1} + K_{\mathrm{d},k}\, y_k + \delta\hat{d}_k$
    $P_k \leftarrow (\mathrm{I} - K_k H_k) P_{k|k-1} + \delta P_k$

    return $\hat{x}_k, \hat{d}_k, P_k$
end function
```

A.2 Soft Sensor Monitoring Interface

A graphical interface was developed to be able to monitor the soft sensor output during operation. Figure A.1 shows the monitor at the end of the test run. Two plots show the major and minor product gas species concentrations output by the soft sensor and the GC, respectively. The product gas analyzer data is not displayed for clarity. Additionally, the water content, char, and tar mass flows are being displayed. Furthermore, fault regimes are indicated by a blue background for the product gas and red for the flue gas. Instances of the GC measurement being fused are indicated by minor tick marks on the horizontal axis of all plots. In addition to the plot legends, an info box includes the aforementioned description of the graphical elements, as well as information on the calculation time, which was, on average, 0.05 s.

Since the duration of the plant operation is not known a priori, the horizontal axis limits are compared to the current time, at each update of the diagram, and adjusted as necessary.

In addition to the graphical output, the soft sensor writes composition, mass flows, and information about the fault regime into a text file in each iteration.

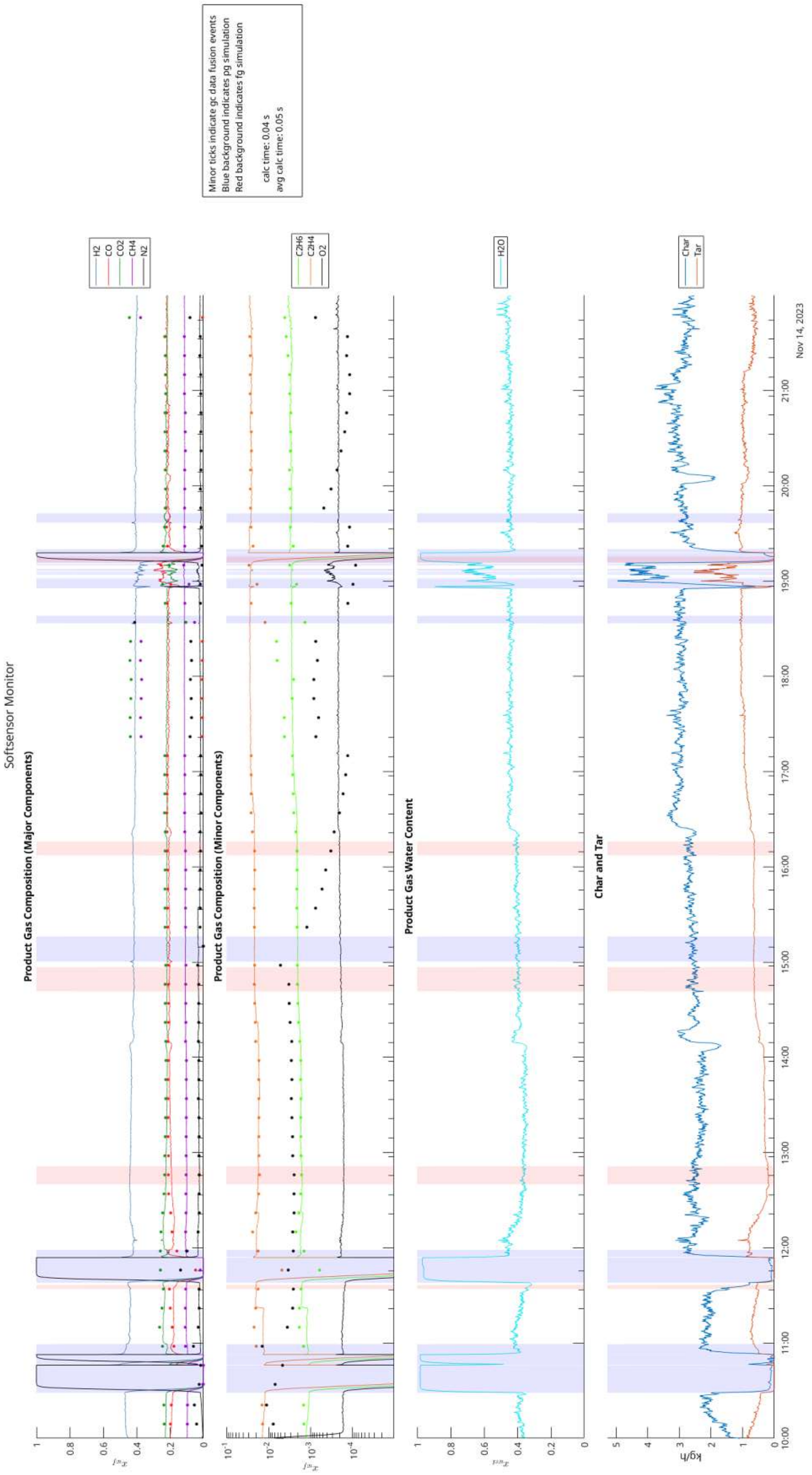

Figure A.1: Soft sensor online monitor.

B Analytical Step Response

In order to recover the time constant τ from the step response, an expression for

$$\frac{\tau}{t'' - t'} \tag{B.1}$$

is required. Knowing this relationship, the time constant τ may be recovered by analyzing the step response curve. For reference, the step response for an interruption in the fuel feed rate is depicted in Figure B.1.

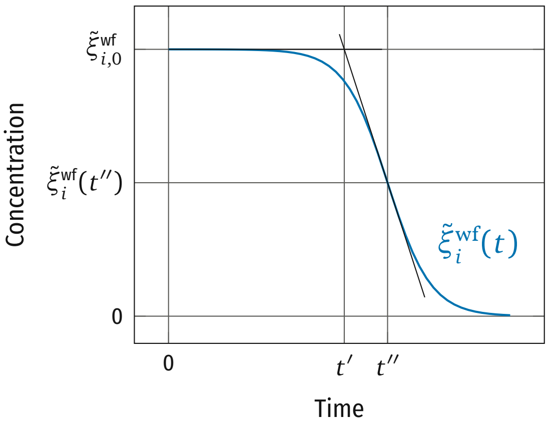

Figure B.1: Analytical response of the dry product gas mole fractions to a step change in the fuel feed rate $\dot{m}_{\mathrm{fuel}}(t = 0) = 0\,\mathrm{kg/h}$.

The rates of change of the molar flows $\dot{n}_i$ and of the total dry product gas molar flow according to the dynamic model eqn. (4.19) are given by

$$\ddot{n}_i = -\frac{1}{\tau_i}\,(\dot{n}_i - f_i)\,, \tag{B.2a}$$

$$\ddot{n}_{\mathrm{PG}}^{\mathrm{wf}} = -\frac{1}{\tau}\sum_j \left(\dot{n}_j - f_j\right) = -\frac{1}{\tau}\left(\dot{n}_{\mathrm{PG}}^{\mathrm{wf}} - f_{\mathrm{PG}}^{\mathrm{wf}}\right), \tag{B.2b}$$

$$\text{where} \quad i, j \in \mathscr{I} = \{H_2, CO, CO_2, CH_4, C_2H_6, C_2H_4, N_2, O_2\}\,.$$

$\dot{n}_{\mathrm{PG}}^{\mathrm{wf}}$ in eqn. (B.2b) denotes the total water-free product gas molar flow rate, and $\tau_i = \tau$ is implied.

When the fuel feed rate is interrupted at time $t_0 = 0\,\mathrm{s}$ ($\dot{m}_{\mathrm{fuel}}(t_0) = 0\,\mathrm{kg/h}$), the soft sensor enters simulation mode and a model switch occurs. As discussed in Section 4.2.3, the molar flow rates of all product gas components, except N_2 and H_2O, are set to 0 kg/h. Therefore the static model predictions equal $f_i = 0\,\mathrm{kg/h}\,\forall i \in \mathscr{I} = \{H_2, CO, CO_2, CH_4, C_2H_6, C_2H_4, O_2\}$, while $f_{N_2} = d_{N_2} = \text{const.}$, and $f_{H_2O} = \dot{m}_{\mathrm{st}} + \dot{m}_{\mathrm{st}}^{\mathrm{LS}}/M_{H_2O}$. Therefore

$$f_{\mathrm{PG}}^{\mathrm{wf}} = \sum_j f_j = f_{N_2} = \text{const.}$$

holds, where $f_{\mathrm{PG}}^{\mathrm{wf}}$ is the predicted water-free product gas molar flow rate.

The rate of change for any of the dry product gas species reads

$$\dot{\xi}_i^{\mathrm{wf}} = \frac{\mathrm{d}}{\mathrm{d}t}\left(\frac{\dot{n}_i}{\dot{n}_{\mathrm{PG}}^{\mathrm{wf}}}\right) = \ldots = -\frac{1}{\tau}\frac{f_{\mathrm{PG}}^{\mathrm{wf}}}{\dot{n}_{\mathrm{PG}}^{\mathrm{wf}}}\xi_i^{\mathrm{wf}}. \tag{B.3}$$

Integrating eqn. (B.3) from 0 to t leads to

$$\ln\frac{\xi_i^{\mathrm{wf}}(t)}{\xi_i^{\mathrm{wf}}(0)} = \ln\frac{\xi_i^{\mathrm{wf}}(t)}{\xi_{i,0}^{\mathrm{wf}}} = -\frac{f_{\mathrm{PG}}^{\mathrm{wf}}}{\tau}\int_0^t \frac{1}{\dot{n}_{\mathrm{PG}}^{\mathrm{wf}}(\zeta)}\mathrm{d}\zeta, \tag{B.4}$$

where ζ serves as integration variable. In order to solve the integral on the right hand side, the function $\dot{n}_{\mathrm{PG}}^{\mathrm{wf}}(t)$ needs to be found from eqn. (B.2b), which can be rewritten as follows:

$$\dot{n}_{\mathrm{PG}}^{\mathrm{wf}} + \frac{1}{\tau}\dot{n}_{\mathrm{PG}}^{\mathrm{wf}} - \frac{1}{\tau}f_{\mathrm{PG}}^{\mathrm{wf}} = 0. \tag{B.5}$$

The homogeneous solution to eqn. (B.5) is

$$\dot{n}_{\mathrm{PG}}^{\mathrm{wf}}(t) = C_1 e^{-t/\tau}. \tag{B.6}$$

The particular solution may be found by variation of constants, letting $C_1 \to C_1(t)$. Inserting this ansatz into eqn. (B.5) leads to

$$\dot{C}_1(t)e^{-t/\tau} - \frac{C_1}{\tau}e^{-t/\tau} + \frac{C_1}{\tau}e^{-t/\tau} - \frac{f_{\mathrm{PG}}^{\mathrm{wf}}}{\tau} = 0.$$

Therefore,

$$\dot{C}_1(t) = \frac{f_{\mathrm{PG}}^{\mathrm{wf}}}{\tau}e^{t/\tau}$$

must hold. Integration gives

$$C_1(t) = f_{\mathrm{PG}}^{\mathrm{wf}}e^{t/\tau} + C_2.$$

Consequently, the temporal evolution of $\dot{n}_{\mathrm{PG}}^{\mathrm{wf}}$ is given by

$$\dot{n}_{\mathrm{PG}}^{\mathrm{wf}}(t) = \left(f_{\mathrm{PG}}^{\mathrm{wf}}e^{t/\tau} + C_2\right)e^{-t/\tau}$$

With the initial condition $\dot{n}_{\mathrm{PG}}^{\mathrm{wf}}(0) = \dot{n}_{\mathrm{PG},0}^{\mathrm{wf}}$ it follows that

$$C_2 = \dot{n}_{\mathrm{PG},0}^{\mathrm{wf}} - f_{\mathrm{PG}}^{\mathrm{wf}}.$$

This leads to the final expression for the temporal development of the molar flow rate of the water-free product gas after the step input:

$$\dot{n}_{\mathrm{PG}}^{\mathrm{wf}}(t) = \dot{n}_{\mathrm{PG},0}^{\mathrm{wf}} e^{-t/\tau} + f_{\mathrm{PG}}^{\mathrm{wf}}\left(1 - e^{-t/\tau}\right). \tag{B.7}$$

Using this result, the integral in eqn. (B.4) can be evaluated:

$$\begin{aligned} \int_0^t \frac{1}{\dot{n}_{\mathrm{PG}}^{\mathrm{wf}}(\zeta)} \mathrm{d}\zeta &= \int_0^t \frac{1}{\dot{n}_{\mathrm{PG},0}^{\mathrm{wf}} e^{-\zeta/\tau} + f_{\mathrm{PG}}^{\mathrm{wf}}\left(1 - e^{-\zeta/\tau}\right)} \mathrm{d}\zeta = \dots \\ &= \frac{\tau}{f_{\mathrm{PG}}^{\mathrm{wf}}} \ln\left(1 - \frac{f_{\mathrm{PG}}^{\mathrm{wf}}}{\dot{n}_{\mathrm{PG},0}^{\mathrm{wf}}}\left(1 - e^{t/\tau}\right)\right). \end{aligned} \tag{B.8}$$

Eqn. (B.4) then becomes

$$\ln \frac{\xi_i^{\mathrm{wf}}(t)}{\xi_{i,0}^{\mathrm{wf}}} = -\ln\left(1 - \frac{f_{\mathrm{PG}}^{\mathrm{wf}}}{\dot{n}_{\mathrm{PG},0}^{\mathrm{wf}}}\left(1 - e^{t/\tau}\right)\right),$$

which may be rewritten, to yield the wanted expression

$$\xi_i^{\mathrm{wf}}(t) = \frac{\xi_{i,0}^{\mathrm{wf}}}{1 - \frac{f_{\mathrm{PG}}^{\mathrm{wf}}}{\dot{n}_{\mathrm{PG},0}^{\mathrm{wf}}}\left(1 - e^{t/\tau}\right)}. \tag{B.9}$$

To obtain the characteristic times t' and t'', both the first and second derivatives of eqn. (B.9) are required. They are given by

$$\dot{\xi}_i^{\mathrm{wf}}(t) = -\frac{f_{\mathrm{PG}}^{\mathrm{wf}} \dot{n}_{\mathrm{PG},0}^{\mathrm{wf}} \xi_{i,0}^{\mathrm{wf}} e^{t/\tau}}{\tau\left(\dot{n}_{\mathrm{PG},0}^{\mathrm{wf}} - f_{\mathrm{PG}}^{\mathrm{wf}}\left(1 - e^{t/\tau}\right)\right)^2}, \tag{B.10a}$$

$$\ddot{\xi}_i^{\mathrm{wf}}(t) = \frac{f_{\mathrm{PG}}^{\mathrm{wf}} \dot{n}_{\mathrm{PG},0}^{\mathrm{wf}} \xi_{i,0}^{\mathrm{wf}} e^{t/\tau}\left(f_{\mathrm{PG}}^{\mathrm{wf}}\left(1 + e^{t/\tau}\right) - \dot{n}_{\mathrm{PG},0}^{\mathrm{wf}}\right)}{\tau^2\left(\dot{n}_{\mathrm{PG},0}^{\mathrm{wf}} - f_{\mathrm{PG}}^{\mathrm{wf}}\left(1 - e^{t/\tau}\right)\right)^3}. \tag{B.10b}$$

The position t'' of the steepest slope of $\xi_i^{\mathrm{wf}}(t)$ coincides with the root of the second derivative eqn. (B.10b), i.e., $\ddot{\xi}_i^{\mathrm{wf}}(t'' = 0)$. It is found to be

$$t'' = \tau \ln\left(\frac{\dot{n}_{\mathrm{PG},0}^{\mathrm{wf}}}{f_{\mathrm{PG}}^{\mathrm{wf}}} - 1\right) \tag{B.11}$$

Inserting this value into eqn. (B.9) yields the associated dry product gas composition:

$$\xi_i^{\mathrm{wf}}(t'') = \frac{\xi_{i,0}^{\mathrm{wf}}}{1 - \frac{f_{\mathrm{PG}}^{\mathrm{wf}}}{\dot{n}_{\mathrm{PG},0}^{\mathrm{wf}}}\left(1 - e^{t''/\tau}\right)} = \frac{\xi_{i,0}^{\mathrm{wf}}}{2}. \tag{B.12}$$

The intersection of the tangent at the point $\left(t'', \xi_i^{\mathrm{wf}}(t'')\right)$ with the horizontal line at $\xi_{i,0}^{\mathrm{wf}}$ is located at

$$t' = t'' - \frac{1}{\dot{\xi}_i^{\mathrm{wf}}(t'')}\left(\xi_i^{\mathrm{wf}}(t'') - \xi_{i,0}^{\mathrm{wf}}\right) \tag{B.13}$$

Inserting the result from eqn. (B.11) yields

$$t' = t'' + \frac{\tau\left(\dot{n}^{\mathrm{wf}}_{\mathrm{PG},0} - f^{\mathrm{wf}}_{\mathrm{PG}}\left(1 - e^{t''/\tau}\right)\right)^2}{f^{\mathrm{wf}}_{\mathrm{PG}}\dot{n}^{\mathrm{wf}}_{\mathrm{PG},0}\tilde{\xi}^{\mathrm{wf}}_{i,0}e^{t''/\tau}}\left(\tilde{\xi}^{\mathrm{wf}}_{i}(t'') - \tilde{\xi}^{\mathrm{wf}}_{i,0}\right),$$

which may be rewritten, to yield the sought-for expression

$$\frac{\tau}{t'' - t'} = \frac{1}{\tilde{\xi}^{\mathrm{wf}}_{i}(t'') - \tilde{\xi}^{\mathrm{wf}}_{i,0}}\left(-\frac{\tilde{\xi}^{\mathrm{wf}}_{i,0}\left(1 - \frac{f^{\mathrm{wf}}_{\mathrm{PG}}}{\dot{n}^{\mathrm{wf}}_{\mathrm{PG},0}}\right)}{4}\right). \tag{B.14}$$

Apparently, this result depends only on the ratio $f^{\mathrm{wf}}_{\mathrm{PG}}/\dot{n}^{\mathrm{wf}}_{\mathrm{PG},0}$. Since $f^{\mathrm{wf}}_{\mathrm{PG}} \ll \dot{n}^{\mathrm{wf}}_{\mathrm{PG},0}$, this expression can be simplified further

$$\frac{\tau}{t'' - t'} \approx -\frac{\tilde{\xi}^{\mathrm{wf}}_{i,0}}{4\left(\tilde{\xi}^{\mathrm{wf}}_{i}(t'') - \tilde{\xi}^{\mathrm{wf}}_{i,0}\right)} = \frac{1}{2} \tag{B.15}$$

Considering eqn. (B.11), the time constant τ can therefore be recovered from the step response, using

$$\tau \approx \frac{t'' - t'}{2}. \tag{B.16}$$

C Parameters

Table C.1 lists elemental compositions of various compounds needed by the soft sensor.

Table C.1: Elemental composition of various compounds used throughout the calculations in this work.

			ξ^{waf}			ξ^{wf}	ξ^{wet}	ρ
Compound	C	H	O	N	S	Ash	H_2O	$\mathrm{kg/m^3}$
Softwood	0.507	0.059	0.043	0.002	0	0.002	0.072	
Char	0.85	0.04	0.12	0	0	0	0	
Tar	0.94	0.06	0	0	0	0	0	
Oil	0.87	0.13	0	0	0	0	0	820

In the following, the initialization values for the soft sensor, the time constants and thresholds, as well as the values for the covariance matrices of the $\mathrm{EKF_x}$ and $\mathrm{EKF_d}$ are given.

The initial value of the system state, $\boldsymbol{x}_{\mathrm{init}}$, equals to the average value of the system state in the identification data:

$$\begin{aligned}\boldsymbol{x}_{\mathrm{init}} = \big[&0.426 \quad 0.190 \quad 0.238 \quad 0.0953 \quad 0.001\,22 \quad 0.0133 \quad 1.00\cdot 10^{-4} \quad \dots \\ &0.0557 \quad 0.534 \quad 0.113 \quad 0.0784 \quad 0.123 \quad 0.334 \quad 2.32 \quad \dots \\ &0.329 \quad 952 \quad 5.00\big]^{\top}.\end{aligned}$$

Conversely, the initial values of the disturbances are chosen such that they have no effect on the initial prediction:

$$\boldsymbol{d}_{\mathrm{init}} = \begin{bmatrix}1 & 1 & 1 & 1 & 1 & 1 & 0 & 1\end{bmatrix}^{\top}.$$

The covariance matrices $\boldsymbol{P}_{\mathrm{x,init}}$ and $\boldsymbol{P}_{\mathrm{d,init}}$ are initialized arbitrarily by

$$\boldsymbol{P}_{\mathrm{x,init}} = \mathbf{I}, \quad \boldsymbol{P}_{\mathrm{d,init}} = \mathbf{I},$$

whereas the state transition matrices and the control input matrices, respectively, are constant and follow from the time discretization as described in sections 5.2 and 5.3:

$$\boldsymbol{\Phi}_{\mathrm{x}} = 0.8462\cdot\mathbf{I}, \quad \boldsymbol{\Phi}_{\mathrm{d}} = \mathbf{I}, \quad \boldsymbol{\Gamma}_{\mathrm{x}} = 0.1538\cdot\mathbf{I}, \quad \boldsymbol{\Gamma}_{\mathrm{d}} = \mathbf{0}.$$

The process noise and measurement noise covariances have been assumed to be diagonal matrices:

$$\begin{aligned} \boldsymbol{Q}_{\mathrm{x}} &= 0.1 \cdot \operatorname{diag}\left(\boldsymbol{x}_{\mathrm{init}}^{\top}\right), \\ \boldsymbol{Q}_{\mathrm{d}} &= \begin{bmatrix} 10^{-4} & 10^{-4} & 10^{-4} & 10^{2} & 10^{1} & 10^{-1} & 10^{-3} & 10^{-3} \end{bmatrix}^{\top}, \\ \boldsymbol{R}_{\mathrm{PG}}^{\mathrm{ana}} &= \begin{bmatrix} 10^{1} & 1 & 1 & 1 & 10^{3} & 10^{3} \end{bmatrix}, \quad \boldsymbol{R}_{\mathrm{FG}}^{\mathrm{ana}} = \operatorname{diag}\left(\begin{bmatrix} 1 & 1 & 1 \end{bmatrix}\right), \\ \boldsymbol{R}_{\mathrm{PG,GC}} &= \operatorname{diag}\left(\begin{bmatrix} 10^{-2} & 10^{-2} & 10^{-2} & 10^{-2} & 10^{-2} & 10^{-2} & 10^{-2} \end{bmatrix}\right). \end{aligned}$$

The particular values have been determined iteratively by comparing the soft sensor's output to the historical data.

The sampling times are given, whereas the time constant was arbitrarily defined as a multiple of the sampling time (see sections 4.3, 5.1 and 6.5):

$$T_s = 5\,\mathrm{s}, \quad T_s^{\mathrm{GC}} = 12\,\mathrm{min}, \quad \tau_i = 30\,\mathrm{s}.$$

Finally, the threshold parameters used for the fault detection mechanism were determined as described in Section 5.5:

$$\boldsymbol{\theta} = \begin{bmatrix} \theta_{\mathrm{PG}}^{\mathrm{ana}} & \theta_{\mathrm{FG}}^{\mathrm{ana}} & \theta_{\mathrm{PG}}^{\mathrm{GC}} \end{bmatrix}^{\top} = \begin{bmatrix} 10^{-2} & 10^{-2} & 5 \cdot 10^{-2} \end{bmatrix}^{\top}.$$

D Historical Data

This chapter documents the historical data, which was utilized in the identification process (see Section 3.1) in the form of time series diagrams. In each diagram, periods of steady state operation are indicated.

It is worth pointing out that the test run on May 16, 2023, was aborted because errors in the calibration of both the fuel feed rate and oil feed rate measurements were detected. While an attempt was made to rectify this in hindsight, the char production rate recovered by means of closing the material balance is at or near 0 kg/h at some points, which does not appear plausible. This issue may also have been present during the test on November 23, 2022.

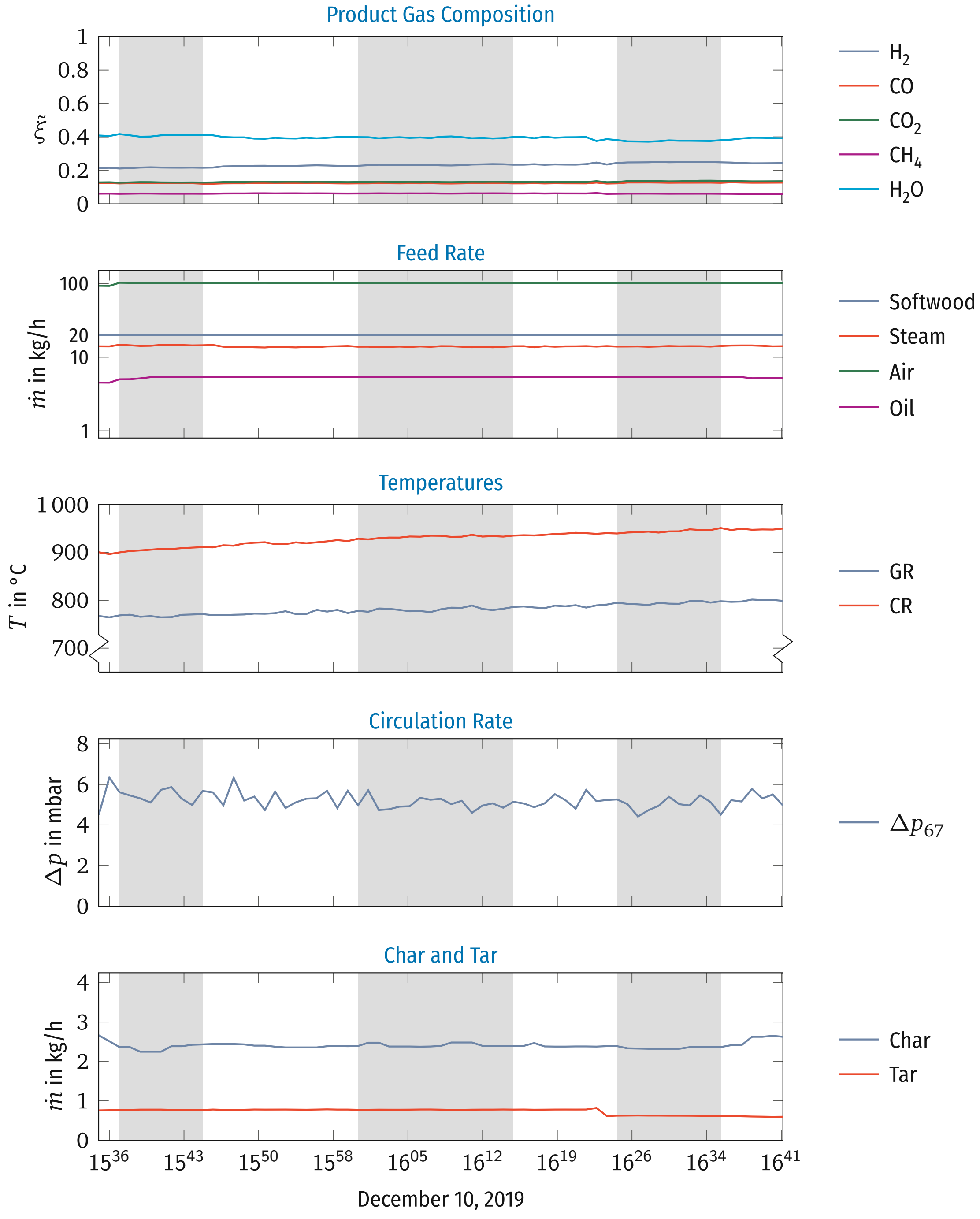

Figure D.1: Test run on December 10, 2019. *Steady state* sample intervals are highlighted by ▨.

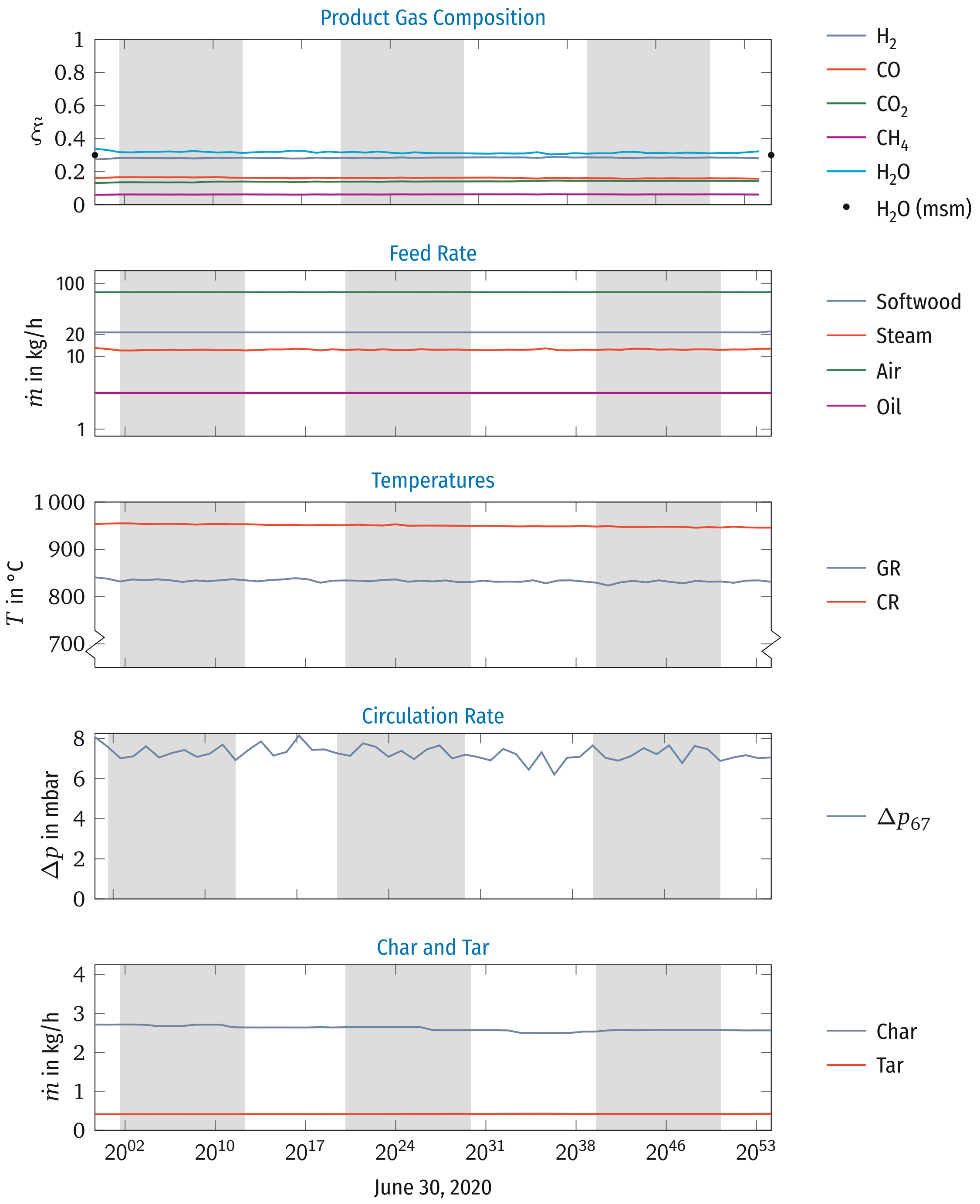

Figure D.2: Test run on June 30, 2020. *Steady state* sample intervals are highlighted by ░.

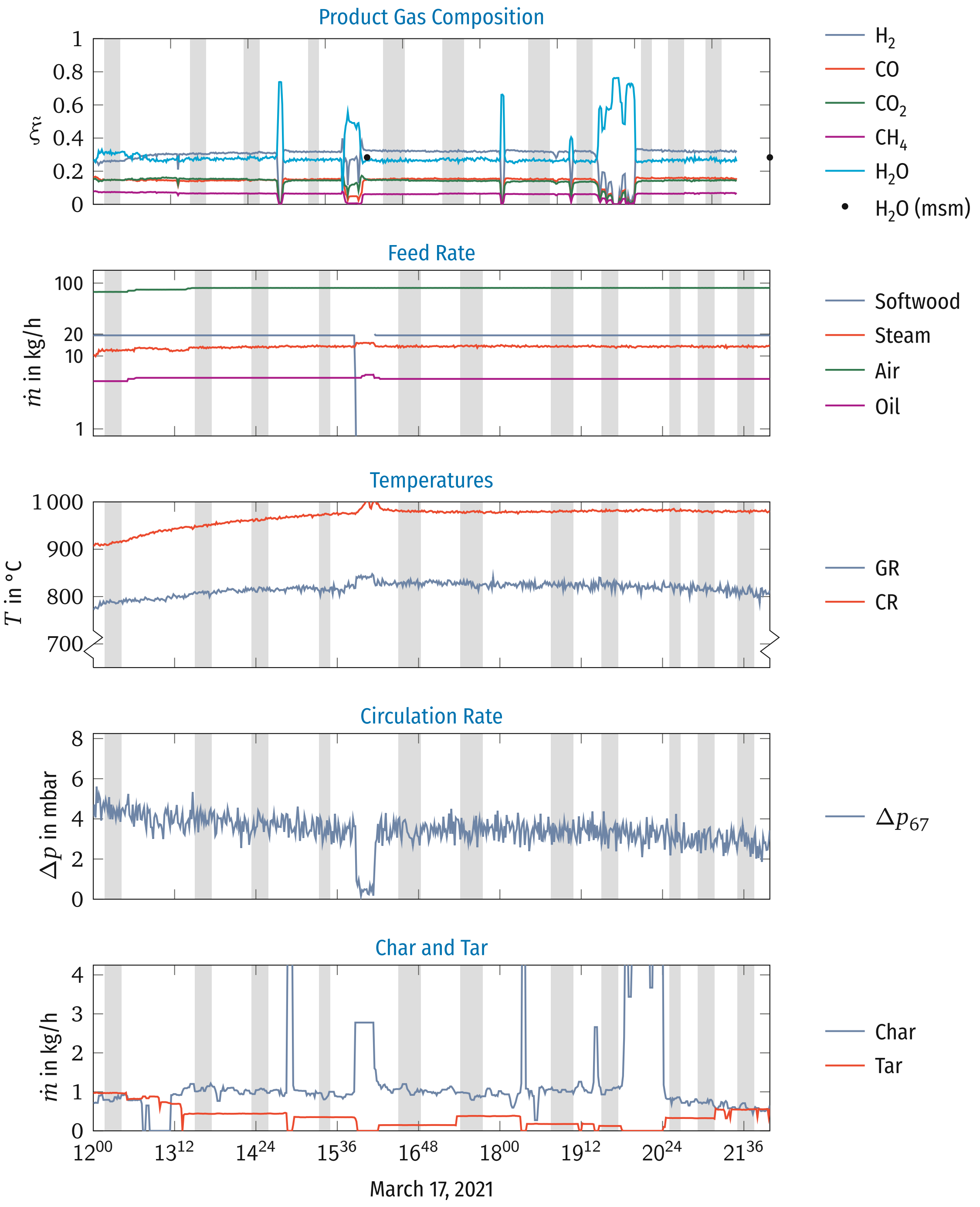

Figure D.3: Test run on March 17, 2021. *Steady state* sample intervals are highlighted by ▨.

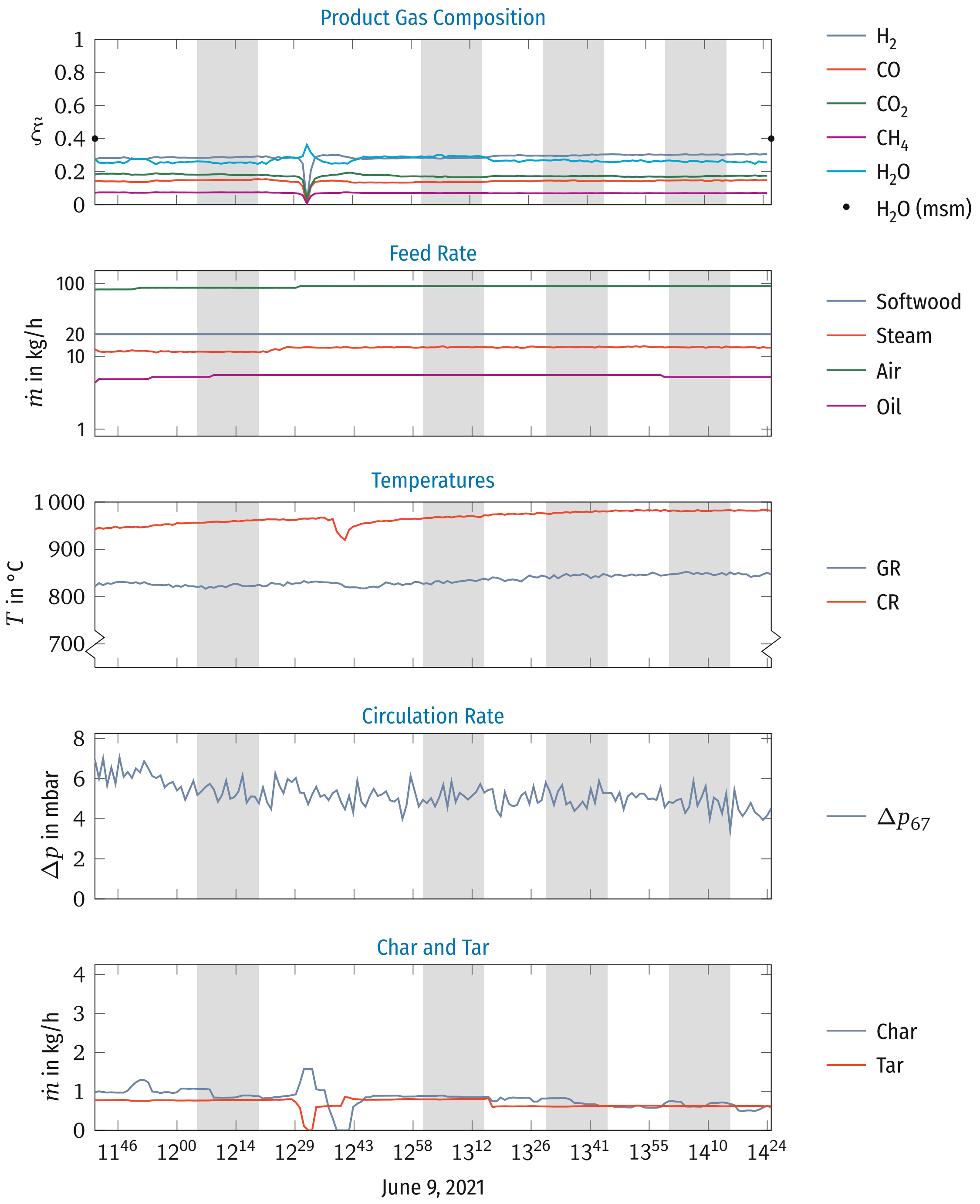

Figure D.4: Test run on June 9, 2021. *Steady state* sample intervals are highlighted by ▨ .

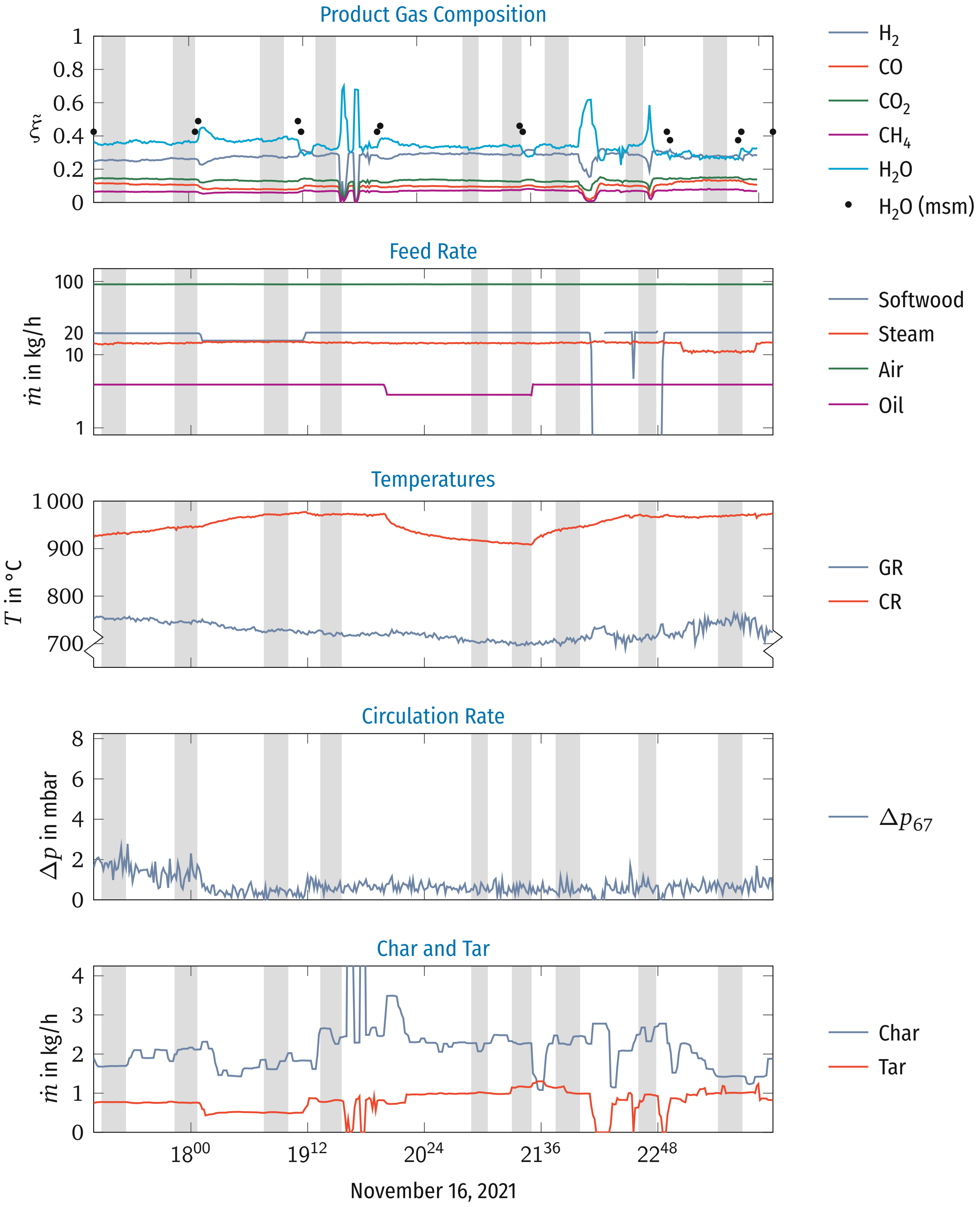

Figure D.5: Test run on November 16, 2021. *Steady state* sample intervals are highlighted by ▨.

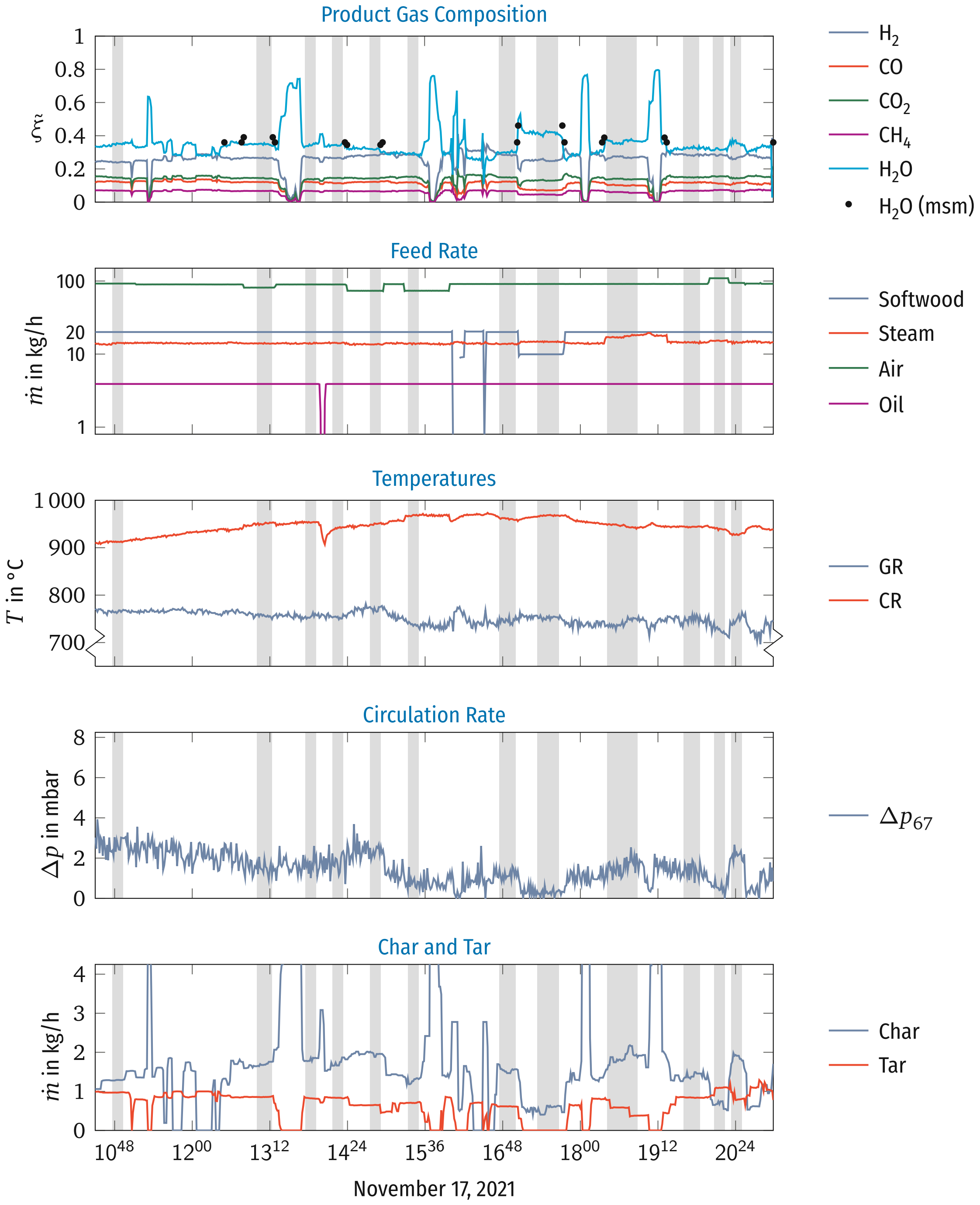

Figure D.6: Test run on November 17, 2021. *Steady state* sample intervals are highlighted by ▨ .

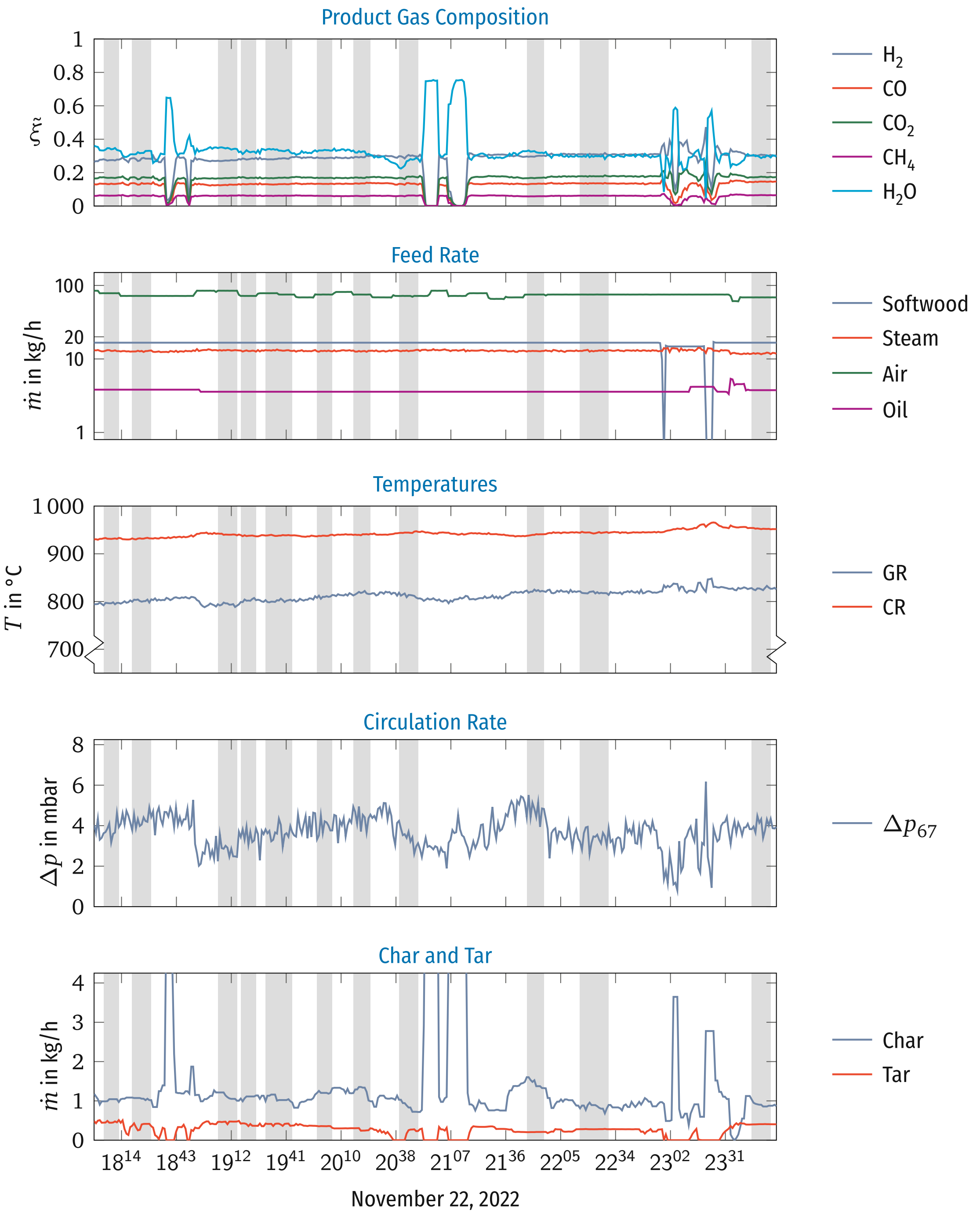

Figure D.7: Test run on November 22, 2022. *Steady state* sample intervals are highlighted by ▨.

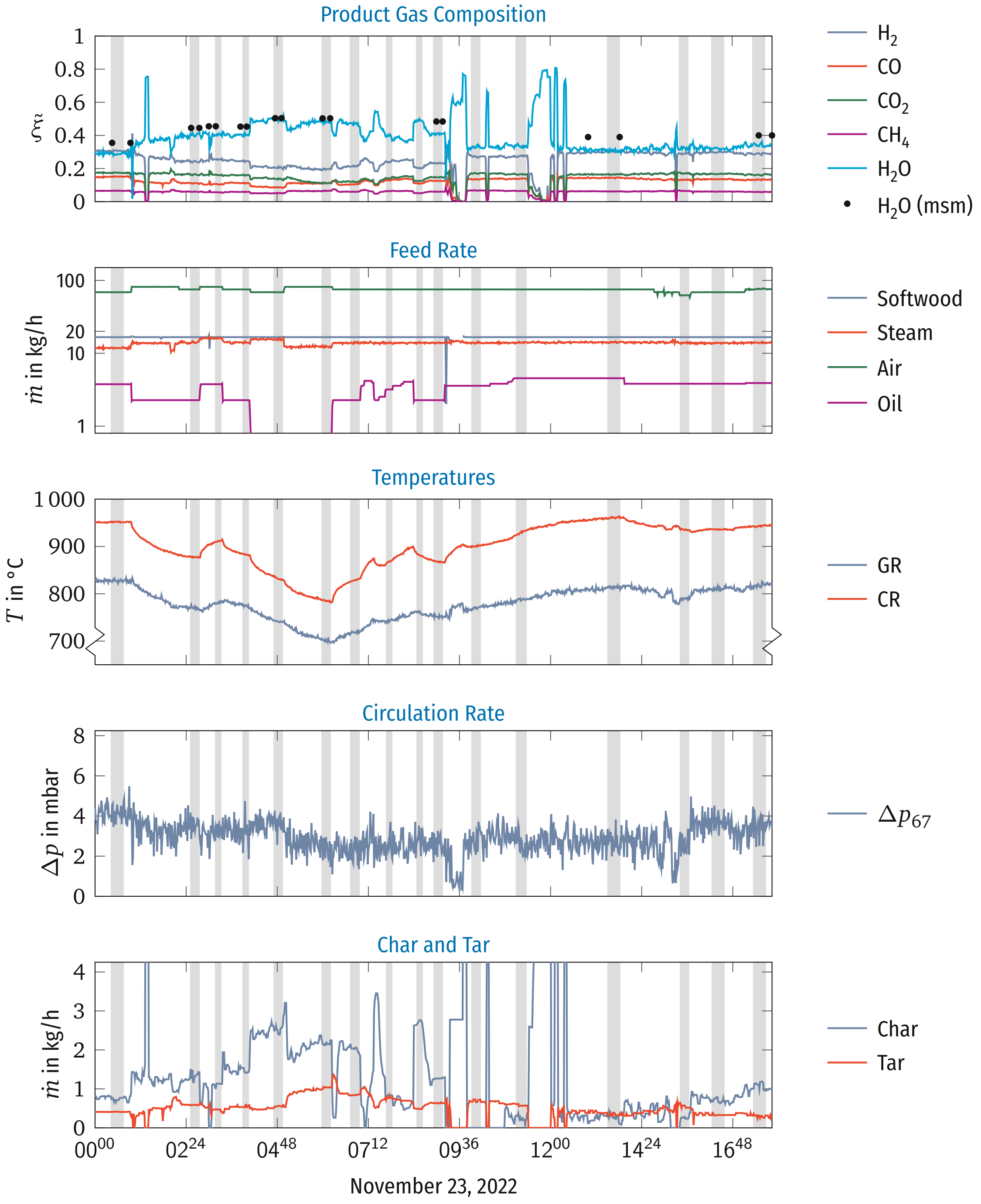

Figure D.8: Test run on November 23, 2022. *Steady state* sample intervals are highlighted by ■.

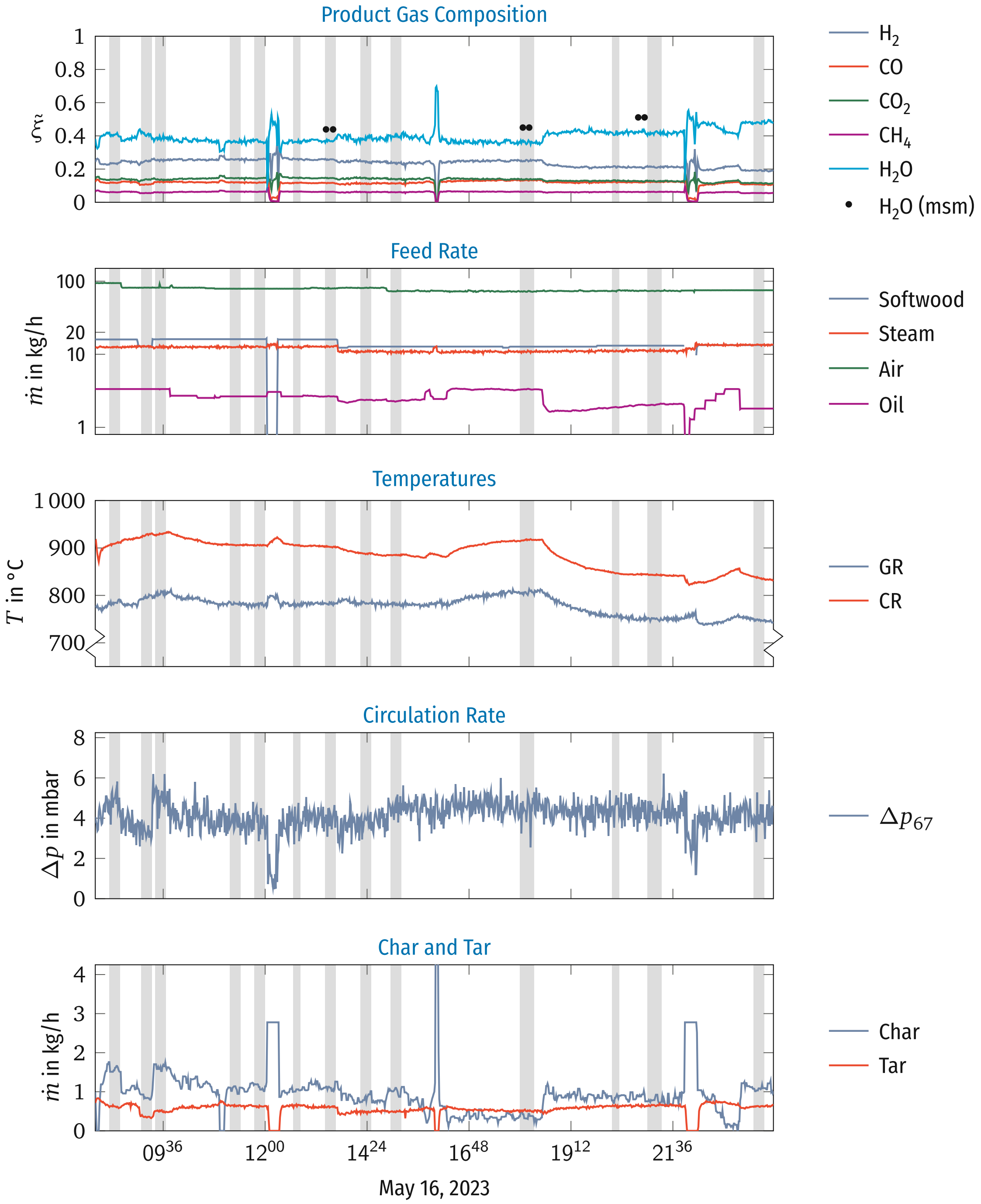

Figure D.9: Test run on May 16, 2023. *Steady state* sample intervals are highlighted by ▨.

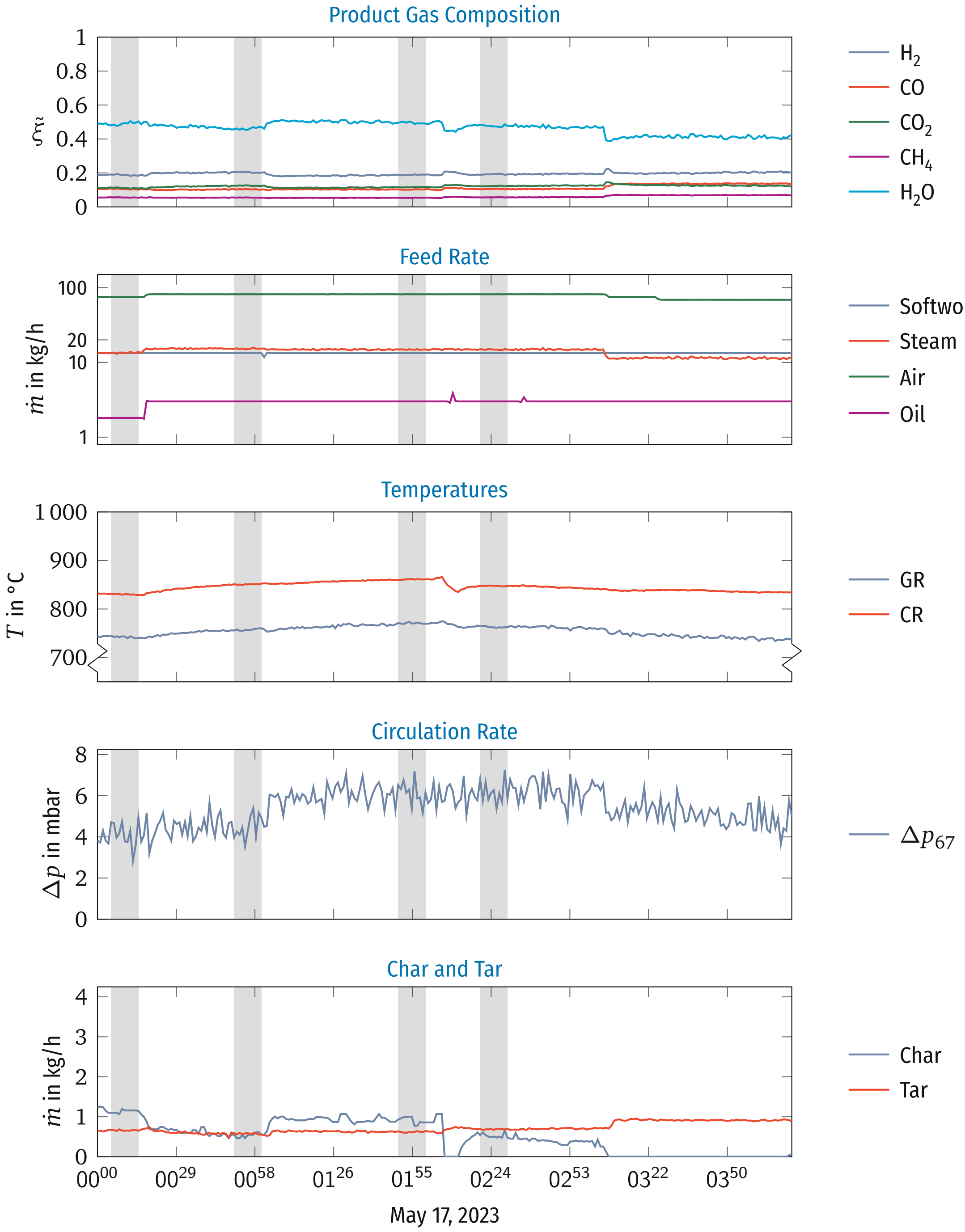

Figure D.10: Test run on May 17, 2023. *Steady state* sample intervals are highlighted by ▨.